

# Active plasmonic sources based on graphene and molybdenum disulfide

Charith Kohomban Wickrama Jayasekara  
B.Sc Engineering(Hons)

Submitted in total fulfilment of the requirements for the degree of  
Doctor of Philosophy



Main Supervisor  
Professor Malin Premaratne

Associate Supervisor  
Professor Govind P. Agrawal  
University of Rochester, USA

**Department of Electrical and Computer Systems Engineering**  
MONASH UNIVERSITY  
CLAYTON, VIC 3800, AUSTRALIA

June 2017

Copyright © Charith Kohomban Wickrama Jayasekara (2017)

All rights reserved. No part of the publication may be reproduced in any form by print, photoprint, microfilm or any other means without written permission from the author.

# Summary

**S**URFACE Plasmon Amplification by Stimulated Emission of Radiation (Spaser) is the future of nano-electronics and nano-optics based applications such as nanoscopy, nano-lithography, and nano-optoelectronics powered information processing. Spaser, being the nanoplasmonic counterpart of laser, shares many common structural components of a laser resonator. Essentially, very much similar to a laser, a spaser is made by coupling a nanoparticle (acting as a resonator cavity) to a gain (active) medium, where photons are replaced by surface plasmons (SP). A spaser compensates the optical losses in the metal by the gain in the active medium, where the resonating eigenmodes of the plasmonic nanosystem provides localize, intense, and coherent electric fields. Nanoparticles comprising noble metals, like gold and silver, are usually used as resonators. However, owing to diverse tunable physical properties of graphene, the use of 2D materials such as graphene and molybdenum disulfide as the resonator could be of great practical interest. These 2D materials based plasmonic nanolasers have shown immense potential in numerous applications, owing to their exotic features of ultra-speed operation, electric field enhancement, miniaturized design and strong near-field confinement. In order to practically realize these exciting features, further analysis of both steady state and dynamic responses are much required for graphene and molybdenum disulfide based spasers. Particularly, in terms of plasmonic quality factor of the resonator, threshold gain requirements, plasmonic modes and mode energies, energy level shifts and pulsed operation characteristics. This research aimed at investigating these issues based on analytical and numerical techniques in order to analyse the behaviour of realistic graphene and molybdenum disulfide based spasers, and developing a set of simple design guidelines for futuristic plasmonic devices and applications.



# General Declaration

In accordance with Monash University Doctorate Regulation 17 / Doctor of Philosophy and Master of Philosophy (MPhil) regulations the following declarations are made:

I hereby declare that this thesis contains no material which has been accepted for the award of any other degree or diploma at any university or equivalent institution and that, to the best of my knowledge and belief, this thesis contains no material previously published or written by another person, except where due reference is made in the text of the thesis. The core theme of the thesis is modelling and analysing of the output and operational characteristics of active plasmonic devices based on graphene and molybdenum disulfide. The ideas, development and writing up of all the papers in the thesis were the principal responsibility of myself, the candidate, working within the Department of Electrical and Computer Systems Engineering under the main supervision of Professor Malin Premaratne.



---

Charith Kohomban Wickrama Jayasekara

June 2017



# Acknowledgements

Firstly, I would like to express my sincere gratitude to my supervisor Prof. Malin Premaratne for the continuous support during my Ph.D study and related research, for his motivation, immense knowledge, and his patience . His guidance helped me in all the time of research and writing of this thesis. I could not have imagined having a better advisor and mentor for my Ph.D study. I would also like to thank Dr. Weiren Zhu and Dr. Chintha Handapangoda for their technical assistance and brainstorming sessions. Moreover, I extend my gratitude to all my colleagues at Advanced Computing and Simulations Laboratory (A $\chi$ L), Thamani, Chanaka, Deb, Chathurangi, Tamara, Dilusha, Ashan, Lakshitha, Sudaraka, Tharindu, Harini, Viraj, Champi and Nethanjalie for sharing their time, views and ideas and even food, making this life of research more enjoyable and memorable. I greatly appreciate everyone's efforts, contributions and motivational support that made my Ph.D experience more productive and effective.

Besides them, I would like to thank Monash Graduate Education (MGE) and the Department of Electrical and Computer Systems Engineering for providing me prestigious scholarships to cover my tuition fees and living expenses. Additionally, for providing financial assistance during the overseas conference travel and extending my candidature. Moreover, I sincerely acknowledge all the staff and my fellow colleagues of the Department of Electrical and Computer Systems Engineering for their support and for making this three and half years pleasant and enriching.

Apart from the world of research, I am so lucky to have a lovely, supportive and cheerful group of friends. In their company, I explored most of the beautiful places of this lovely country and spent quality time. Especially, Buddhika ayya, Ayal, Nimal

uncle, Ashani, Arunodhi akka, Mahela ayya, Chamila Ayya, Pabasara, Chamal, Ama, Awanthi, Cathy and Andrew deserve a special mention for making my Ph.D. life more exciting and memorable.

Last, but not least, my beloved parents and sister, my father Wijepala Jayasekara, my mother Nirmala Gunasekara and my sister Anuradhi who have provided me moral and emotional support in my life. Without their unconditional love, support and sacrifices, this PhD would not have been possible. They devoted their life bringing me up and managed all the hard work by themselves to support me and achieve my dream of achieving a doctorate. Furthermore, I greatly appreciate our Dr. Amma's (Dr. Nirmalie Jayasinghe) support for keeping my family safe and healthy. Moreover, my father in law Late Gamini Thilakarathna, mother in law Vinitha Jayarathna, my brother Amila and my sister Shanadi receive a special mention for their support and sacrifices. Additionally, Athil ayya and family for being such a support to me and my family since I landed in Melbourne. My beautiful wife, Sajeewa, receives a special mention for being a wonderful life partner with her endless love, care, support and encouragement. I appreciate my baby, my little girl Siheli for abiding my ignorance and the patience she showed during my thesis writing. I consider myself the luckiest person in the world to have a caring and lovely family, standing beside me with their unconditional support and love. Thanks for all your encouragements !

**Charith Jayasekara.**

*To my most beloved parents, my daughter Siheli and my life partner, my beautiful wife  
Sajeewa: because I owe it all to you. Many Thanks!*



# Contents

<b>1</b>	<b>Introduction</b>	<b>1</b>
1.1	Aims of the research . . . . .	5
1.2	Thesis Outline . . . . .	8
<b>2</b>	<b>Theory of spasers</b>	<b>11</b>
2.1	Design and components . . . . .	11
2.2	Operation principles of a spaser . . . . .	13
2.3	Background theory . . . . .	14
2.4	Insight in to the history of spasers . . . . .	15
2.4.1	Theoretical work on spasers . . . . .	15
2.4.2	Experimental realisations of spasers . . . . .	17
2.4.3	Spasers made of graphene . . . . .	20
<b>3</b>	<b>Quantum mechanical model of a spaser</b>	<b>23</b>
3.1	The Hamiltonian of a spaser . . . . .	23
3.2	Motion equations . . . . .	24
3.3	Continuous wave (CW) operation . . . . .	25
<b>4</b>	<b>Two-dimensional resonator-based spasers</b>	<b>27</b>
4.1	Two-dimensional plasmonic materials . . . . .	27
4.1.1	Graphene . . . . .	28
4.1.1.1	Mono-layer graphene (MLG) . . . . .	29
4.1.1.2	Bi-Layer Graphene (BLG) . . . . .	32
4.1.2	Molybdenum disulfide . . . . .	34
4.1.3	Other potential materials . . . . .	35
4.2	Equations of a circular spaser . . . . .	35
4.2.1	Comparison of square and circular graphene flakes . . . . .	38
<b>5</b>	<b>Graphene based spasers</b>	<b>43</b>
5.1	Circular graphene spaser . . . . .	43
5.1.1	Spaser Model . . . . .	44
5.1.1.1	Design . . . . .	44
5.1.1.2	Spaser modes and degeneracy . . . . .	45
5.1.1.3	Quantum cascade well . . . . .	47
5.1.2	Results and Discussion . . . . .	49
5.1.2.1	Analytical model . . . . .	49
5.1.2.2	Operational characteristics and their tunability . . . . .	49

5.1.3	Conclusion . . . . .	54
5.2	Ultra-fast dynamics of graphene spasers . . . . .	55
5.3	Spaser made of un-doped graphene . . . . .	66
5.3.1	Results and discussion . . . . .	66
5.3.2	Conclusion . . . . .	70
5.4	Summary . . . . .	71
<b>6</b>	<b>An MoS<sub>2</sub>-based spaser</b>	<b>73</b>
6.1	Introduction . . . . .	73
6.2	Results and Discussion . . . . .	74
6.2.1	Design of the spaser . . . . .	74
6.2.2	MoS <sub>2</sub> resonator and degeneracy modes . . . . .	76
6.2.3	Active medium and the operation of the spaser . . . . .	78
6.2.4	Analysis of the performance . . . . .	79
6.2.4.1	Condition for continuous spasing . . . . .	82
6.3	Comparison between MoS <sub>2</sub> and graphene resonators . . . . .	84
6.4	Summary . . . . .	87
<b>7</b>	<b>Design guidelines of spasers and applications</b>	<b>89</b>
7.1	Spaser design guidelines . . . . .	89
7.1.1	Designing the components of a spaser . . . . .	89
7.1.1.1	Resonator . . . . .	89
7.1.1.2	Active medium / gain system . . . . .	91
7.1.1.3	Pump . . . . .	91
7.1.2	Operational Characteristics . . . . .	92
7.1.2.1	Q-Factor . . . . .	92
7.1.2.2	Threshold gain . . . . .	93
7.1.2.3	Electric field amplitude . . . . .	94
7.1.2.4	Rate of surface plasmon generation . . . . .	94
7.2	Applications of spasers . . . . .	94
7.2.1	Continuous wave operation (CW mode) . . . . .	95
7.2.1.1	Nano-lithography . . . . .	95
7.2.1.2	Nano-Scopy . . . . .	95
7.2.1.3	Lab-on-a-chip . . . . .	95
7.2.1.4	Quantum computing . . . . .	96
7.2.2	Spaser as an amplifier . . . . .	96
7.2.3	Spaser as a modulator . . . . .	97
7.2.4	Applications in bio-medicine . . . . .	97
<b>8</b>	<b>Conclusions and future work</b>	<b>99</b>
8.1	Summary of contributions . . . . .	99
8.2	Suggestions for future research . . . . .	104
	<b>Abbreviations</b>	<b>106</b>

<b>A Resonator wavelengths</b>	<b>107</b>
A.1 Graphene Resonance Wavelengths . . . . .	107
A.2 Bi-layer Graphene (BLG) Resonance Wavelengths . . . . .	109
A.3 MoS <sub>2</sub> Resonance Wavelengths . . . . .	110
<b>B Numerical Methods</b>	<b>111</b>



# List of Figures

2.1	Main components and operation of the spaser. . . . .	12
2.2	Energy transitions of a spaser. . . . .	13
2.3	Spaser made of V-shaped metallic inclusion surrounded by quantum dots. . . . .	15
2.4	Electrically pumped spasers. . . . .	16
2.5	Electrically pumped bowties spasers . . . . .	18
2.6	Two-dimensional spaser . . . . .	19
2.7	Carbon based spaser . . . . .	21
2.8	Quantum cascade well powered, graphene spaser . . . . .	21
4.1	E-K diagrams of mono-layer graphene . . . . .	30
4.2	Real values of relative complex permittivity of mono-layer graphene. . . . .	31
4.3	Imaginary values of complex permittivity of mono-layer graphene. . . . .	31
4.4	Corresponding E-K diagrams of Bi-layer graphene. . . . .	32
4.5	Real values of the relative complex permittivity of bi-layer graphene. . . . .	33
4.6	Imaginary values of the complex permittivity of bi-layer graphene. . . . .	33
4.7	Comparison between a circular resonator with a square resonator. . . . .	39
5.1	Spaser based on a circular graphene resonator. . . . .	44
5.2	Normalized electric field distribution of the six lowest energy modes supported by the circular graphene flake. . . . .	46
5.3	Operational principles of the quantum cascade well. . . . .	48
5.4	Tunability of the operational characteristics of the circular graphene spaser. . . . .	49
5.5	Minimum Q-factor requirement with respect to Fermi energy level of the flake and spaser mode energy. . . . .	52
5.6	Schematic diagram of optically pumped, quantum dots powered, mono-layer graphene based spaser . . . . .	56
5.7	Electric field output and the spaser mode energies of the proposed spaser design versus radius of the flake. . . . .	56
5.8	Steady state operational characteristics of the proposed spaser design. . . . .	60
5.9	Dynamic responses of the proposed spaser design. . . . .	62
5.10	Variations in the number of SPs pver time after making the gain 0 and at 100fs <b>(a)</b> when mode energy is 206.78 meV and <b>(b)</b> when mode energy is 248.14 meV. . . . .	63
5.11	Variations in the number of SPs generated on log scale <b>(a)</b> When the SP mode energy is 20 THz <b>(b)</b> 50 THz <b>(c)</b> 60 THz and <b>(d)</b> 100 THz respectively. . . . .	64
5.12	The Steady state responses of six lowest energy modes of the bi-layer graphene based spaser. . . . .	68

5.13	Ultra-fast dynamics of a bi-layer graphene spaser under continuous pumping condition. . . . .	69
5.14	Modulated response of a Bi-layer graphene based spaser. . . . .	70
6.1	Schematic diagram of the proposed spaser based on circular shaped MoS <sub>2</sub> resonator. . . . .	75
6.2	Quantum mechanical model of the spaser with $n$ -states considering degeneracy modes of the resonator. . . . .	78
6.3	Spaser mode energy, electric field amplitude and threshold gain requirement of the proposed spaser design based on MoS <sub>2</sub> . . . . .	80
6.4	Steady state characteristics of the proposed spaser design based on MoS <sub>2</sub> nano-resonator. . . . .	82
6.5	Schematic diagram of the spaser design used to compare spasers based on graphene and molybdenum disulfide. . . . .	85
6.6	Performance comparison between spasers based on Graphene and MoS <sub>2</sub> . . . . .	86
B.1	2D resonant structure considered in COMSOL Multiphysics. . . . .	114

# List of Tables

7.1	Table of spaser mode energy tunability with respect to its resonator type . . . . .	90
7.2	Table of emission spectrum tunability with respect to active medium . . . . .	92
A.1	Table of resonance wavelengths of MLG vs radius when $E_f=0.8$ eV. . . . .	107
A.2	Table of resonance wavelengths of MLG vs Fermi level of the flake when $R = 30$ nm. . . . .	108
A.3	Table of resonance wavelengths of BLG vs radius of the flake when $E_f = 0.0$ eV. . . . .	109
A.4	Table of resonance wavelengths of BLG vs radius of the flake when $E_f = 0.2$ eV. . . . .	109
A.5	Table of resonance wavelengths of BLG vs radius of the flake when $E_f = 0.4$ eV. . . . .	110
A.6	Table of resonance wavelengths of MoS <sub>2</sub> flake vs radius when $N_n=8.84 \times 10^{27} \text{ m}^{-3}$ . . . . .	110
A.7	Table of resonance wavelengths of MoS <sub>2</sub> flake vs radius when $N_n=16.85 \times 10^{27} \text{ m}^{-3}$ . . . . .	110



# Publications

## Journal Papers

1. **C. Jayasekara**, M. Premaratne, S.D. Gunapala, and M.I.Stockman, “MoS<sub>2</sub> spaser”, *Journal of Applied Physics*, 119, 133101(2016).
2. **C. Jayasekara**, M. Premaratne, M.I.Stockman, and S.D. Gunapala, “Multimode analysis of highly tunable, quantum cascade powered, circular graphene spaser”, *Journal of Applied Physics*, 118, 173101(2015).

## Journal Papers - Drafted

1. **C. Jayasekara**, M. Premaratne, W. Zhu, H.T. Hattori and M.I.Stockman, “Ultra-fast dynamics of a mono-layer graphene based spaser”.
2. **C. Jayasekara**, M. Premaratne, W. Zhu, and H.T. Hattori , “Un-doped graphene based spaser”.

## Conference Papers

1. **C. Jayasekara**, M. Premaratne, S.D. Gunapala, and M.I.Stockman, “Is MoS<sub>2</sub> better for spasers than graphene?”, *Conference on Lasers and Electro-Optics*, San Jose, USA, (Optical Society of America, 2016), paper FTu1B.2, (2016).



# Chapter 1

## Introduction

**H**IGH speed ultrathin nanodevices play a significant role in designing miniaturized electronic devices [1–3]. These electronic devices consist of active and passive electronic components. Active components are electronic devices with gain or directionality. Unlike passive components, active electronic components have an active region, require a control signal and a minimum voltage or current to perform functions, such as controlling the flow or direction of current. The operating speed of an electronic circuit depends on the delays associated with passive components, and delays occur in active components, such as transistors [4]. However, those limits to reduce the delays have reached their thresholds. Electronic-based systems have reached to their maximum operating speeds, limiting bandwidth and acting as a bottleneck in most of the designs. Therefore, technology such as photonics are essential to maintaining Moore’s law. Photonics is a promising technology for solving this problem and it has been used to design electronic devices that operate at tera-hertz speeds. This technology can also be used to design systems that replace the operation of transistors in optical systems.

The role of the transistor as an active device in electronic systems is replaced by a laser in photonics. Since a laser can work at tera-hertz speeds, it is possible to create ultra-fast opto-electronic devices. However, the use of lasers increases the critical dimensions of the devices, making the setup bulky and inefficient for nano-scale applications. This emphasises the requirement of accomplishing nano-scale active devices based on photonics. Therefore, the ability to manipulate light at the nanoscale level enables many different applications, including, but not limited to, building efficient optical intercon-

nects, sources, amplifiers, modulators and sensors. To this end, significant progress in the field of nanophotonics has been made over the past two decades [2–5].

The wavelength used in most of these technologies is in the order of micrometers. Thus, the fundamental diffraction limit has intervened to constrain the advantages of scaling below the subwavelength dimensions. With sophisticated nanofabrication techniques, feature sizes approaching tens of nanometers are being designed reliably, and light can be confined to an unprecedented small volume, enabling strong light-matter interaction [5]. The solution involves using a hybrid particle state between electrons and photons, which is known as ‘surface plasmon’ (SP), to operate at a nanoscale [6,7].

Surface plasmons (*i.e.* collective oscillation of electrons), have received much attention over the past two decades, due to their significant properties, such as smaller mode volume, strong mode confinement, and tight localisation [8–16]. SPs can be generated in a metal-dielectric surface where the real part of the complex permittivity of the plasmonic metal is negative and relatively small compared to its imaginary component. However, this oscillation can not be sustained due to the Joule losses associated with the plasmonic metal. Therefore, gain must be introduced to achieve continuous generation of SPs.

Similar to lasers, surface plasmon amplification through stimulated emission of radiation (spaser) was introduced by Stockman and Bergman in 2003 [6]. A spaser is not only a loss compensator; it can be used as an optimal source of coherent SPs, an SP amplifier, and an SP modulator which can interconnect with other plasmonic nano-circuitries.

A spaser, as the nanoplasmonic counterpart of a laser, shares many common structural components. It is made by coupling a nanoparticle (resonator) with a gain (active) medium. In a spaser, photons are replaced with SPs and the cavity is replaced with a nanoparticle. This compensates for the optical losses in the metal by overlapping gain in the active medium with the SP eigenmodes of the plasmonic nano-system and provides localised, intense, and coherent optical fields [17–19]. The operation of a spaser requires

---

non-radiative energy transfer from the gain medium to the resonator [6,19–21] (more details are discussed in Chapter 2).

Spasers have been the subject of intensive research over the past ten years and this research has demonstrated that they are well suited for room and low temperature electronics [19,22,23]. While theoretical models offer comprehensive insight into the physics of spasers, they usually do not provide options such as dynamic and transition analysis in addition to studying device performance. For this reason, a framework for analysing the steady state and dynamic responses of a spaser configuration is essential [24]. Advanced simulation tools are therefore necessary for further analysis and optimisation of these devices. Many theoretical models of spasers have recently been developed including a V-shaped metallic structure surrounded by quantum dots [6], an electrically pumped spaser made of silver and gold nanoparticles that works at extreme quantum limits [17], an electrically pumped bowtie spaser [25], a silver nanoparticle coupled to an externally driven three level gain medium and a quasi-classical model [26]. An experimental demonstration of stimulated SP emissions using a spherical gold nanoparticle surrounded by dye-doped silica was the first practical realisation of the spaser [27]. Spasers can be categorised according to their features and the materials used. Furthermore, spasers are classified by confinement as one-dimensional [28], two-dimensional [29] and three-dimensional [30]. According to the pumping method, they can also be further divided into two categories, optically pumped spasers [22] and electrically pumped spasers [17].

In addition, the energy transition between the gain medium and the resonator, and the different types of gain mediums and resonators have been analysed in recent studies [19,22]. The ability to use quantum dots, rare earth ions, carbon nanotubes and quantum well structures as the gain medium is considered in most of the studies. Moreover, using graphene and molybdenum disulde as the resonator in spasers instead of metallic nanoparticles such as gold and silver; is an emerging trend because of its enhanced operational characteristics, low threshold gain requirements, a high plasmon quality factor ( $Q$ ) and easy tuning capabilities [19,31,32]. The possibilities, such as larger tuning range,

tight localisation of output and more efficient output are raised due to the desirable dispersion relationships of graphene and molybdenum disulfide [5, 33, 34].

Graphene, a two-dimensional form of carbon in which the atoms are arranged in a honeycomb lattice, offers many of the advantages of carbon materials including mechanical strength and flexibility, and chemical and thermal stability [22, 33, 35–43]. A striking feature of graphene is that; doping has a strong effect on its optical properties [5, 33, 34, 44]. Due to the high electron mobility of graphene, doped graphene demonstrates plasmonic properties and a high quality factor [33, 34]. In addition, graphene provides an opportunity to obtain coherent optical fields of high concentration and intensity because of the unprecedented tight localisation of local plasmonic fields [5, 22, 33, 34, 44–46]. Spasers made of graphene are important in the field of nanoelectronics. Therefore, experimental creations of graphene-based nano devices with improved characteristics are prevalent. Nano-fabrication techniques for fabricating graphene have also been improved. Consequently, it is important to analyse the improved performances of graphene-based spasers.

Regarding the unique electronic properties of the most widely studied two-dimensional material graphene, researchers are seeking similar or better properties in other layered materials which could eventually be integrated into the current nano-electronic technology. In the past silicon was the most important element used in semiconductor technology, but it has recently been replaced with graphene in optical electronics due its better optical properties [33, 34]. Therefore, the prospect of a replacement counterpart for graphene such as molybdenum disulfide [31, 47–55], Plasmene [56] or Black Phosphorus [57, 58], is intriguing from a physical point of view for possible integration into nanoelectronic devices.

Since  $\text{MoS}_2$  is the strongest contender for graphene replacement in electrical and optical applications, it is worth modelling and analysing the characteristics of a device made of  $\text{MoS}_2$  to increase efficiency. Due to the large tunability ranges such as the high doping (ultra-doping) range, large free charge carrier mobility and direct bandgap, plasmons in

MoS<sub>2</sub> have recently received increased attention over graphene [32,59,60]. Furthermore, details about the optimum design parameters of MoS<sub>2</sub> based spasers are essential to developing ultra-speed nano-optical devices with increased efficiency. Although, materials such as graphene are appealing, chipmakers would likely prefer a two-dimensional alternative that would allow them to continue using similar materials without contaminating their fabrication process [31,56]. Thus, it is necessary to characterise the designs based on graphene, in addition to other two-dimensional plasmonic materials. However, due to the lack of appropriate approaches, little is known about the characteristics of two-dimensional nano-resonator-based spasers. Improving the performances of spasers requires a comprehensive understanding of the on-going processes. Therefore, this study analysed characteristics of active nanoplasmonic sources based on graphene and molybdenum disulfide to fill the knowledge gaps.

## 1.1 Aims of the research

### 1. Model and analyse characteristics of a simple graphene spaser.

Much research has been conducted to analyse the performance of graphene spasers. Since, the operational characteristics of a graphene spaser depend on its geometric and material parameters, it is essential to analyse how geometry and material parameters affect the operational characteristics of a spaser. In addition, it is necessary to analyse the localised plasmon modes that can be supported by a particular resonator given its degenerated modes. This can be analysed by implementing a theoretical model for a graphene spaser.

### 2. Analyse continuous wave (CW) operation of spasers.

By improving the developed theoretical model, a comprehensive study can be performed on how the material and geometrical parameters affect the CW operation of the spaser. An analytical model is required to be derived to determine the plasmonic modes, the mode energies, the threshold gain required for its continuous

operation, the quality factor and the efficiency of the device.

**3. Study ultra-fast dynamics of spasers.**

A spaser can be used not only as a coherent plasmonic source, but also as an SP modulator or amplifier. Using a spaser as an amplifier or modulator requires an analysis of dynamic behaviour of the system in addition to continuous wave operation. These characteristics are based on both the resonator and the gain system and must be analysed extensively to obtain an improved and an accurate model. This model can be used to analyse the performance of the spasers and enhance its ability to use spasers in many different potential applications.

**4. Design optimisation of spasers.**

The operating characteristics of a spaser, such as plasmonic modes and mode energy, the Q-factor, and the electric field output, depend on its geometric and material parameters. It is important to study how to improve the performance of a spaser with different geometries and materials for different spaser configurations. These conditions can be analysed through a comprehensive analytical model, aided by detailed numerical and graphical simulations.

**5. Examine the potential for materials to be used as a resonator for spasers.**

Graphene is a material that has better optical characteristics than other materials used for plasmonics, such as noble metals. Other two-dimensional materials such as molybdenum disulfide can also be used as a replacement for graphene with better optical properties than graphene. Therefore, an analysis must be performed to determine resonator-gain medium interactions for different spaser configurations using different plasmonic materials. This analysis would improve output and operational characteristics of spasers.

**6. Study the applicability of spasers to biomedical applications.**

Previous work on spasers has shown that using spasers in cancer treatment can

be an ideal alternative to chemotherapy. The current spaser designs are primarily based on heavy metals, such as gold, silver, and doped graphene. Furthermore, most of the other two-dimensional plasmonic materials must also be doped to achieve plasmon resonance in commercially useful wavelengths. This reduces the applicability of current spaser designs in biomedical applications such as chemotherapy. Therefore, use of non-doped non-toxic materials are a better choice for these applications and an analysis must be implemented to identify designs made of non-doped materials.

**7. Implement a set of comprehensive design guidelines for two-dimensional resonator based spasers.**

Considering the operational characteristics, the optical properties and the fabrication constraints of the device, designing a comprehensive set of guidelines to implement spasers with improved performance, considering geometric constraints is the final step in this research. This step would provide a set of comprehensive design guidelines to design and optimise spasers.

## 1.2 Thesis Outline

This thesis consists of eight chapters and two appendices. The chapters are organised as follows:

Chapter 1 introduces the topic of the research, briefly discussing recent advancements and trends associated with spaser technology. This chapter provides the details of the motivation and the aims, followed by the objectives of the current research.

Chapter 2 presents the background theory of the spaser, including its design and components, how it works, major operational characteristics, and a description on the evolution of spasers.

Chapter 3 provides derivations of analytical equations associated with the quantum mechanical model of a simple spaser configuration, including the motion equations associated with it. In addition, this chapter demonstrates the necessary equations for analysing operational characteristics of the designs. The ability to use two-dimensional plasmonic materials, such as graphene and  $\text{MoS}_2$ , as plasmonic materials in spaser setups is described in Chapter 4. This chapter presents permittivity models that are associated with each plasmonic material with derivations of equations. Moreover, it provides details of the developed framework to analyse two-dimensional resonator based spaser configurations.

Chapter 5 illustrates the configuration and the operational characteristics of an electrically pumped, circular graphene spaser with a quantum cascade well as the gain element. This chapter also discusses the ultra-fast dynamics of graphene based spasers, while considering different types of graphene, mono-layer graphene and bilayer graphene, which demonstrates the dynamics of an un-doped graphene based spaser. Design considerations of all the spaser configurations, their tuning capabilities and optimum configurations are extensively described in the later sections of this chapter.

Furthermore, Chapter 6 reports a detailed study on a spaser that is based on Molyb-

---

denum disulfide. This provides design guidelines along with a comprehensive analysis of a vertical cavity surface emitting laser (VCSEL) pumped, circular, MoS<sub>2</sub> based spaser.

Design guidelines for building spasers based on their applicability and output characteristics are presented in Chapter 7. This chapter also includes a discussion of potential real world applications of the proposed designs.

Finally, Chapter 8 concludes this thesis by presenting a summary of the major outcomes and vital contributions of this research towards active plasmonic nano-sources followed by a discussion of suggested future work.



# Chapter 2

## Theory of spasers

**A** SPASER, a non-diffraction limited configuration can be used as a coherent surface plasmon (SP) source, amplifier, or modulator. Unlike a laser, its critical dimensions are much smaller than half of its operating wavelength ( $\ll \lambda/2$ ), and is typically, in the order of a few nanometres to hundreds of nanometres (from  $\sim 10$  nm to  $\sim 100$  nm). Moreover, miniaturised nanoplasmonic systems in the nanometre scale (*e.g.* hundreds of nanometres) are being developed with plasmonics. A spaser, as the nanoplasmonic counterpart of a laser, shares many common structural components with a laser resonator. Similar to a laser, a spaser is made by coupling a nanoparticle (resonator) to a gain (active) medium; photons are replaced by surface plasmons (SP) and the cavity is replaced by a nanoparticle [6, 61]. A spaser must compensate for the intrinsic optical losses in the plasmonic resonator with energy received from an external source via its gain element, which is then transferred non-radiatively to the resonator [6, 19–21]. Some optical modes of the resonator, which also overlap with the SP's eigenmodes of the plasmonic nanosystem, survive this process and are responsible for the spaser field [17–19]. Further details are provided in the following sections.

### 2.1 Design and components

A spaser consists of a nano-resonator, a gain medium, and a pumping source, which can be either electrically or optically pumped. The schematic diagram of the components and the basic operational principle of a simple spaser is shown in Figure 2.1. Plasmons are generated on the surface of the nano-particle. A set of material parameters should be

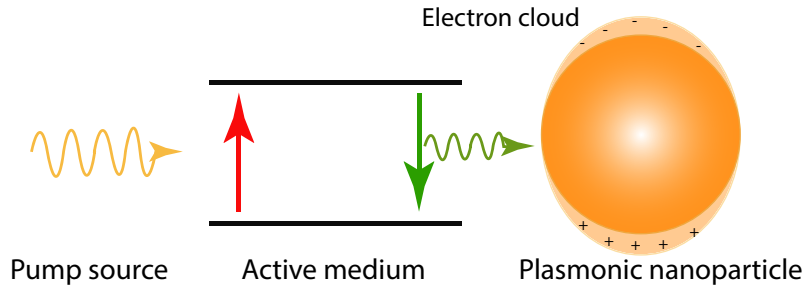


Figure 2.1: Main components and operation of the spaser.

satisfied for plasmons to exist on a nanoparticle:

$$\text{Re}(\epsilon_m) < 0, \quad \text{Im}(\epsilon_m) \ll -\text{Re}(\epsilon_m), \quad (2.1)$$

where  $\epsilon_m$  is the complex permittivity of the nanoparticle which depends on its operating wavelength. The most popular plasmonic materials used for spaser designs are gold, silver, aluminium and graphene. This thesis introduces the use of a new potential material for spaser designs as an alternative to graphene, molybdenum disulfide ( $\text{MoS}_2$ ). In terms of the dimensions of the nanoparticle, the size of the resonator can be a few nanometers to few hundreds of nanometers. The size of the nanoparticle is limited by its non-locality radius  $l_{nl} = V_F/\omega$  where,  $V_F$  is Fermi velocity of electrons in the metal and  $\omega$  is plasmon frequency, which is approximately one nm for noble metals such as gold and silver. The wavelength of the generated SPs depends on the size of the particle and further details are described in Chapter 4. To overcome losses associated with the plasmonic resonator, an active medium containing excited atoms must be placed near the resonator.

The most commonly used active mediums are quantum-dots, rare earth-ions, dye-molecules, nano-wires, quantum-wells and carbon nanotubes. Excited atoms in the active medium transfer energy non-radiatively to the plasmonic resonator and generate sustainable SPs. As the excited atoms are reduced to their ground state, releasing their energy to the plasmonic resonator, a continuous pump source is required to excite the atoms and provide continuous gain. Thus, an external pumping source is required to achieve continuous operation of the spaser. The pumping source excites the atoms. Two

main pumping mechanisms used in spaser designs are optical and electrical pumping. A laser that matches the frequency with the absorption of the active medium can be used as the optical pumping source, and a quantum well can be powered electrically via electrodes similar to semiconductor lasers.

## 2.2 Operation principles of a spaser

The concept of achieving plasmonic gain in a nanoparticle by stimulated emission was introduced by Bergman and Stockman in 2003 [6]. In plasmonic gain, the excited active medium of the spaser transfers energy non-radiatively to a closely positioned resonator to excite its localised plasmonic modes. Bergman and Stockman claimed that the SPs that initially existed in the system stimulate the active medium and multiply the number of generated SPs which is known as spasing. These systems generate intense, coherent and localised plasmonic fields that can be confined to a nanometric scale. During the operation of a spaser, electrons undergo several transitions. The energy flow diagram of a simple spaser configuration is shown in Figure 2.2.

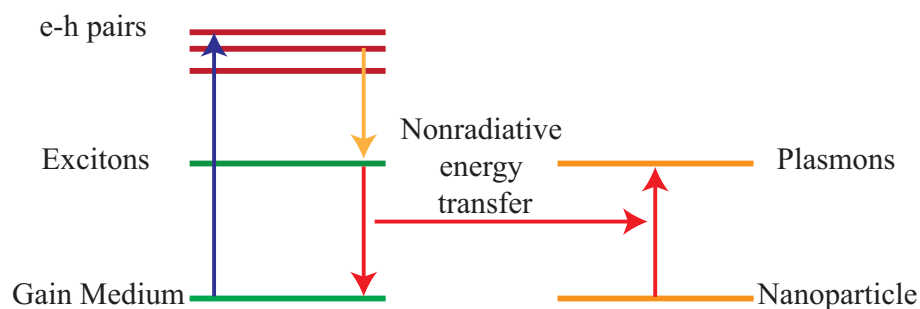


Figure 2.2: Energy transitions of a spaser.

Due to energy provided externally either by optical pumping or electrical pumping, an electron shifts to its higher energy state (blue arrow) and emanates back to a transitional state (yellow arrow) becoming an exciton. These excitons release energy and return to ground energy level emitting energy to the plasmonic resonator (red arrows). The non-radiatively transmitted energy generates plasmons in the nanoparticle and these excited

plasmons that are already in the resonator stimulate the gain medium and start a feedback mechanism to sustain the spasing phenomenon.

## 2.3 Background theory

A nano-system made of metal or semiconductor inclusions entrenched in a dielectric host was analysed by Stockman *et. al.* [21], which demonstrates that, the plasmonics modes  $[E_k(r)]$  of the resonator can be derived from,

$$\nabla \cdot [\Theta(r) - S_n] \nabla E_k(r) = 0, \quad (2.2)$$

where  $\Theta(r) = 1$  inside the inclusions and 0 outside the inclusions and is called the characteristics function. Moreover, the SP mode frequency  $\omega_n$  that satisfies  $S(\omega_n) = S_n$ ,  $S(\omega)$  is the Bergman's spectral index, which has the following form:

$$S(\omega) = [1 - \epsilon_m(\omega)/\epsilon_d]^{-1} \quad (2.3)$$

where,  $\epsilon_m(\omega)$  is the wavelength dependent complex permittivity of plasmonic material and  $\epsilon_d$  is the permittivity of the surrounding dielectric. These SP frequencies are complex,  $\omega = \omega_n - i\gamma_n$ , with the real frequency  $\omega_n$  and relaxation rate  $\gamma_n$ . The SP lifetime is one of the major parameters for the continuous operation of the spaser. For weak relaxation, ( $\gamma_n \ll \omega_n$ ),  $\omega_n$  satisfies the relationship of:

$$\text{Re}[s(\omega_n)] = s_n, \quad (2.4)$$

and the amplitude of the spontaneous decay rate of SPs ( $\gamma_n$ ) at frequency  $\omega_n$  is derived by:

$$\gamma_n(\omega_n) = \text{Im}\epsilon_m(\omega_n) \left[ \frac{\partial \text{Re}\epsilon_m(\omega_n)}{\partial \omega_n} \right]^{-1}. \quad (2.5)$$

A spaser is considered as a simple harmonic oscillator that has a Hamiltonian ( $H$ ) of:

$$H = \sum_n \hbar \omega_n \left( a_n^\dagger a_n + \frac{1}{2} \right), \quad (2.6)$$

where  $a_n^\dagger$  and  $a_n$  are plasmon creation and annihilation operations respectively and  $\hbar$  is the reduced Planck's constant. Moreover, the threshold gain ( $g_{\text{th}}$ ) required for spasing at frequency  $\omega$  was studied and has the following form,

$$g_{\text{th}} = \frac{\omega}{c\sqrt{\epsilon_d}} \frac{\text{Re}[s(\omega)]}{1 - \text{Re}[s(\omega)]} \text{Im}[\epsilon(\omega)], \quad (2.7)$$

where  $c$  is the speed of light,  $\epsilon_d$  is the permittivity of the surrounding dielectric, and  $s(\omega)$  is the Bergman's spectral index.

## 2.4 Insight in to the history of spasers

### 2.4.1 Theoretical work on spasers

The work of Bergman and Stockman constitutes the initial theoretical discussion of spasers. Their initial design consisted of a V-shaped, nano sized metallic inclusion with an active medium (QDs). The proposed V-shaped spaser is shown in Figure 2.3.

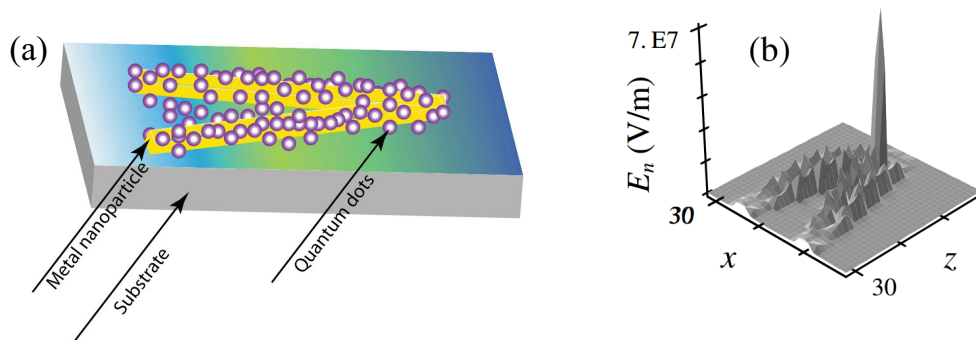


Figure 2.3: a) Spaser made of V-shaped metallic inclusion surrounded by quantum dots. b) Electric field output of the system for energy  $\hbar\omega_n = 1.18$  eV [6].

The V-shaped metal particle is surrounded by two-level quantum emitters. This

spaser does not emit light as it transfers energy to the metallic nanoparticle non-radiatively and is transformed into the quasi-static electric field energy of SPs.

Over the past decade, there has been increased interest in spasers due to their unprecedented properties. As described in Section 2.1 little analysis has been done on electrically pumped spasers. An electrically pumped plasmonic semiconductor nanolaser based on a metallic bowtie structure is described in reference [25] and shown in Figure 2.4. In the design, the curvature effect of the bowtie tips provides added field en-

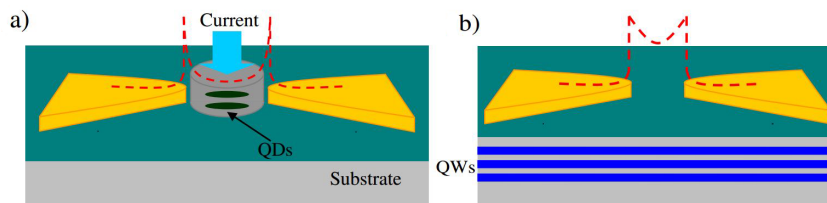


Figure 2.4: Electrically pumped bowties spaser design powered by a) Quantum dots b) Multiple quantum wells (MQW) [25].

hancement between the bowtie gap and further reduces the modal volume. Hence, the size of the active region can be reduced, significantly decreasing the threshold operating current. In addition, the field enhancement, which occurs because of the small modal volume at the gap may overcome the material and radiation losses by increasing both spontaneous and stimulated emission rates thus making the spasing action possible.

An investigation into surface plasmon amplification in a silver nanoparticle coupled to an externally driven three level gain medium was conducted by Konstantin *et al.* [62]. They demonstrated that, quantum coherence significantly enhances the generation of SPs. Surface plasmon amplification by stimulated emission of radiation was accomplished in the absence of population inversion on the spasing transition. This process decreased the pumping requirements of the design. Additional degrees of freedom for the control of quantum dynamics were achieved with this scheme using a coherent drive.

Several models have been developed over the past two decades to analyse the perfor-

mance of spasers, including an exact solvable quasi-classical model for a spaser [26]. A medium with nonlinear permittivity and negative losses was used as the gain medium and the main features of the spaser were demonstrated within the study. A self-oscillating state (spasing), arising without an external driving field if the pumping exceeds some threshold value was considered in this analysis. Synchronization of a spaser by an external field within the Arnold tongue, and the possibility of compensating for Joules losses (when the pumping is below threshold) were also analysed and described in this study.

A few possible applications of spasers have been analysed in recent studies and a set of nano-antennas made of spasers was theoretically analysed by Zhong *et al.* [63]. The device was made of a plasmonic nano-antenna embedded with an active medium and the model was treated semiclassically. The model was incorporated with four-level atomic rate equations including the classical oscillator model for the active medium. A large Purcell factor and low absorption loss leading to a low threshold spaser, are advantages of nano-antennas made of spasers. Operating characteristics, including enhancement of the local electric field, gain, the saturation phenomenon and the lasing threshold were discussed using the developed theory.

Furthermore, a theoretical model for electrically pumped spasers was analysed by Dabing Li and Mark Stockman [17]. The design used quantum wires to provide energy to the active medium, and the analysis investigated extreme quantum limits. Gold, silver, and aluminium nanoparticles were considered for the analysis and silver particles produced productive output with a lower current threshold and higher mode energies compared to the other materials considered.

#### 2.4.2 Experimental realisations of spasers

An experimental demonstration of stimulated SP emission using a spherical gold nanoparticle surrounded by dye-doped silica has been recorded as the first practical implementation of the spaser [27]. the design is shown in Figure 2.5.

A gold nanoparticle with a 44-nm diameter and a dye-doped silica shell were used

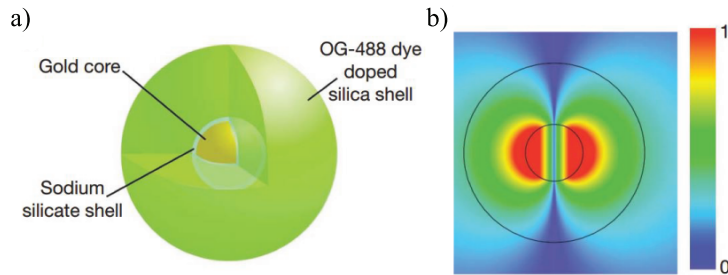


Figure 2.5: a) Schematic of the first experimental realization of spasers made of silver nano particle surrounded by dye-doped silica. b) Normalized electric field output of the spaser [25].

in the assembly, which allowed the proposed design to overcome the losses associated with localised surface plasmons by inserting gain media, producing a spaser. This device can support photonic modes at a wavelength of 531 nm due to optocoupling of surface plasmon oscillation, and this is the first and smallest experimental nanolasers operate at visible wavelengths.

A spaser that is made by inserting a gold-film plasmonic waveguide between optically pumped InGaAs quantum-well gain media is demonstrated in reference [64]. This device supports transverse magnetic plasmon waves with gain narrowing. Furthermore, it produces a mirror feedback provided by cleaved facets in a one mm long cavity fabricated with a flip-chip approach. This spaser is readily applicable to electronic operations on an integrated microchip.

Martin *et al.* [28] demonstrated lasing in metal-insulator-metal (MIM) waveguides filled with electrically pumped semiconductor cores, with core width below the diffraction limit. Furthermore, these waveguides propagate a transverse magnetic (TM), which is referred to as gap plasmon mode. Hence, losses in sub-wavelength MIM waveguides can be overcome to create small plasmon mode lasers at wavelengths near 1500nm. Transverse electric (TE) modes were supported in approximately 310 nm wide semiconductor cores at room temperature.

An experimental demonstration of nanometre-scale plasmonic lasers, which gener-

ated optical modes that are one hundred times smaller than the diffraction limit, is presented in [29]. The design is a nanolaser made of a hybrid plasmonic waveguide. This nanolaser consists of a high-gain cadmium sulphide semiconductor nanowire which is separated from a silver surface by a five nm thick insulating gap. Due to strong mode confinement of the laser, an emission enhancement of the nanowire's exciton spontaneous emission rate up to six times was observed . In addition to these conditions, a lower lasing threshold was achieved. Lower operating threshold of the laser was clarified by the direct measurements of an emission lifetime. Down-scaling of the lateral dimensions of both the device and optical mode were demonstrated due to the lack of a cut off for the plasmonic modes. The schema of the design is shown in Figure 2.6:

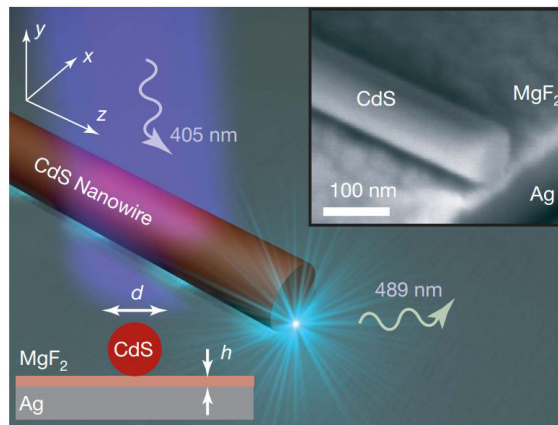


Figure 2.6: Schematic diagram of the two dimensionally confined spaser from [29].

Ren-Min *et al.* [30] presented a room-temperature semiconductor sub-diffraction-limited laser. This system was designed by adopting total internal reflection of surface plasmons to mitigate the radiation loss. Furthermore, strong light confinement with low metal losses were achieved using hybrid semiconductor-insulator-metal nanosquares. High cavity quality factors, approaching 100, along with strong  $\lambda/20$  mode confinement were reached, leading to enhancements of spontaneous emission rates by up to 18-fold. Single-mode lasing was achieved by controlling the structural geometry due to the reduced number of cavity modes. The electric field of this spaser was confined to all three dimensions.

### 2.4.3 Spasers made of graphene

Graphene is a promising material that has extraordinary optical properties in addition to properties such as mechanical strength and thermal stability. Graphene is a two dimensional form of carbon. thus, it contains properties that are inherent to carbon. Furthermore, doping would affect the optical properties of graphene, such as frequency dependent optical conductivity [5, 33, 34, 44]. Due to the high electron mobility of graphene, doped graphene demonstrates plasmonic properties with high quality factors [33, 34]. Graphene provides an opportunity to obtain coherent optical fields of an extremely high concentration and intensity because of the unprecedented tight localisation of local plasmonic fields [5, 22, 33, 34, 44–46]. Therefore, much research has focused on graphene spasers to improve performance.

The amplification of SPs in a doped graphene nanoribbon was proposed in reference [65]. Due to the non-radiative excitation by emitters, the plasmons in the THz region could be generated in a doped graphene nanoribbon. The active medium was modelled as a two-level quantum generator. Furthermore, the minimal population inversion per unit area, needed for the net amplification of SPs in a doped graphene nanoribbon was obtained. The dependence of the minimal population inversion on the surface plasmon wavevector, the graphene nanoribbon width, and the doping and damping parameters that are necessary to amplify surface plasmons in an armchair graphene nanoribbon were studied in the analysis.

In addition, a spaser based on carbon was proposed by Rupasinghe *et al.* [22]. A square graphene flake was used as the resonator and a carbon nanotube was used as the gain element. This theoretically demonstrated the ability to transfer energy non-radiatively from an excited carbon nanotube to a graphene sheet . Localised plasmon modes, mode energy alterations, the quality factor and the threshold gain required for continuous spasing were analysed. The plasmon generation rate was also examined under this analysis. The schematic diagram of the design is shown in Figure 2.7.

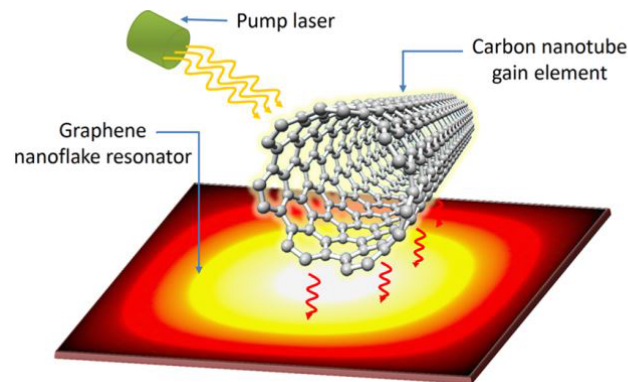


Figure 2.7: Schematic diagram of the proposed spaser made of an optically pumped carbon nanotube located above a square graphene nanoflake resonator [22].

There are several materials that can be used as a gain medium for a spaser, such as quantum dots, quantum wells, rare earth ions, and carbon nanotubes. A spaser powered by a quantum cascade well was theoretically modelled by Apalkov and Stockman in 2014 [19]. The schematic diagram of the proposed graphene nanospaser is shown in Figure 2.8. The design supports plasmons with a higher quality factor because of the in-

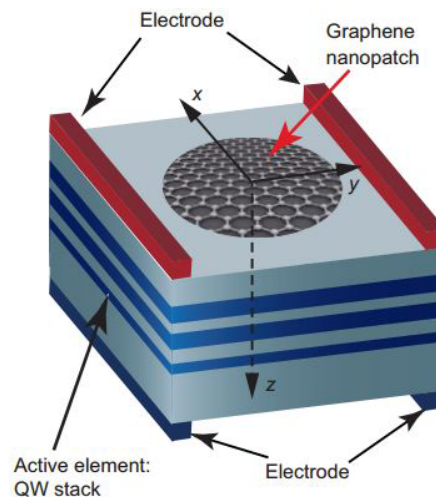


Figure 2.8: Schema of a graphene quantum cascade nanospaser: monolayer graphene nanopatch on top of a stack of quantum cascade wells and electrodes for electric pumping [19].

herent properties of graphene. In addition, it has more advantages than other nanolasers,

because of the features of its quantum-cascade-well structure, such as its thermal and mechanical stability and ease of tuning. The device can be operated in the Mid-IR range and may be an ideal nanoscale optical source in optoelectronics.

# Chapter 3

## Quantum mechanical model of a spaser

**A** QUANTUM mechanical model of a simple spaser based on a circular resonator is discussed in this chapter. A simple spaser configuration consists of two main subsystems, a plasmonic subsystem and a gain subsystem. Here, the gain subsystem is treated quantum mechanically and the plasmonic subsystem is treated quasi classically.

### 3.1 The Hamiltonian of a spaser

The Hamiltonian of a spaser consists of three components: the Hamiltonian of the gain system ( $H_g$ ), the plasmonic system ( $H_{pl}$ ), and the interaction Hamiltonian ( $H_{int}$ ).

$$\mathbf{H} = \mathbf{H}_g + \mathbf{H}_{pl} + \mathbf{H}_{int}(t) , \quad (3.1)$$

The Hamiltonian of the two-level gain medium can be expressed in bra-ket notation as:

$$\mathbf{H}_g = \hbar \sum_{j=1,2} \omega_{j_g} |j_g\rangle \langle j_g| . \quad (3.2)$$

In addition, the corresponding Hamiltonian of the plasmonic system can be expressed as:

$$\mathbf{H}_{pl} = \hbar \sum_n \omega_{pl_n} \hat{a}_n^\dagger \hat{a}_n , \quad (3.3)$$

where,  $\hat{a}_n^\dagger$ , and  $\hat{a}_n$  are SP creation and annihilation operators respectively. To calculate the emissions under resonance excitation, it is sufficient to explicitly consider the interaction

operator  $H_{int}$ . The interaction Hamiltonian can be obtained as follows [1,21],

$$\mathbf{H}_{int} = \sum_p -E_{sp}(\mathbf{r}_p) \mathbf{d}^{(p)}, \quad (3.4)$$

where,  $\mathbf{r}_p$  is the position of  $p^{\text{th}}$  gain chromophore and  $\mathbf{d}^{(p)}$  is dipole moment of the two-level system associated with the  $p^{\text{th}}$  chromophore.

### 3.2 Motion equations

The motion equations of the spaser can be derived considering their interaction picture Hamiltonian. The relationship between the population inversion of the gain medium and the corresponding density matrix elements associated with the energy transitions between gain and plasmonic subsystems are obtained using the density matrix formalism related to laser physics [21]. Hence, the plasmon creation operator is explained by:

$$\hat{a}_{np} = a_{0np} e^{-i\omega t}, \quad (3.5)$$

where,  $a_{0np}$  is a slow varying amplitude and the number of SPs generated per SP mode is obtained from  $N_{np} = |a_{0np}|^2$ . Then, considering the  $\rho^{(p)}$  as the density matrix of a  $p^{\text{th}}$  chromophore and using Liouville's equation  $\frac{d\rho}{dt} = \frac{i}{\hbar} [\hat{p}, \hat{H}]$ , the motion equations associated with the configuration are explained. Standard rotating wave approximation (RWA) is also considered. In this procedure, high frequency oscillations were omitted and the resonance between the gain system and the resonator was taken into account for. A rate constant, a polarization relaxation time ( $\Gamma_{12}$ ) is introduced and population inversion between the excited level and the ground level is considered as  $n_{21} = \rho_{22} - \rho_{11}$ . Therefore, the equation of the motion for the non-diagonal element of the density matrix ( $\rho_{12}$ ) is derived as the following equation:

$$\frac{d\tilde{\rho}_{12}}{dt} = -[i\Delta_{12} + \Gamma_{12}]\tilde{\rho}_{12} + in_{21}\Omega_{12} \quad (3.6)$$

where,  $\Omega_{12}$  is the single plasmon Rabi frequency and  $\Delta_{12} = \omega - \omega_{12}$ . The single plasmon Rabi frequency has the following form.

$$\Omega_{12} = -E_{np} \mathbf{d}_{12}^{(p)} \nabla \varphi_{np}(\mathbf{r}_p) / \hbar . \quad (3.7)$$

By careful design,  $\mathbf{d}_{12}$  can be made real, resulting in a real value for  $\Omega_{12}$ .

Similarly, by considering the Liouville's equation above, a motion equation for the population inversion ( $n_{21}$ ) is derived using the diagonal elements of the density matrix ( $\rho_{11}$  and  $\rho_{22}$ ).

$$\frac{d\tilde{n}_{12}}{dt} = -4i(\tilde{\rho}_{12}\Omega_{12}) - \gamma_2(1 + \tilde{n}_{21}) + g(1 - \tilde{n}_{21}) , \quad (3.8)$$

where,  $g$  is the pump rate of the external source which pumps the atoms from the ground state  $|1\rangle$  to the excited state  $|2\rangle$  and  $\gamma_2$  represents the decay rate for the  $|2\rangle \rightarrow |1\rangle$  transition. By adding the SP relaxation rate  $\gamma_{np}$ , the motion equation for the stimulated emission of the SPs is obtained as:

$$\frac{da_{0np}}{dt} = (i\Delta_{np} - \gamma_{np})a_{0np} + i \sum_p \tilde{\rho}_{12} \Omega_{12} \quad (3.9)$$

where,  $\Delta_{np} = \omega - \omega_{sp}$ .  $\gamma_{np}$  is a frequency dependent parameter that also depends on the material of the resonator and can be calculated from its permittivity as described in the equation 2.5

### 3.3 Continuous wave (CW) operation

Considering equations (3.6)-(3.9), the equations for the continuous wave (CW) operation of the spaser can be obtained as follow:

$$\frac{(\gamma_{np} + \Gamma_{12})^2}{\gamma_{np}\Gamma_{12}[(\gamma_{np} + \Gamma_{12})^2]} \sum_p |\tilde{\Omega}_{12}|^2 n_{21} = 1. \quad (3.10)$$

$$n_{21} = \frac{g - \gamma_2}{\left[ g + \gamma_2 + \frac{4N_{np} |\tilde{\Omega}_{12}|^2 (\Gamma_{12} + \gamma_{np})}{\Delta^2 + (\Gamma_{12} + \gamma_{np})^2} \right]}. \quad (3.11)$$

Moreover, the spasing frequency  $\omega_{sp}$  can be derived by:

$$\omega_{sp} = \frac{\gamma_{21} \omega_{sp} + \Gamma_{12} \omega_{np}}{\gamma_{np} + \Gamma_{12}} \quad (3.12)$$

Given the population inversion (since,  $n_{21} \leq 1$ ) of the spaser and the motion equations described by equations 3.6 with 3.8, a condition for continuous spasing can be obtained as [18, 21],

$$\frac{(\gamma_n + \Gamma_{12})^2}{\gamma_n \Gamma_{12} [(\omega_{12} - \omega_{sp})^2 + (\gamma_n + \Gamma_{12})^2]} \sum_k |\Omega_{12}|^2 \geq 1, \quad (3.13)$$

at resonance  $\omega_{12} = \omega_{sp}$ , therefore, a necessary condition for spasing in a spaser can be obtained accordingly. The necessary conditions for each design that is considered in this thesis are described extensively in Chapter 5 and Chapter 6.

The number of SPs generated per unit time is another important parameter of a spaser. A design can be optimised to achieve higher SP generation rate according to the required specifications. Furthermore, the plasmon excitation rate of a spaser can be obtained from the following equation [22, 24],

$$\mathfrak{R}_{pl,k} = \alpha \omega_{sp}^2 \frac{\gamma_{2p}}{\gamma_{2p}^2 + (\omega_{12} - \omega_{sp})^2} |d_{13}^{(L)}|^2 \sum_{j=4}^n |d_{12}^{(K),j}|^2. \quad (3.14)$$

where,  $\alpha$  is the normalisation constant, and  $d_{12}^{(K),j}$  is the dipole matrix element that corresponds to the energy transition between the gain system and plasmonic nano-resonator.  $d_{13}^{(L)}$  is the corresponding matrix element for the transition between the pump and the gain system.

# Chapter 4

## Two-dimensional resonator-based spasers

**T**WO dimensional materials such as graphene and molybdenum disulfide have received attention from the researchers and opto-electronics industry during the past decade due to their optical properties. As described in Chapter 1, plasmonic properties of a spasers are based on its nano-resonator materials parameters and mainly on the wavelength dependent complex permittivity. Compared to other plasmonic materials such as gold and silver, doped graphene and molybdenum disulfide show improved plasmonic properties due to their desirable dispersion relation. Doping can also be used to tune the plasmonic characteristics of the materials unlike gold and silver.

### 4.1 Two-dimensional plasmonic materials

In addition to graphene and molybdenum disulfide, black phosphorus is an alternative plasmonic material with numerous plasmonic applications, such as ultra-thin nano-circuitries and on-chip designs. These two-dimensional materials can be used in plasmonic applications effectively since they can interconnect with other optical interconnections owing due to their two-dimensional geometry. In this chapter, the plasmonic characteristics of graphene and MoS<sub>2</sub> and their applicability to spaser designs are described.

### 4.1.1 Graphene

Graphene, a two-dimensional form of carbon in which the atoms are arranged in a honeycomb lattice, offers many advantages such as mechanical strength, chemical stability and thermal stability [22, 33]. The most striking feature of graphene is that doping has a strong effect on the optical properties [5, 33, 34, 44]. Due to the high electron mobility of graphene, doped graphene possesses plasmonics properties with high quality factors [33, 34]. Moreover, graphene provides the opportunity for obtaining coherent optical fields of extremely high concentration and intensities because of the unprecedented tight localisation of local plasmonic fields [5, 22, 33, 34, 44–46].

A circular graphene flake with a finite radius accommodates coherent, localised plasmon modes due to the properties of graphene [33, 34]. The plasmonic properties of graphene are based on its frequency dependent optical conductivity, which can vary widely at different infrared frequencies ( $0.75\mu\text{m} - 10\mu\text{m}$ ). These properties are derived from both intraband and interband contributions. At low doping limits (*i.e.*  $0 < E_F \ll \hbar\omega$ ), the interband transitions contribute significantly at higher frequencies. At high doping levels (*i.e.*  $\hbar\omega \ll E_F$ ), intraband transitions become dominant [34, 66]. Therefore, it is necessary to consider intraband and interband contributions when estimating the dynamic optical conductivity of graphene. In this study, both of the transitions were considered to analyse the model, using the Kubo formulas:[34, 66]

$$\sigma_{\text{intra}}(\omega) = \frac{ie_0^2|E_F|}{\pi\hbar^2(\omega + i\tau^{-1})}, \quad (4.1)$$

where  $e_0$  is the charge of an electron,  $E_F$  is the Fermi energy,  $\hbar$  is the reduced Planck's constant,  $\omega$  is the angular frequency of the mode and  $\tau$  is the intrinsic relaxation time of carriers at 300 K with an experimentally measured value of  $4 \times 10^{-13}$  s [67]. Interband conductivity is also approximated as [66, 68],

$$\sigma_{\text{inter}}(\omega) = \frac{ie_0^2}{4\pi\hbar} \ln \left( \frac{2|E_F| - (\omega - i\tau^{-1})\hbar}{2|E_F| + (\omega - i\tau^{-1})\hbar} \right). \quad (4.2)$$

These expressions are the Drude model for graphene.

From equations (4.1) and (4.2), two-dimensional (2D) graphene conductivity is obtained as follows:

$$\sigma_{2D}(\omega) = \sigma_{\text{intra}}(\omega) + \sigma_{\text{inter}}(\omega) , \quad (4.3)$$

$$\sigma_{3D}(\omega) = \sigma_{2D}(\omega)/d . \quad (4.4)$$

Equation 4.4 is used to obtain the conductivity of a three-dimensional graphene flake, where  $d$  is the thickness of the flake. Then, the permittivity of the material can be obtained with:

$$\epsilon(\omega) = \epsilon_0 \left( 1 + \frac{i\sigma_{3D}}{\omega_{\text{sp}}\epsilon_0} \right) , \quad (4.5)$$

where  $\epsilon_0$  is the permittivity of the vacuum and  $\omega_{\text{sp}}$  is the wavelength of the corresponding SP mode. The conductivity of graphene structures is dependent on the thickness of the layers.

This study considered two main graphene structures, mono-layer graphene (MLG) and bi-layer graphene (BLG). MLG can be formed by a single layer of graphene or two identical layers of graphene without considering energy binding between two layers (*i.e.* avoiding tunnelling effects) [69]. BLG is formed using two perfectly aligned and tightly bonded graphene layers (layer thickness is less than the MLG); tunnelling between two layers also has been considered [69]. the conductivity of MLG has a similar form to that explained in the previous section and is further explained by from the equations described in the following sections.

#### 4.1.1.1 Mono-layer graphene (MLG)

Although, graphene is typically an atomic thick layered material. double layer graphene can be designed by using two identical graphene single layers that act separately without having any interactions between layers (thickness of the layers  $\approx 0.46$  nm). This scenario

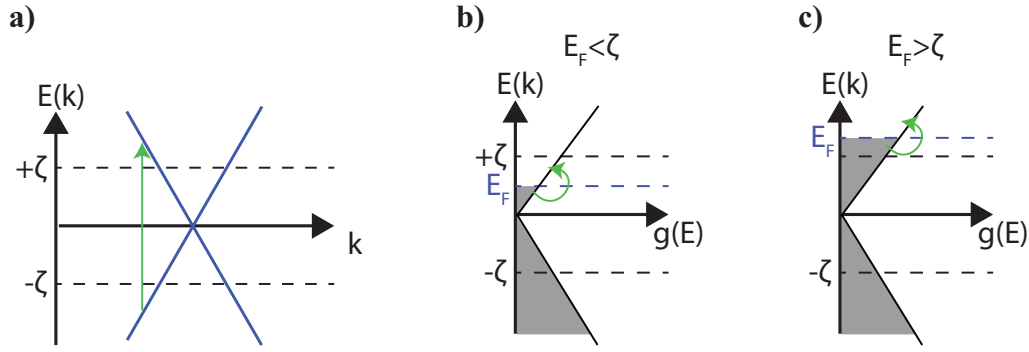


Figure 4.1: **a)** E-K diagram of Mono-layer graphene with allowed transitions. **b)** Energy / transition diagram when the Fermi level is lower than the energy gap between two layers ( $E_F < ζ$ ). **c)** Energy / transition diagram when the Fermi level is higher than the energy gap between two layers ( $E_F > ζ$ ).

is modelled by the bulk graphene conductivity formula and derived as:

$$\sigma_{\text{MLG}}(\omega) = \frac{ie_0^2}{\pi\hbar} \left\{ \frac{|E_F|}{\hbar(\omega + i\tau^{-1})} + \frac{1}{4} \ln \left[ \frac{2|E_F| - \hbar(\omega - i\tau^{-1})}{2|E_F| + \hbar(\omega - i\tau^{-1})} \right] \right\}, \quad (4.6)$$

corresponding energy diagrams are shown in Figure 4.1. This figure demonstrates that, there is no possible allowed transitions when the Fermi level stays in the middle of the energy gap (intrinsic graphene). When the material is sufficiently doped, either electrochemically or electrostatically, the system provides a set of allowed transitions as illustrated by the green arrows in the diagram. Thus, intrinsic mono-layer graphene does not provide plasmon resonance at zero doping.

The real component and imaginary components of the complex permittivity of MLG with respect to wavelengths from 600 nm to 3000 nm for different doping levels are shown in Figure 4.2 and figure 4.3 respectively. These figures demonstrate that for high doping limits, graphene satisfies the necessary condition of existing plasmon resonance at low wavelengths. lower doping limits, such as 0.1 eV, plasmon resonance can obtained at higher wavelengths ( $>2000$  nm). However, At the zero doping level, mono-layer graphene acts as an insulator.

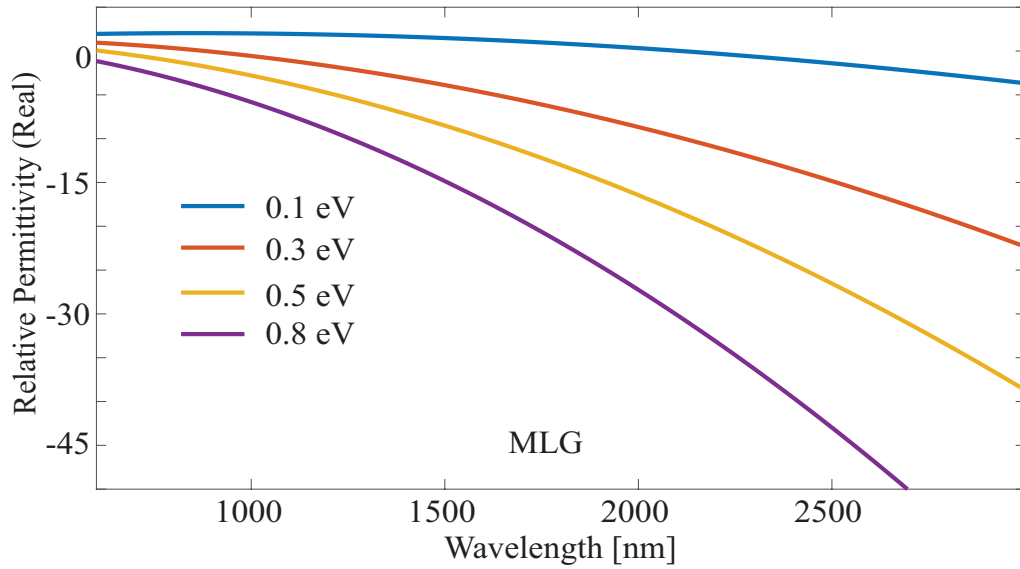


Figure 4.2: Real values of complex permittivity of mono-layer graphene with respect to wavelength for varying doping levels.

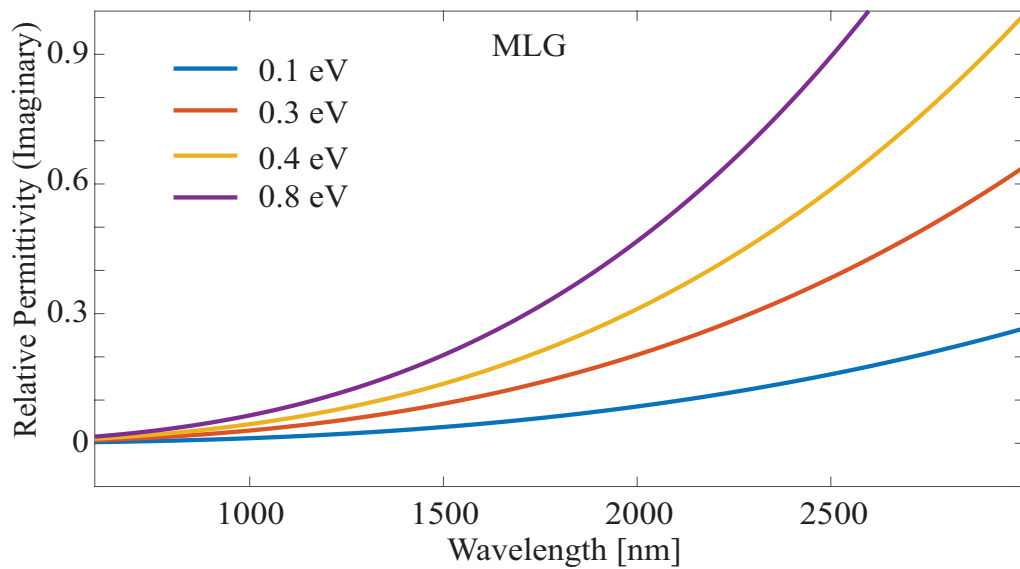


Figure 4.3: Imaginary values of complex permittivity of mono-layer graphene with respect to wavelength for varying doping levels.

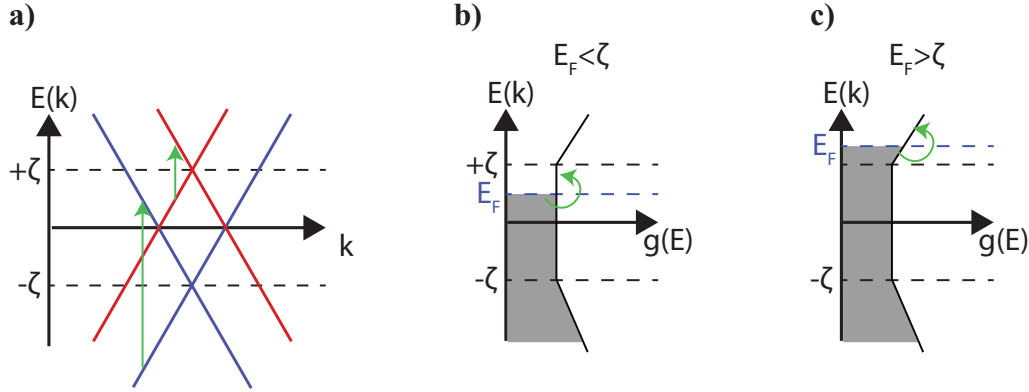


Figure 4.4: **a)** E-K diagram of bi-layer graphene with allowed transitions. **b)** Energy / transition diagram when the Fermi level is lower than the energy gap between two layers ( $E_F < \zeta$ ). **c)** Energy / transition diagram when the Fermi level is higher than the energy gap between two layers ( $E_F > \zeta$ ).

#### 4.1.1.2 Bi-Layer Graphene (BLG)

Similar to MLG, an equation for precisely aligned BLG can be obtained and was recently demonstrated in reference [69].

$$\sigma_{\text{BLG}}(\omega) = \frac{ie_0^2}{2\pi\hbar} \left\{ \frac{|E_F + \zeta| + |E_F - \zeta|}{\hbar(\omega - i\tau^{-1})} \right\} + \frac{ie_0^2}{8\pi\hbar} \left\{ \ln \left[ \frac{2|E_F + \zeta| - \hbar(\omega - i\tau^{-1})}{2|E_F + \zeta| + \hbar(\omega - i\tau^{-1})} \right] + \ln \left[ \frac{2|E_F - \zeta| - \hbar(\omega - i\tau^{-1})}{2|E_F - \zeta| + \hbar(\omega - i\tau^{-1})} \right] \right\}. \quad (4.7)$$

The conductivity of the BLG is a composition of its monolayer characteristics deviated from the difference of the energy gap between tightly bonded layers ( $\sigma_{\text{MLG}}(\omega - \zeta)$  and  $\sigma_{\text{MLG}}(\omega + \zeta)$ ). The layer thickness of BLG typically stays around  $\approx 0.36$  nm.

In Figure 4.4, allowed transitions in intrinsic BLG (green arrows) are visible, indicating that plasmons can be generated on the surface without doping the material. This condition is important because some of the spaser applications, such as biomedical applications, required to have non-toxic compounds. For that reason, the plasmonic resonator can not be doped. Therefore, the introduction of BLG is an ideal solution for creating bio-friendly spaser designs.

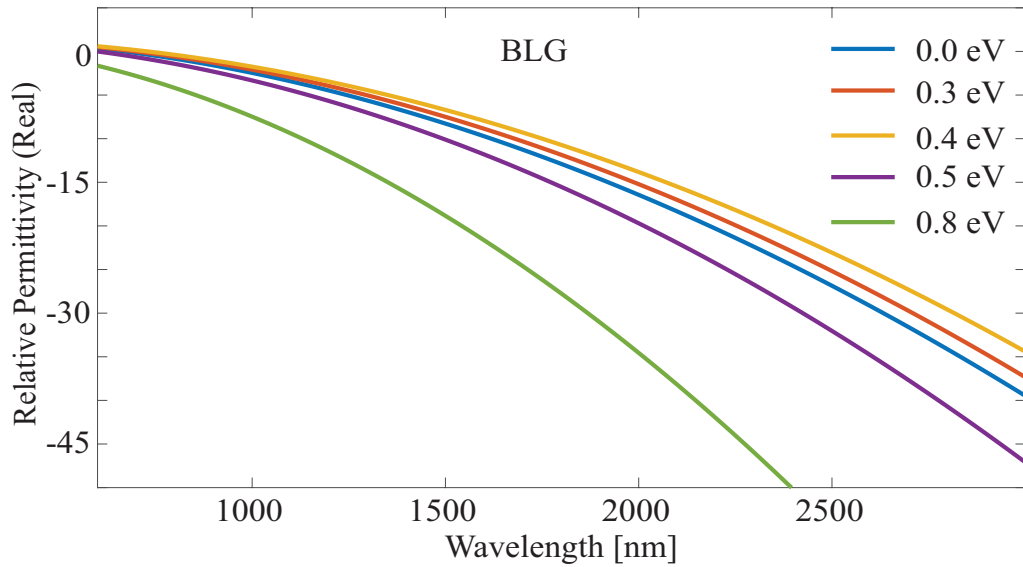


Figure 4.5: Real values of complex permittivity of bi-layer graphene with respect to wavelength for varying doping levels.

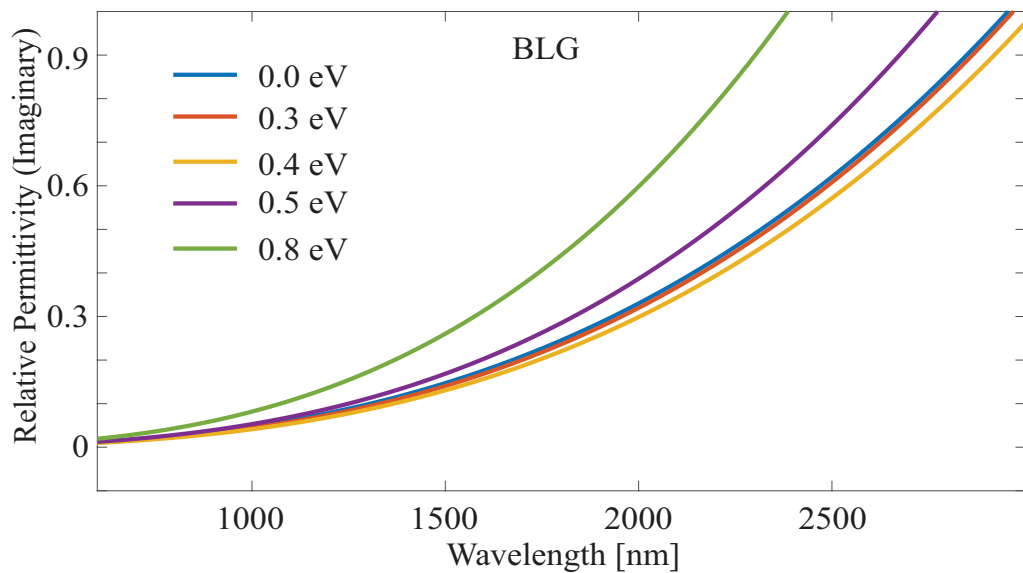


Figure 4.6: Imaginary values of complex permittivity of bi-layer graphene with respect to wavelength for varying doping levels.

The real component and imaginary components of BLG's complex permittivity with respect to wavelengths vary from 600 nm to 3000 nm for different doping levels are shown in Figure 4.5 and Figure 4.6 respectively.

According to Figures 4.2 - figure 4.6, in contrast to MLG, BLG has a random pattern of permittivity regarding doping limits due to the energy separation between BLG layers [69].

The permittivity equations above were used to model the graphene based spaser designs described in this thesis. Plasmon resonance frequency has non linear relationship with its geometrical parameters. In the graphene flakes considered in this study, the resonance frequency was tailored by varying the doping level and the radius of the flake. Resonance wavelengths of the resonators were found by modelling graphene in COMSOL Multiphysics and CST Microwave Studio. The resonance wavelengths obtained for different resonators can be found in Appendix A

### 4.1.2 Molybdenum disulfide

Molybdenum disulfide ( $\text{MoS}_2$ ) has emerged as one of the biggest contenders for a graphene alternative with many unique optical and electrical properties [1–3]. Unlike graphene,  $\text{MoS}_2$  consists of massive electrons. Therefore, the mobility of the electrons is lower than that of the electrons in graphene. However,  $\text{MoS}_2$  can accommodate many electrons within the layers and can achieve improved optical properties. Having a bandgap is another advantage of using  $\text{MoS}_2$  (graphene does not have a bandgap).

Many experiments have been conducted to obtain the characteristics of the dielectric properties of  $\text{MoS}_2$  and analyse the optical responses of  $\text{MoS}_2$  layers at IR and the visible wavelengths. These experiments show that, the complex permittivity of  $\text{MoS}_2$  can be modelled by a Lorentz-Drude model [32, 70, 71] and obtained from the following

equation [32]:

$$\epsilon(\omega) = \epsilon' + i\epsilon'' = \epsilon_b - \frac{\omega_p^2}{\omega^2 + i\gamma\omega}, \quad (4.8)$$

where,  $\epsilon_b$  is the surrounding permittivity,  $\omega_p$  is the plasma frequency,  $\gamma$  is the electron decay rate of the material and  $\omega$  is the operating angular frequency. The plasma frequency can be calculated by  $\omega_p = \sqrt{Ne^2/(\epsilon_0 m_e^*)}$  and  $\gamma$  is calculated from  $\gamma = 1/\tau = ne^2/(\sigma m_e^*)$ , where,  $\tau$  is the scattering time of an electron,  $\sigma$  is the conductivity of the material which depends on the doping level of the material and  $m_e^*$  is the effective mass of the carriers.

### 4.1.3 Other potential materials

Silver and gold are the most frequently used materials for making nano-resonators of spaser designs owing to their plasmonic properties. Although the most frequently used geometry is the sphere, shapes, such as rods, shells, and rectangular prisms can also be used in spaser designs. In addition to two-dimensional materials such as graphene and MoS<sub>2</sub>, the design can be made of two-dimensional generic material such as plasmene, an artificial graphene analogue from plasmonic nanoparticles [56]. Black Phosphorus is also a potential plasmonic material [57,58,72–75]. Therefore, this study can be extended to Black Phosphorus based nano-resonators to improve performance. Unlike graphene, Black Phosphorus consist of a band gap and has more potential plasmonic applications than spasers.

## 4.2 Equations of a circular spaser

A circular resonator has different characteristics than other shapes such as square and rectangular resonators in terms of the resonant frequency, SP mode energy and electric field amplitude (explained in Section 4.2.1). Due to their shape, circular resonators provide higher mode confinement at the middle of the resonator and higher electric field amplitude than widely studied square resonators. A circular resonator with a finite radius supports a set of localised plasmon modes and can be derived with the eigenmode (equation 2.2) and Bergman's Spectral Index (equation 2.3) described in Section 2.3. Con-

sidering the resonator surface and the surrounding, for both the values of characteristic function  $\Theta(r)$ , the equation (2.2) simplifies to  $\nabla^2 E_k(r) = 0$ , which is the Laplacian [76]. For cylindrical coordinates, the Laplacian becomes:

$$\frac{1}{\rho} \frac{\partial}{\partial \rho} \left( \rho \frac{\partial E_k}{\partial \rho} \right) + \frac{1}{\rho^2} \frac{\partial^2 E_k}{\partial \phi^2} + \frac{\partial^2 E_k}{\partial z^2} = 0. \quad (4.9)$$

Given the appropriate boundary conditions for a circular resonator with a finite radius, plasmon modes of the resonator can be obtained if the electrical field have the following form in a cylindrical coordinate system:

$$\mathbf{E}_k = \begin{pmatrix} E_{z^+} \\ E_{\rho^+} \\ E_{\phi^+} \\ E_{z^-} \\ E_{\rho^-} \\ E_{\phi^-} \end{pmatrix} = \begin{cases} \begin{pmatrix} E_{np} J_n(k_\rho \rho) \cos(n\phi) e^{-k_z z}, \\ -\frac{k_z}{k_\rho^2} E_{np} \frac{\partial}{\partial \rho} [J_n(k_\rho \rho)] \cos(n\phi) e^{-k_z z}, \\ \frac{nk_z}{k_\rho^2} E_{np} J_n(k_\rho \rho) \cos(n\phi) e^{-k_z z}, \end{pmatrix} & z \geq 0 \\ \begin{pmatrix} E_{np} J_n(k_\rho \rho) \cos(n\phi) e^{k_z z}, \\ \frac{k_z}{k_\rho^2} E_{np} \frac{\partial}{\partial \rho} [J_n(k_\rho \rho)] \cos(n\phi) e^{k_z z}, \\ -\frac{nk_z}{k_\rho^2} E_{np} J_n(k_\rho \rho) \cos(n\phi) e^{k_z z}. \end{pmatrix} & z < 0 \end{cases} \quad (4.10)$$

where each mode is characterized by two letters  $(n, p \in \mathbb{Z}^+)$ .  $E_{np}$  is the amplitude of the electric field towards the  $z$ -direction,  $k_z$  is the wave vector towards the  $z$ -direction, and  $J_n$  is the  $n^{\text{th}}$  order Bessel function of the first kind.

Researchers have recently found that edge modes appear when the width of a graphene sheet is relatively small compared to its length (e.g. nanoribbons) but not in geometries such as circles and squares as clearly described in [77–79]. In addition, the radial component of the electric field is negligible compared to other components (described below) and it does not excite significant electric fields at the edges of the graphene flake due to reflections at the boundary. Therefore, edge modes in the circular graphene sheet can be discarded safely. Since,  $E_k$  vanishes at the edge of the circle, by applying appropriate boundary conditions,  $k_\rho = \chi_{np}/R$ , where  $\chi_{np}$  is the  $p^{\text{th}}$  solution of  $J_n(\chi_{np}) = 0$  is obtained, where  $R$  is the radius of the circular flake.

By considering realistic parameters, the values of  $k_\rho^2$  in equation (4.10) are in the range of  $10^{14} - 10^{15}$  and the values of  $k_z$  are estimated to be in the range of  $10^6 - 10^9 \text{ m}^{-1}$ , depending on the operating wavelength of the device. Therefore, the magnitude of the radial component of the electric field ( $E_\rho$ ) is relatively small compared to other components. Moreover, due to the azimuthal symmetry of the design and the deployment of the cylindrical coordinate system, the  $E_\phi$  component vanishes. Thus for greater insight and clarity, only the  $E_z$  component of the electric field can be considered as an approximate representation of the electric field in the device.

The quantised plasmonic field can be obtained by considering plasmon creation ( $\hat{a}_k^\dagger$ ) and annihilation ( $\hat{a}_k$ ) operators of the dipole SPs described in Section 3.2. Thus, the electric field operator can be defined as:

$$\hat{E} = \sum_k E_k (\hat{a}_k^\dagger + \hat{a}_k) . \quad (4.11)$$

Using the Brillouin expression for the mean field energy in a dispersive medium [19] and the form of electric field defined in equation (4.10), the unknown electric field amplitude  $E_{np}$  of the  $np^{\text{th}}$  plasmonic mode was determined as,

$$\frac{\hbar\omega_{\text{sp}}}{2} = \frac{1}{8\pi} \int_v \frac{\partial \text{Re}[\omega\epsilon(\omega)]}{\partial \omega} \Big|_{\omega_{\text{sp}}} |\mathbf{E}_k|^2 dV , \quad (4.12)$$

which yields,

$$E_{np} = \left( \frac{4\hbar\omega_{\text{sp}}k_z}{\frac{\partial \text{Re}(\omega\epsilon(\omega))}{\partial \omega} \Big|_{\omega_{\text{sp}}} \int_0^R \rho J_n\left(\frac{\chi_{np}\rho}{R}\right) d\rho} \right)^{1/2} \quad (4.13)$$

where

$$\int_0^R \rho J_n\left(\frac{\chi_{np}\rho}{R}\right) d\rho = \begin{cases} \frac{R^2}{2} [J_0(\chi_{np})^2 + J_1(\chi_{np})^2], & n = 0 \\ \frac{R^2}{2\chi_{np}} [\chi_{np} J_{(n-1)}(\chi_{np})^2 - & \\ 2n J_{(n-1)}(\chi_{np}) J_n(\chi_{np}) + & n \geq 1 \\ \chi_{np} J_n(\chi_{np})^2] . & \end{cases} \quad (4.14)$$

$R$  is the radius of the resonator and  $\chi_{np}$  is the  $p^{\text{th}}$  root of the  $n^{\text{th}}$  Bessel function of the first kind.

#### 4.2.1 Comparison of square and circular graphene flakes

This study focuses on circular resonator based designs. In addition to the commonly studied spherical design, the most commonly considered two-dimensional design is the square shape. In this study, circular geometry was chosen to obtain an analytical model for analysing the performances of the design. The two-dimensional spasers can be made of any shape in addition to a square or circle. However, due to fabrication constraints, some of the complex shapes are not applicable to spaser designs. An analysis was conducted to compare the electric field output and mode energy variation of two types of graphene spasers (square and circular) with different conditions for the fundamental modes of the resonators.

Following the same steps used for the circular resonator and considering appropriate boundary conditions for the square resonator, the electric field distribution ( $E_s$ ) of the square resonator can be expressed as,

$$E_s = \begin{cases} E_{mn} \sin(m\pi x/L) \sin(n\pi y/L) e^{-k_z z}, & z \geq 0 \\ E_{mn} \sin(m\pi x/L) \sin(n\pi y/L) e^{k_z z}, & z < 0 \end{cases} \quad (4.15)$$

where  $L$  is the side length of the graphene flake,  $m$  and  $n$  are positive integers, and  $x$  and  $y$  vary from  $-L/2$  to  $L/2$ . Using equations 4.12 and 4.15, the unknown amplitude  $E_{mn}$

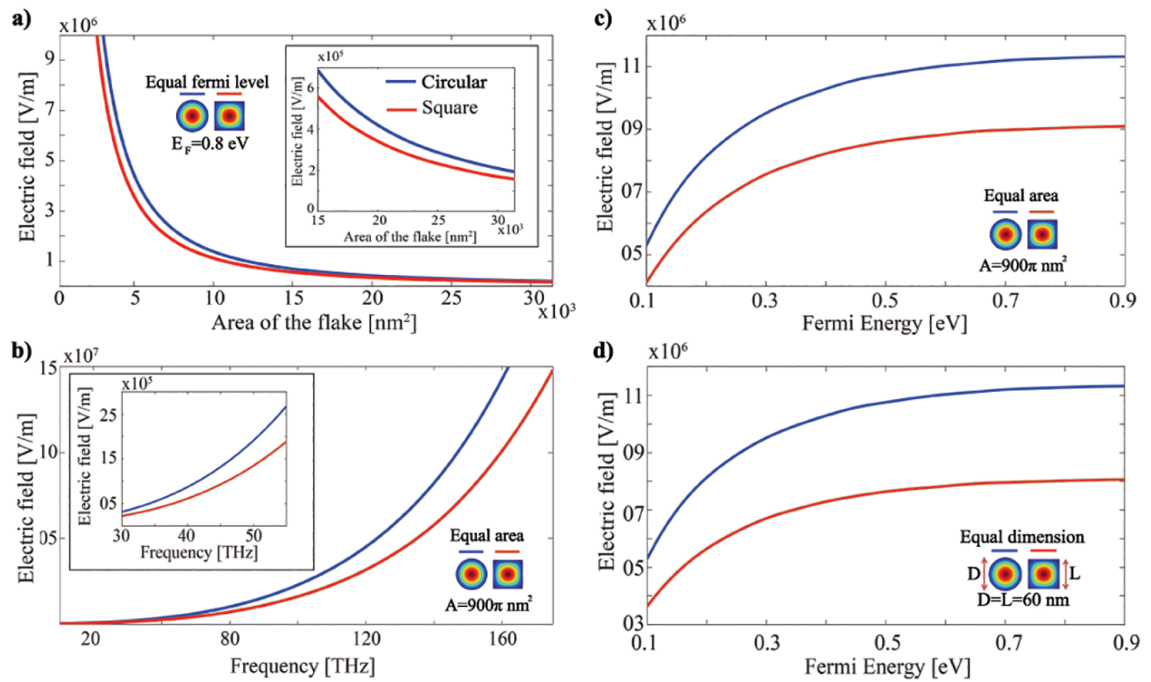


Figure 4.7: Analysis of variation of output electric field intensity of the circular spaser (blue) and square spaser (red) geometries: a) Variation of the electric field intensity with area of the flake for fermi energy 0.8 eV. b) and c) Electric field intensity with the variation of spaser mode frequency from Mid-IR to Near-IR and fermi energy of the flakes from 0.1 eV to 0.9 eV respectively for circular resonator of 30 nm radius (R) and square resonator with side length (L) of  $30\sqrt{\pi} \text{ nm}$  ( $A = 900\pi \text{ nm}^2$ ). d) Electric field intensity distribution for varying fermi energy from 0.1 eV to 0.9 eV for resonators with diameter (D) and side length (L) of 60 nm.

of equation (4.15) can be derived as,

$$E_{mn} = \left( \frac{16\pi\hbar\omega_{sp}k_z}{L^2 \left. \frac{\partial \text{Re}[\omega\epsilon(\omega)]}{\partial \omega} \right|_{\omega_{sp}}} \right)^{1/2} \quad (4.16)$$

The SP mode wavelength of a resonator is dependent on geometry and size of the resonator [22]. The mode frequencies of both resonators were determined by the COMSOL Multiphysics Eigenmode Solver (see Appendix A for the results).

Figure 4.7 a) illustrates the electric field distribution of the fundamental mode of the resonators which are presented in equations (4.13) and (4.16) with the variation in the area of the flakes, while maintaining the Fermi energy of the flakes at 0.8 eV. For both resonators, the output electric field intensity decreases when the area increases. For areas that are considered, the electric field amplitude of the circular resonator (blue color line) is higher than the square resonator.

Another important factor that must be considered when designing nano-circuitries is the packing density of the proposed device. The device should provide more efficient outputs with smaller dimensions. Figure 4.7 shows an analysis of the electric field distribution of the resonators. Figure 4.7 b) shows the variation of electric field distribution with mode frequency. Here, equal area scenario ( $A = 900\pi \text{ nm}^2$ ) for a circular flake with a 30 nm radius and a square flake with a side length of  $30\sqrt{\pi}$  nm was analysed for mode frequencies varying from the Mid-IR range to the Near-IR range. Electric field amplitude increases exponentially with the spaser mode frequency. Variation of the electric field distribution of both the resonators for varying fermi energy from 0.1 eV to 0.9 eV, and for equal area and equal dimension scenarios is shown in Figure 4.7 c) and Figure 4.7 d). In Figure 4.7 d), a circular resonator with a 60nm diameter (D) was selected for comparison with a square resonator that has a side length (L) of 60 nm. For both cases, electric field increases when Fermi energy increases and the rate of electric field amplitude decreases when fermi energy increases. For all four cases, the circular resonator provides more

electric field intensity than the square resonator.

The results of the simulations demonstrate that the circular resonator supports higher mode energies than the square resonator with similar dimensions. Therefore, the circular resonator provides higher electric fields as shown in the Figure 4.7. Higher energy density in the middle of the circular resonator [5,80] is also a reason for the higher outputs. In addition to electric field amplitude, other resonator characteristics, such as plasmon generation rate and number of SPs generated per spasing mode primarily depend on the SP mode energy. Therefore, the design which provides higher SP mode energy provides higher output in all the aspects. Moreover, for both of the flakes, the mode energy decays when the size of the flakes increases. Since the circular graphene resonator provides more energy and higher electric field intensity, it is useful for designing ultrafast nanocircuits.



# Chapter 5

## Graphene based spasers

**H**IGH-speed, ultra-thin nanodevices are integral to the development of miniaturized electronic devices [1–3]. Due to many advances in micro fabrication technology throughout the past two decades, it is now possible to fabricate ultra-thin structures that operate in the quantum regime [2, 3]. Since the operating wavelengths of these devices are much higher than their physical dimensions, they must work in the plasmonic regime to overcome limitations imposed by diffraction artefacts [2, 3, 81, 82]. A spaser is an ideal concept for overcoming those issues mentioned. In this chapter, in contrast to widely analysed quadrilateral resonators, details of two-dimensional, circular, resonator based spasers are analysed and described. This chapter also proves that the proposed geometry provides higher outputs compared to square and rectangular shapes, providing adequate results based on simulation and analytical studies. This chapter also provides details, such as continuous wave (CW) and dynamic responses of spaser designs based on mono-layer and bi-layer circular graphene resonators.

### 5.1 Circular graphene spaser

After the experimental discovery of two-dimensional gated graphene in 2004 by Novoselov *et al.* [83–87], miniaturised opto-electronic designs took a revolutionary step towards realising efficient, strong, ultra-fast designs due to the surprising optical properties of graphene described in Section 4.1.1. The use of graphene in spaser designs creates opportunities to design ultra-thin, ultra-fast, nano-scale opto-electronic circuits. This section describes an electrically pumped, quantum cascade well powered spaser made of

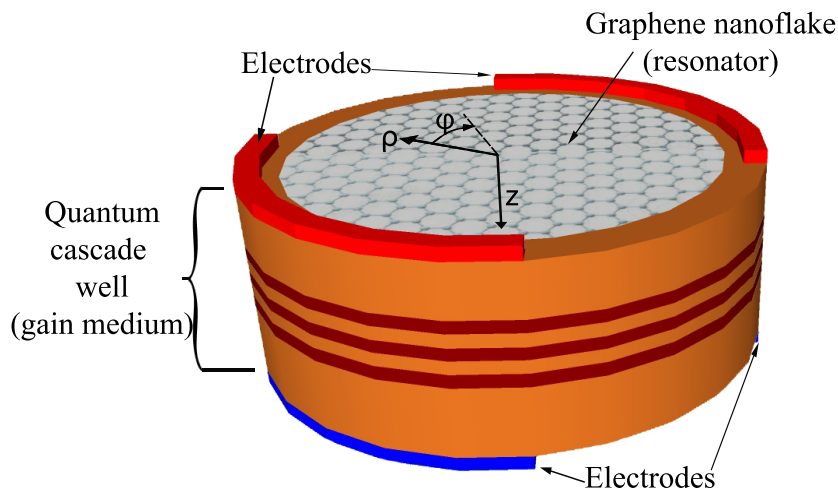


Figure 5.1: Schematic diagram proposed circular spaser made with a circular graphene patch resonator that has an electrically pumped, quantum cascade well gain medium.

circular shaped doped mono-layer graphene (MLG).

## 5.1.1 Spaser Model

### 5.1.1.1 Design

The design that was adopted for the circular graphene spaser in this study is shown in Figure 5.1. The design consists of a circular graphene nanopatch resonator which supports a set of plasmon modes powered by a quantum cascade well (active medium) [88–90]. The electrodes were included to pump energy to the gain medium and a circular graphene patch was selected for the properties, such as ease of fabrication and to obtain analytical expressions for comparing the design with simulation results. The nanofabrication of such graphene disks have been demonstrated experimentally [91], which allows the number of geometric parameters to be reduced without loss of generality. For a given radius,  $R$ , the resonator supports a number of localised surface plasmon (SP) modes with different wavelengths as shown in Figure 5.2. Those modes spatially and spectrally overlap with the intersubband transitions of the active element and experience different amounts of gain. The SP mode, which is in resonance with intersubband transitions of the gain medium, receives the maximum gain and becomes the dominant mode of the

spacing field.

Consequently, transitions between the subbands of the active medium generate coherent plasmons in the circular graphene sheet since the stimulated emission occurs in the resonator. The coherence of the produced plasmons is an imperative characteristic of the device. The required degree of coherence depends on the application; optoelectronic applications typically require higher spatial and temporal coherence [92]. Furthermore coherence properties of light confined in subwavelength structures can be found in the literature [93, 94]. This analysis there can be readily extended to the current scenario, demonstrating that both temporal and spatial coherence of the field can be maintained provided stimulated emission occurs inside the cavity. The graphene structure positively contribute to sustain coherence attributes in the cavity as discussed in references [34, 95].

The wavelength of the generated plasmons depends on the emission wavelength of the intersubband transitions of the active medium. To obtain a specific mode with corresponding wavelength, it is necessary to change the flake radius, the Fermi level of the flake and the wavelength of the transitions of the gain medium. The tunability of the proposed design is discussed below.

### 5.1.1.2 Spaser modes and degeneracy

A circular graphene flake with a finite radius of 30 nm - 100 nm accommodates coherent, localized plasmon modes due to the properties of graphene [33, 34]. The plasmonic properties of graphene are based on its wavelength and dependent on optical conductivity, which can be varied widely at infrared wavelengths (0.75  $\mu\text{m}$  - 10  $\mu\text{m}$ ). It derives its properties from both intraband and interband contributions. Furthermore, the wavelength dependent, complex permittivity of MLG can be obtained from equations 4.5 and 4.6. Modes of the resonator also can be found using the SP eigenvalue equation (equation 2.2).

Considering appropriate boundary conditions for a finite circular graphene sheet

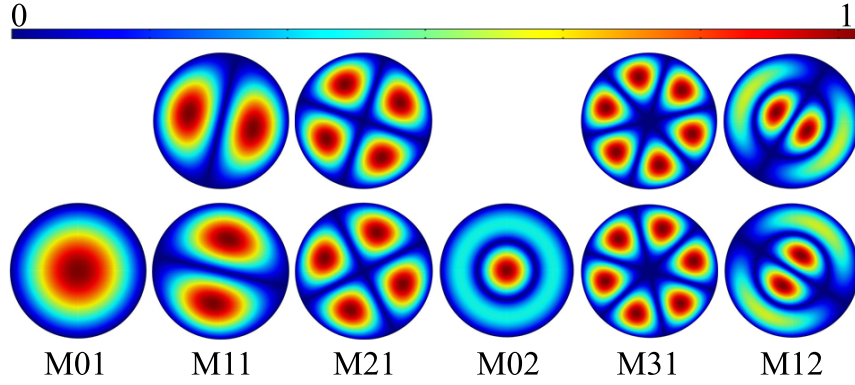


Figure 5.2: Normalized electric field distribution of the six lowest energy modes supported by the circular graphene flake.

with a thickness of 0.46 nm, (derivations provided in the Section 4.2), localised plasmon modes can be derived by assuming that the electrical field has the following form in a cylindrical coordinate system:

$$\mathbf{E}_k = \begin{pmatrix} E_{z^+} \\ \\ E_{z^-} \end{pmatrix} = \begin{cases} E_{np} J_n(k_\rho \rho) \cos(n\phi) e^{-k_z z}, \\ \\ E_{np} J_n(k_\rho \rho) \cos(n\phi) e^{k_z z}, \end{cases} \quad (5.1)$$

where each mode is characterized by two letters  $(n, p \in \mathbb{Z}^+)$ .  $E_{np}$  is the amplitude of the electric field towards the z-direction,  $k_z$  is the wave vector towards the z-direction and  $J_n$  is the  $n^{\text{th}}$  order Bessel function of the first kind.

The normalized electric field distribution of the modes is obtained from equation (5.1) and corresponding SP resonance wavelengths are found numerically with the use of three-dimensional conductivity of the graphene sheet. The localised SP mode frequency which is supported by a resonator is dependent on the shape and size of the resonator [22].

Since graphene plasmons affect strong inherent, coherent plasmonic wave localisation and extreme light confinement [34], the circular graphene nano resonator supports a series of localised plasmon modes as shown in Figure 5.2. These modes can be excited

from an external source as described in following sections of this chapter. Since the generated plasmon modes are localised plasmon modes, they can be characterized in similar manner to dielectric disk resonator modes [22,96]. Figure 5.2 shows the normalized electric fields of the six lowest energy modes supported by a circular MLG nanoflake with 30 nm radius. The letter "M" represents the word mode, the first letter represents value of  $n$ , and second letter represent the value of  $p$ . Figure 5.2 demonstrates that, due to the symmetry of the flake, M11, M21, M31, and M12 are twice as degenerated, while carrying the same mode energy [21,24].

### 5.1.1.3 Quantum cascade well

The emission wavelength of the quantum cascade well is essentially determined by quantum confinement, which depends on the thickness of the material and independent of their band gap [81,97–103]. Based on the latter property, the emission wavelength can be tuned over a wide range using the same material with different thicknesses. Moreover, the thermal stability of the quantum well structure provides a tremendous advantage for the design and operation [81,89].

Figure 5.3(a) shows the energy profile of the conduction band of the quantum cascade well and it is made of low-bandgap material (GaInAs) inserted between layers of a higher-bandgap semiconductor (AlInAs) [88]. The horizontal lines indicate the lowest energy subbands and the location of the energy level depends on the thickness of the well. When the thickness of the hetero-structures is reduced to a nanometre scale, quantum effects arise in the structure and separating the subbands. When the thickness is reduced, the subband energy separation increased and this process is called bandgap tailoring [104–108]. However, due to fabrication and operational constraints, a quantum cascade well can provide emissions in the range of IR wavelengths. In the active region of the quantum cascade well, electrons can undergo cascaded energy levels by emitting energy to the circular graphene nanoflake resonator. The schematic diagram of the intersubband transitions of quantum well is shown in Figure 5.3(b). The emission occurs between quantised energy level for electrons  $E_1$  and  $E_2$  or for holes  $H_1$  and  $H_2$ . These

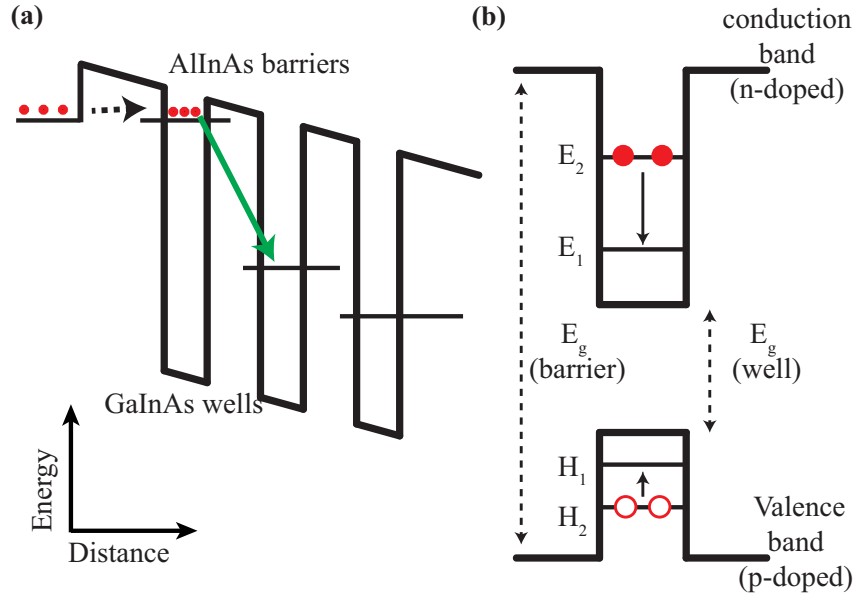


Figure 5.3: **(a)** Schematic diagram of the conduction band energy profile of the quantum cascade well. **(b)** Schema of a quantum well and the intersubband transition between lowest energy levels of electrons,  $E_1$  and  $E_2$ , or for holes  $H_1$  and  $H_2$  in the well.

quantized energy levels can be changed by adjusting the thickness of the well through altering the deposition time of the material [81, 89, 109]. The energy levels of an electron can be determined using the following equation,

$$E_n = \left( \frac{\hbar^2 \pi^2}{2m^* L_w^2} \right) n^2, \quad (5.2)$$

where  $L_w$  is the thickness of the layer,  $n$  is an integer corresponding to the energy level and  $m^*$  is the effective mass of electrons in the well. Then the energy difference ( $E_{21}$ ) between the lowest ( $E_1$ ) and the first excited states ( $E_2$ ) of the intersubband transition can be obtained as,

$$E_{21} = E_2 - E_1 = \frac{3\hbar^2 \pi^2}{2m^* L_w^2}. \quad (5.3)$$

With realistic parameters,  $\text{Ga}_{0.47}\text{In}_{0.53}\text{As}$  has an effective bandgap of 0.75 eV and  $m^* = 0.041m_0$ , where  $m_0 = 9.1 \times 10^{-31}$  kg is the mass of an electron [110]. The active medium of the design is treated quantum-mechanically and SPs are treated quasi-classically. Considering the quantum mechanical model of the spaser, when the system has a stationary

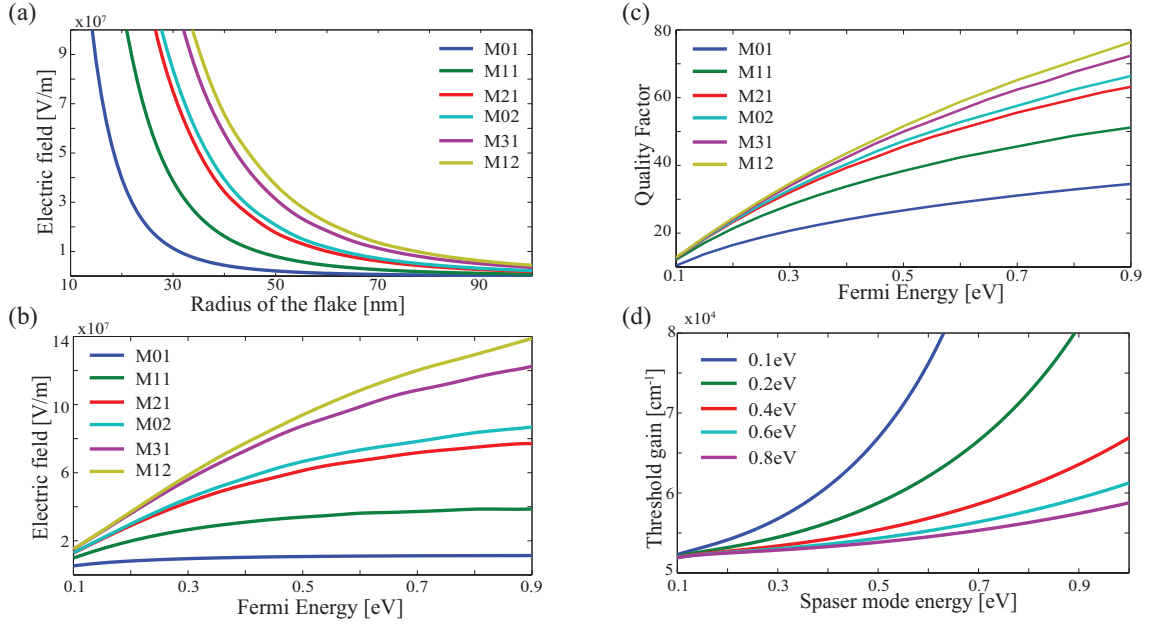


Figure 5.4: Tunability and operating characteristics of circular graphene spaser: Electric field intensity distribution of six lowest energy modes supported by circular flake against (a) radius of the flake with Fermi energy of 0.8 eV, (b) Fermi energy of the flake for a flake of 30 nm radius, (c) plasmon quality factor distribution over the Fermi energy of the flake from 0.1 eV to 0.9 eV, (d) threshold gain required for continuous spasing for the spaser mode energies from 0.1 eV to 1.0 eV.

number of SPs per spasing mode (continuous wave (CW) regime), the necessary condition for spasing can be found using the method described in Section 3.3

## 5.1.2 Results and Discussion

### 5.1.2.1 Analytical model

The circular spaser models described in Chapter 3 and Chapter 4 are used to analyse and derive the corresponding operational characteristics of the proposed design.

### 5.1.2.2 Operational characteristics and their tunability

The circular graphene flake supports a set of SP modes with different frequencies as defined in equation (5.1). The normalized electric field distribution and the first six spaser

modes supported by the circular graphene flake are presented in Figure 5.2. For a specific radius of the flake, the nano-resonator supports a series of spaser modes as described in Section 6.2.2. There is an associated frequency for each mode. Based on these mode frequencies which are found numerically, and equation 5.1, the tunability of the modes electric field intensity supported by the flake is shown in Figure 5.4(a) as a function of the flake radius ( $R$ ). For a given radius of the flake, it is possible to obtain different electric field amplitudes by changing the gain of the system. This gain depends only on the dielectric properties of the system and spasing wavelength, and not on the geometry of the system or the distribution of the local fields of the spasing mode [21]. Since the permittivity of graphene can be altered by changing the Fermi level of the flake, the electric field of the proposed device can be tuned according to the requirement shown in Figure 5.4(b). Figure 5.4(b) illustrates electric field intensity distribution with the Fermi energy of the flake. The spaser mode energies are seen to vary over a wide range from Mid-IR to Near-IR permitting flexibility in spaser design. These variations can be tailored over a wide range by varying spaser geometry such as the size, shape, and material parameters of the flake [22,24,91].

In a conventional, non-diffraction limited setup, optical resonances can occur by periodic exchange of energy between electrical and magnetic fields [111, 112]. However, when a cavity is formed for sub-diffraction operation (*e.g.* to make a spaser), the ability of the magnetic field to store the full amount of energy contained in the electric field fails, disrupting its ability to self-sustain a resonance condition [113,114]. The remedy is to use kinetic energy on free electrons interacting with the field, restoring the energy balance for self-sustained oscillations. Spasers take advantage of this mechanism, but the kinetic energy is lost from the system commensurate with the rate of electrons scattering in metal [114–116]. The solution is to introduce gain either using optical or electrical pumping to restore the energy loss through electron scattering [6, 117, 118]. Another approach is to design materials with less loss (*i.e.* low electron scattering rates) and high free carrier densities [119]. Both methods are feasible because none of the fundamental physical laws provide tight constraints on these processes. A radically different approach is to consider

A cluster of strongly coupled spasers making up a system that collectively suppresses the Purcell effect and reduces the threshold gain requirements [120]. The design in this study avoids some of the issues associated with three-dimensional, conventional metals by using two-dimensional graphene with that can sustain plasmon resonances with a higher quality factor (Q) compared to metallic cavities and stronger field confinement. As a result, the losses associated with the proposed spaser design can be compensated using the quantum cascade well structure described here. The condition for continuous spasing depends on the Q factor of the generated plasmons which can be estimated by [21]

$$Q = \frac{\omega}{2} \frac{\partial \text{Re}[\epsilon(\omega)] / \partial \omega}{\text{Im}[\epsilon(\omega)]}. \quad (5.4)$$

Figure 5.4(c) shows the impact of the Fermi energy for the quality factor of the plasmons generated by the flake. Doping would improve the quality factor of the plasmons generated by the circular graphene resonator, which provides improved spaser performances with lower losses.

It is important to analyse amount of threshold gain ( $g_{\text{th}}$ ) required for continuous operation of the spaser. The threshold gain depends on the spaser mode wavelength and flake properties, which are functions of spaser geometry and material parameters. The amount of gain required for spasing is [21],

$$g_{\text{th}} = \frac{\omega}{c\sqrt{\epsilon_d}} \frac{\text{Re}[s(\omega)]}{1 - \text{Re}[s(\omega)]} \text{Im}[\epsilon(\omega)] \quad (5.5)$$

The threshold gain has a unit of " $\text{cm}^{-1}$ ". The amount of threshold gain required to increase spaser mode energy from 0.1 eV to 1.0 eV for different Fermi levels is illustrated in Figure 5.4(d). There is exponential growth in the required gain with increasing spaser mode energy. For lower Fermi energy values the proposed spaser requires higher threshold gain than for higher Fermi energies. Moreover, the device should satisfy the necessary condition given in equation 3.13 for spasing in CW regime. The corresponding Rabi

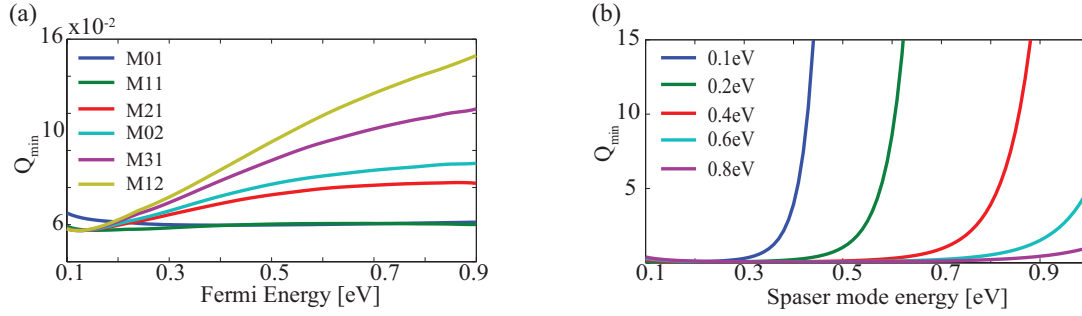


Figure 5.5: Minimum quality factor required for spasing against (a) Fermi energy of the graphene flake and (b) spaser mode energy.

frequency is presented in reference [19]:,

$$\Omega_{12} = E_{np}d_{12}e^{-k_z\ell}, \quad (5.6)$$

where  $d_{12}$  is the intersubband envelop dipole matrix element and must be a real quantity. This element can be made real by taking proper design considerations.  $\ell$  is the characteristic distance between the graphene layer and the quantum well. According to reference [19], for the cascade well structure  $\Sigma_k|\Omega_{12}|^2$  reduces to,

$$\Sigma_k|\Omega_{12}|^2 = \frac{\hbar\omega_{sp}qk_0^2}{\epsilon_0\epsilon_r}|d_{12}|^2e^{-2k_z\ell}, \quad (5.7)$$

where  $q$  is the plasmon wave vector that can be calculated from the following equation [34],

$$q(\omega) = 2\pi\hbar^2\epsilon_0\epsilon_r\omega(\omega + i\tau^{-1})/(e_0^2E_F), \quad (5.8)$$

where,  $e_0$  is the charge of an electron and  $k_0$  is an effective Fermi wave vector of the quantum cascade well structure. Since  $\omega_{12} = \omega_{sp}$  at the resonance, the condition for spasing in equation 3.13 simplifies to,

$$\frac{2\pi\hbar^3\omega_{sp}^2(\omega + i\tau^{-1})k_0^2}{e_0^2E_F}|d_{12}|^2e^{-2k_z\ell} \geq \gamma\Gamma_{12}. \quad (5.9)$$

Equation (5.9) introduces a condition of the plasmon polarization relaxation rate. Since,  $Q = \omega_{sp}/(2\gamma)$  a condition of  $Q$  for spasing can be derived as follows:

$$Q \geq Q_{\min} = \frac{e_0^2 E_F \Gamma_{12}}{4\pi \hbar^2 \omega_{\text{sp}} (\omega_{\text{sp}} + i\tau^{-1}) k_0^2 |d_{12}|^2} e^{2k_z \ell}. \quad (5.10)$$

The realistic parameters of the gain medium are  $d_{12} = 2.5e_0$  nm,  $\ell \simeq 6.5$  nm and  $k_0 = 0.1$  nm<sup>-1</sup> [19]. For the quantum wells, there will be inhomogeneous broadening of intersubband transitions due to fluctuations in the well thickness and interface roughness. Thus,  $\Gamma_{12} = 3.6$  meV [19] was used for the structure. Figure 5.5(a) illustrates the minimum quality factor required for spasing in the CW regime for the condition derived in equation (5.10) for Fermi energy variation from 0.1 eV to 0.9 eV. After 0.15 eV, the required  $Q_{\min}$  increases when  $E_F$  increases. The required  $Q_{\min}$  is less than 0.2 For the entire span, which is well below the Q value of the generated plasmons. Furthermore, the  $Q_{\min}$  required for CW spasing of the corresponding mode energies from 0.1 eV to 1.0 eV for different Fermi levels are shown in Figure 5.5(b). There is an exponential variation of the  $Q_{\min}$  versus the SP mode energy and, for less Fermi energies, such as 0.1 eV, the system requires higher  $Q_{\min}$  threshold than for higher Fermi energy values at higher mode energies. Since the Q values of the device stay above ten for low Fermi energies (Figure 5.4(b)), at low Fermi energies such as 0.1 eV, the device can operate in the Mid-IR range For high Fermi energies greater than 0.6 eV, it is possible to operate within the Near-IR range.

The analysis of spaser characteristics determined that the proposed spaser is highly tunable and can be optimized to achieve more efficient output with more energy. The fundamental mode energy can be altered from 0.1 eV to 0.7 eV and other modes can provide more energy while producing electric field intensity of up to  $35 \times 10^7$  V/m for a flake with a 20 nm radius and an  $E_F = 0.8$  eV. The spaser mode frequencies can be tailored over a wide range from Mid-IR to Near-IR by changing the radius ( $R$ ) and Fermi energy ( $E_F$ ) of the flake. The active medium can be set to particular emission wavelength by changing the thickness of the sandwiched layers of GaInAs and AlInAs without changing the materials, as with conventional lasers. The thickness of the layers can be changed according to equation (5.2) by varying the deposition time of the materials. These structures are thermally stable compared to other active mediums [89, 90]. Furthermore, this design supports SPs that have higher quality factors than noble metals such as gold and

silver, which reduces loss. Due to higher mode confinement in the center of the resonator because of its circular-shape [80, 121], the design provides higher spaser mode energies and electric field intensities in a compact setup compared to previously reported designs. In addition, the circular graphene spaser satisfies the necessary conditions for spasing in the CW regime. The major tuning parameters of the spaser provide flexibility of design by considering fabrication methods.

Using common techniques of nanofabrication, the proposed graphene circular spaser can be experimentally constructed. Nanofabrication of graphene disks (with a minimum radius of 20 nm) and quantum cascade well structures that supports Mid-IR to Near-IR frequencies have been experimentally demonstrated [89, 91]. In addition to tunability and ease of fabrication, the proposed design has additional advantages such as mechanical strength and thermal stability due to the exceptional properties of the quantum cascade well structure and graphene. Therefore, this design is useful as an active device when designing ultrafast nanocircuits. Moreover, it can be used in on-chip circuits because the spaser is powered electrically using electrodes unlike those that are optically powered with bulk lasers. Therefore, possible applications of the circular graphene spaser range include ultrafast nanodevices, on-chip circuits, and high-temperature tunable electronic devices.

### 5.1.3 Conclusion

In this chapter, a circular spaser made of a graphene resonator and powered by a quantum cascade well is proposed and discussed. The operational characteristics and tunability of the device are demonstrated. Performance can be improved *by* controlling the dielectric properties, size of the flake, and adjusting the emission wavelength of the quantum cascade well structure by changing the thickness of the heterostructures. The design supports a series of modes with different mode energies. Due to the shape of the resonator, the device supports SP energy modes with degenerated modes of same energy and can be tuned over a wide frequency range from Mid-IR to Near-IR. The proposed electrically pumped circular graphene spaser can be fabricated using current nanofabrication meth-

ods. The circular graphene resonator allows, the proposed design to delivers a higher quality factor, high electric field intensities, and corresponding higher spaser mode energies in a compact setup compared to previously reported designs. In addition, mechanical and thermal stability are other advantages of the device. This design is an efficient source for intense, coherent optical fields, and because of the size and operating speed of the device, it has numerous potential applications including nanoscopy [122,123], high speed nano-processors [124] and nano-optoelectronics [125].

## 5.2 Ultra-fast dynamics of graphene spasers

The previous section provided the operational characteristics of an MLG based spaser working in the steady state mode (CW operation). A graphene spaser can be used in the CW mode and as an amplifier or a modulator. The following sections describe the ultra-fast behaviour of a spaser based on MLG. The effect of changes in the gain system to the plasmonic nano-resonator is also considered in this analysis. Since the device is powered by optically pumped quantum dots, the spaser is an optically pumped configuration.

### Device Setup

This work considers, both the continuous wave and dynamic responses of an MLG based spaser. A schematic diagram of the proposed spaser design considered in this work is shown in Figure 5.6. The setup consists of a circular graphene flake, quantum dots and a VCSEL. Gain is introduced to the system by embedding quantum dots inside of a dielectric material over the flake. These quantum dots are pumped optically with a VCSEL as shown in the schema. Two electrodes are provided to power the VCSEL. Due to energy conservation laws and the conditions for exciting plasmons on a surface, the interaction with the laser beam from the VCSEL with the graphene resonator [126] is assumed to be negligible. Considering the operation of the spaser, the excited atoms provide energy non-radiatively [127–129] to the resonator and generate SPs accordingly. The process starts due to the spontaneous noise of the plasmonic system [18]. Since the stimulated emission occurs, a coherent SP output can be achieved from the graphene res-

onator [93,94]. The design considerations of each component are described in following subsections.

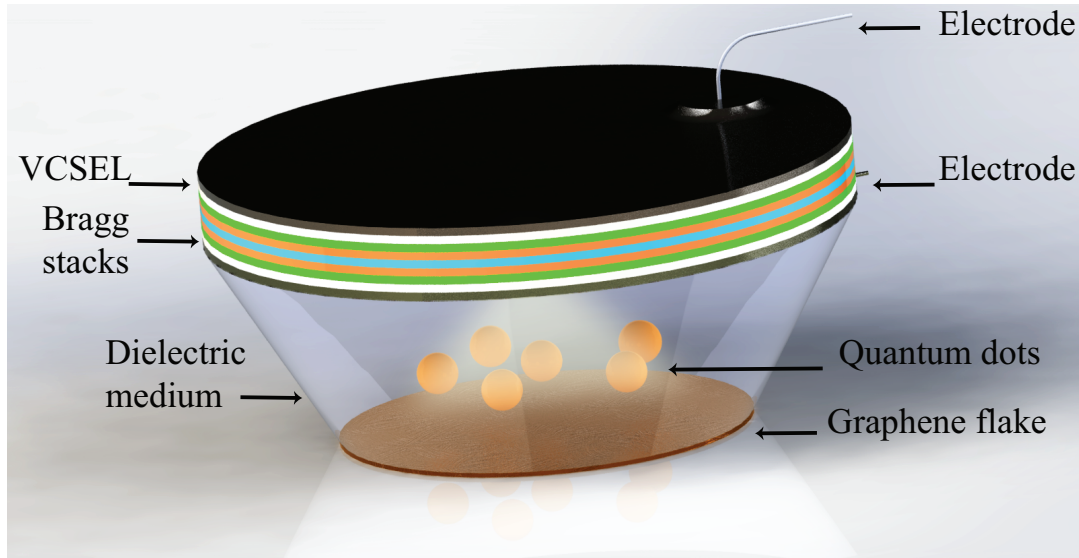


Figure 5.6: (a) Schematic of the proposed spaser based on a circular graphene flake pumped by a VCSEL.

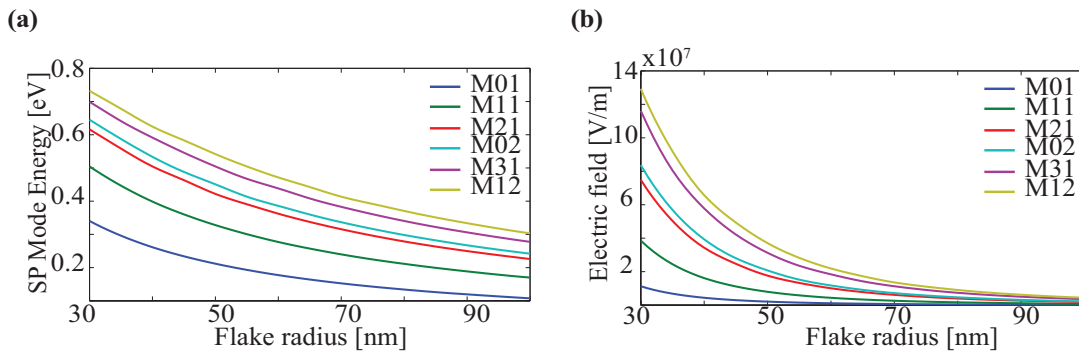


Figure 5.7: (a) Spaser mode energy variation of the six lowest energy modes with respect to the radius of the flake. (b) Electric field amplitude variations obtained in equation (4.13) according to the variation of the flake radius.

### MLG circular graphene resonator and its plasmon modes

Similar to the previous design described in the first half of this chapter, the newly proposed spaser design is also equipped with a circular shaped graphene flake. A circular geometry was chosen for the higher mode confinement in the middle of the resonator,

and for the ease of coupling it with the VCSEL and many other optical interconnections [7, 130]. Since, the shape of the resonator remained the same, this spaser supports the same set of SP modes shown in the Figure 5.2. SP mode energy variations with respect to the radius of the flake are shown in Figure 5.7 a) and the electric field amplitudes obtained from the equation (4.13) are shown in Figure 5.7 b). Both SP mode energy and electric field amplitude have an inverse relation to the radius for the radius span considered in this study. SP mode energies that vary in wavelength from Near-IR to Mid-IR ( $1.7\mu\text{m} - 10\mu\text{m}$ ) can be obtained from this device [7]. Furthermore, the resonator can achieve an electric field amplitude in the order of  $\sim 10^7 - \sim 10^8$  with maximum electric field amplitude of  $1.3 \times 10^8$  at the flake radius of 30 nm. The electric field amplitude of a spaser strongly affects the dynamic performances of the setup and is described in the spaser characteristics subsection.

### Active medium

Gain must be introduced to the system to achieve continuous operation of the spaser by overcoming the losses of the nano-resonator. When spaser is operating, the gain is equal to the losses of the resonator. In the proposed design, semiconductor quantum dots or dye molecules can be used as the active medium. and in this study, quantum dots were used. These quantum dots were embedded in a dielectric slab over the graphene flake to provide energy to produce SPs in the flake. Here, a typical value of the density of chromophores is considered as  $\rho_0 = 6.5 \times 10^{24} \text{ m}^{-3}$  which is realistic for PbS quantum dots that support IR emissions [131, 132]. However, this study can be extended to any type of gain chromophores. Graphene based quantum dots can also be considered as a potential active medium for this spaser design. If a set of quantum dots does not cover all of the operational wavelengths considered for the nano-resonator, several types of quantum dots with different sized can be used along with a matched pump. A quantum dot can be tuned to provide emissions at different wavelengths by changing its size. More details of how to tune gain mediums are provided and described in Section 7.1.

A two-level gain system is considered in this analysis and a third level is introduced

to achieve gain in the system [6,21]. However, an assumption can be made as, the third level decays rapidly in to the second level and there is no considerable population in the third level compared to second and ground levels during the operation of the spaser. Therefore, the system satisfies the equation  $E_2 - E_1 = \hbar\omega$  where,  $E_1$  and  $E_2$  represent the energy of the ground state and excited state respectively and  $\omega$  is the angular frequency of the transition.

The following realistic parameters are considered in this study to analyse the performance of the setup. The dipole matrix element corresponds to the transition from  $|2\rangle \rightarrow |1\rangle$ ,  $d_{12} = 3.1233 \times 10^{-8} e_0$ , a polarization relaxation rate of  $\Gamma_{12} = 2.42 \times 10^{12} \text{ s}^{-1}$  and a decay rate of  $\gamma_2 = 4 \times 10^{12} \text{ s}^{-1}$  [18,21].

### VCSEL pump

To achieve continuous operation, the active medium must to be pumped optically or electrically. A pump laser was used to pump the active medium optically since the active medium is quantum dots. A VCSEL was used as the pump due to the peculiar optical and geometrical properties [133–139]. VCSEL provides a circular output beam unlike other semiconductor lasers where as other semiconductor lasers typically provide elliptical optical beam due to waveguiding and scattering effects [140]). Hence, the output can be easily coupled with the circular nano-resonator with higher efficiency. To achieve less mirror loss ( $\approx 40 \text{ cm}^{-1}$ ) in the cavity, in a conventional laser, the cavity length is in the order of few hundreds of microns. However, the reflectivity of the mirrors (R) is much higher than normal lasers because of the Bragg stacks (the VCSEL is a variation of the distributed Bragg reflector or (DBR) laser) Using 20 to 30 periodic layers of high refractive indexed layer next to low refractive indexed layers, a reflectivity up to 0.998 can be achieved. Hence, the cavity length can be reduced to a few nanometres. Furthermore, in bulk, an array of VCSELs can be fabricated easily with the epitaxial growth method.

When a laser is operating, the gain ( $\gamma$ ) = scattering loss ( $\alpha_{scatter}$ ) + mirror losses ( $\alpha_{mirror}$ ). There is an inverse relationship between the length of the cavity and the mirror losses and

the length with respect to loss can be calculated with:

$$\alpha_{mirror} = \frac{1}{2l} \ln \left( \frac{1}{R_1 R_2} \right) \quad (5.11)$$

where,  $R_1$  and  $R_2$  are the reflectivity of the mirrors at the two ends and  $l$  is the length of the laser cavity. Due to the Bragg stacks of the VCSEL, reflectivity of 0.998 can be achieved. Therefore, for a loss of  $40\text{cm}^{-1}$ , the cavity length can be reduced to a few hundred nanometers ( $\approx 200\text{nm}$ ).

## Results and Discussion

In this work, as the first regime of operation, the characteristics of the spaser in the CW (steady state) mode were studied and the results obtained from equations (3.10) and (3.11) are shown in Figure 5.8. Although a spaser can start from different arbitrary initial SP populations ( $N_{sp}$ ), it comes to a stationary number of SPs in a very short time. The spaser was pumped continuously over the entire period and performance of the spaser after reaching the CW mode (in hundreds of femtoseconds) was analysed. Figure 5.8 (a) shows the number of SPs generated per each mode versus the gain of the system when the spasing mode energy was 206.78 meV ( $\omega/2\pi=50$  THz). Similarly, Figure 5.8 (b) depicts the number of SPs generated when the mode energy was 248.14 meV ( $\omega/2\pi=60$  THz). The generated SPs can reach more than 900 for the higher modes with a spasing frequency of 50 THz at a higher gain of  $12 \times 10^{12} \text{ s}^{-1}$ . However, for higher frequencies, as shown in Figure 5.8 (b), there is a noticeable deduction in the number of generated SPs. though it reaches 250 when the gain is  $12 \times 10^{12} \text{ s}^{-1}$ . In contrast to the laser, in a spaser, the SP population only reaches 1000 at 50 THz even with a higher gain of  $12 \times 10^{12} \text{ s}^{-1}$ ; lasers provide a population in the order of  $\sim 1000$ . The reason for low population was the smaller mode volume compared to the laser [18]. Figures 5.8 a) and b) imply that, just after the threshold gain, the curve has a linear relationship with the gain. The slope of the number of SPs generated per spasing mode with respect to the gain of the system declines for higher values of gain and reaches a constant, showing a horizontal asymptote.

Six different spaser designs are considered to obtain different transversal mode energies (*i.e.*  $M_{01}$ ,  $M_{12}$ , etc). In addition, Figures 5.8 (c) and (d) illustrate variation in the number of SPs generated with respect to the flake radius, from 35 nm to 95 nm (generates SPs in Mid-IR to near-IR wavelengths) for different gain values of  $5 \times 10^{12} \text{ s}^{-1}$  and  $8 \times 10^{12} \text{ s}^{-1}$  respectively. In this scenario, the electric field and the mode frequency vary according to the flake radius as shown in figure 5.8 (c) and (d). Thus, electric field affects the single plasmon Rabi frequency ( $\Omega_{12}$ ) and the number of generated plasmons increase when the radius increases, but not linearly. Due to the low SP mode energy,  $M_{01}$  provides the highest SP population and it achieves 1000 at a radius of 82 nm when the gain is  $8 \times 10^{12} \text{ s}^{-1}$ .

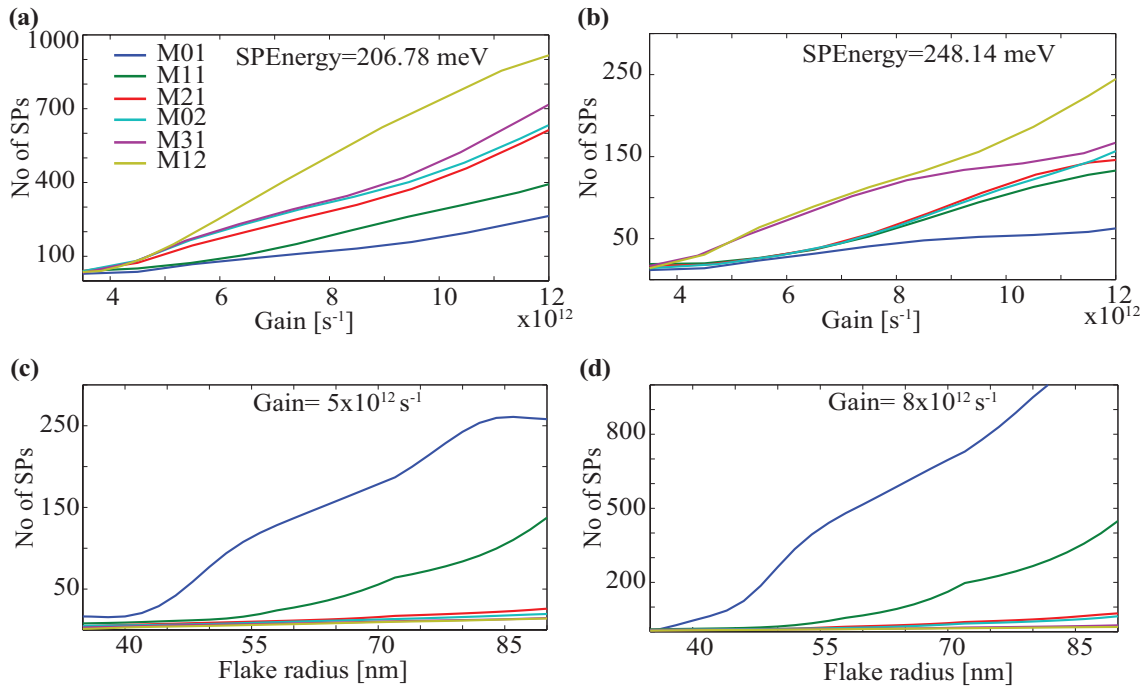


Figure 5.8: **(a)** No of SPs generated per each mode with respect to gain when the SP mode energy is 206.78 meV. **(b)** Same as **(a)** when SP mode energy is 248.14 meV. **(c)** No of SPs generated per mode Vs flake radius while providing constant gain of  $5 \times 10^{12} \text{ s}^{-1}$ . **(d)** Same as **(c)** when the gain is  $8 \times 10^{12} \text{ s}^{-1}$ .

The CW mode of operation was analysed in the time domain using the results obtained by solving equations 3.6 to 3.9. A pump with a finite gain larger than the threshold gain (in the order of  $\sim 10^{12} \text{ s}^{-1}$ ) began pumping the system at  $t = 0$ . while an arbitrary

SP population ( $N_{np}$ ) was introduced to the system. For numerical analysis, only the fundamental mode of the nano-resonator is considered. Figures 5.9 (a), (b) and (c) show the SP population variation on a log scale with respect to the time for different gain values and SP mode energies (lines with different colours represent different initial SP populations ( $N_{np}$ ) introduced to the system from an external system.). Comparing Figure 5.9 (a) and Figure 5.9 (b) indicate, that, for a lower gain value of  $5 \times 10^{12} \text{ s}^{-1}$ , the system reaches a steady state within 400 fs and for higher gains, such as  $8 \times 10^{12} \text{ s}^{-1}$ , the system reaches a steady state within 300 fs. This occurs because of the strong feedback from the spaser which is a typical behaviour the spasers. However, this effect is high compared to the silver based resonators described in reference [18]. Even after SP mode the energy increases to 248.14 meV and the system becomes stable within 400-500 fs. The output characteristics of the proposed design indicates that the gain significantly affects the dynamic responses of the system. Figures 5.9 (d), (e) and (f) illustrate the population inversion of each case shown in Figure 5.9 (a), (b), and (c) respectively. In each case population inversion changes rapidly and becomes stable at a value close to zero ( $\approx 0.001$ ). This effect also occurs due to the strong feedback of the design compared to the existing spaser designs (i.e. resonators based on gold and silver [18,21]).

The performance of the system under a pulse pumping condition was then analysed. The gain medium population is inverted at  $t = 0$  to saturate the higher energy levels of the active medium using a short pump pulse of 100 fs. Simultaneously, at  $t = 0$  plasmons are injected to the system from an external nano-plasmonic circuit. In response, the spaser provides an amplified pulse of SP population. This scenario is illustrated in the Figure 5.10. Figure 5.10 (a) shows the analysis of the SP population when the spaser is pulse pumped from  $t = 0$  to  $t = 100$  fs and operating at an SP mode energy of 206.78 meV (50 THz). Figure 5.10 (b) shows the SP population for the same pulsed pump conditions explained above at an SP mode frequency of 60 THz. Figure 5.10 (a), shows that, despite the initial population introduced at  $t = 0$ , the spaser generates a series of SP pulses that, exceed a threshold of  $N_{np} \sim 80$ . The underlying reason for this rapid depletion of the inversion is the strong feedback of the spaser as described above, where the energy is

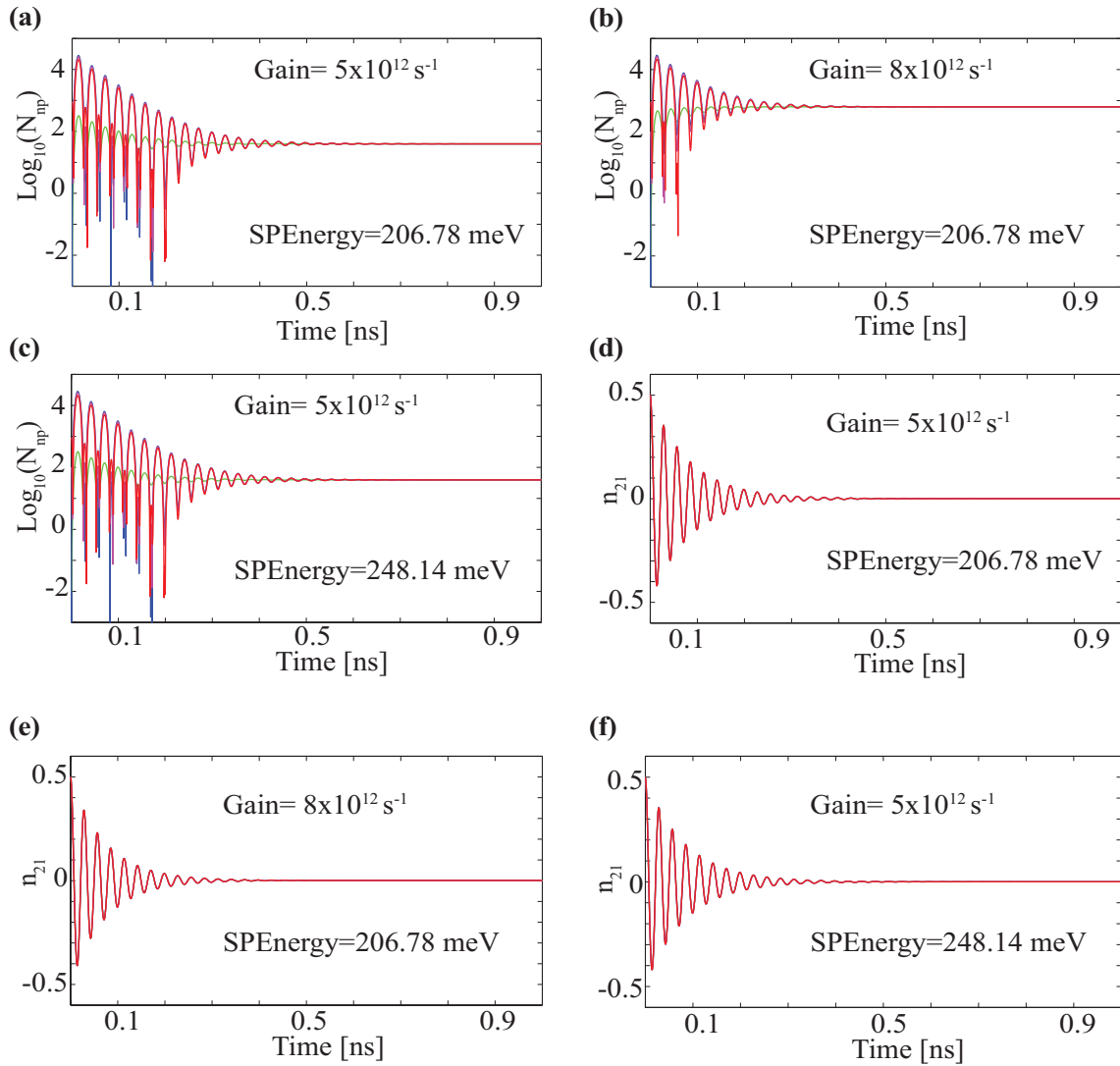


Figure 5.9: **(a)** The number of SPs per mode in log scale with time when the gain is  $5 \times 10^{12} \text{s}^{-1}$  and mode energy is 206.78 meV. (Different colours represent different initial no of SPs). **(b)** Same as **(a)** when the gain is  $8 \times 10^{12} \text{s}^{-1}$  and mode energy is 206.78 meV. **(c)** Same as **(a)** when the gain is  $5 \times 10^{12} \text{s}^{-1}$  and mode energy is 248.14 meV. **(d)** Variation of the population inversion ( $n_{21}$ ) with respect to time when the gain is  $5 \times 10^{12} \text{s}^{-1}$  and mode energy is 206.78 meV. **(e)** Same as **(d)** when the gain is  $8 \times 10^{12} \text{s}^{-1}$  and mode energy is 206.78 meV. **(f)** Same as **(d)** when the gain is  $5 \times 10^{12} \text{s}^{-1}$  and mode energy is 248.14 meV.

dissipated in the graphene resonator of the spaser. The characteristic duration of this pulse is 50 fs, which is defined by the depletion of the population inversion controlled by the energy transfer and SP relaxation rate [18,21]. The lower population (in purple) later produces an amplification, which implies that the spaser functions as a convertor of

pulse amplitude to time delay [18].

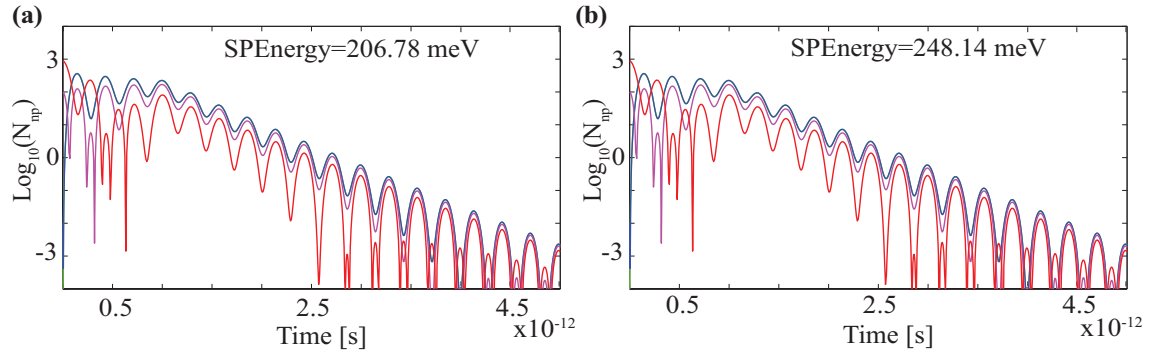


Figure 5.10: Variations in the number of SPs pver time after making the gain 0 and at 100fs **(a)** when mode energy is 206.78 meV and **(b)** when mode energy is 248.14 meV.

Figure 5.11 shows the modulated output of the spaser for the sine wave at frequency of 10 THz. Four different spaser configurations are considered with different SP mode energies. Figure 5.11 (a) shows the output number of SPs generated over time when the SP mode energy is 82.71 meV (20 THz). Figure (5.11) (b), (c) and (d) show the SP population for SP mode energies 206.78 meV (50 THz), 248.14 meV (60 THz) and 413.57 meV (100 THz) respectively. For each of the case, the system becomes stable after 350 fs. In addition, for lower SP mode energies, variation in the amplitude of the modulated SP population is relatively small compared to higher SP mode energies. In all cases, the system decreases the number of SPs and then settles and oscillates at approximately 40 surface plasmons per spasing mode. The total electric field variation can be obtained from equation (4.11). which implies that the design can be used as a SP amplitude modulator in nanoplasmonic circuitries. Due to the design of the VCSEL, the VCSEL electrodes can be used to input the signal to the system. The VCSEL output will then vary according to the input wave The graphene nano-resonator also provides SP variation according to the input wave. Thus, the system works as a electronic signal to a SP modulator.

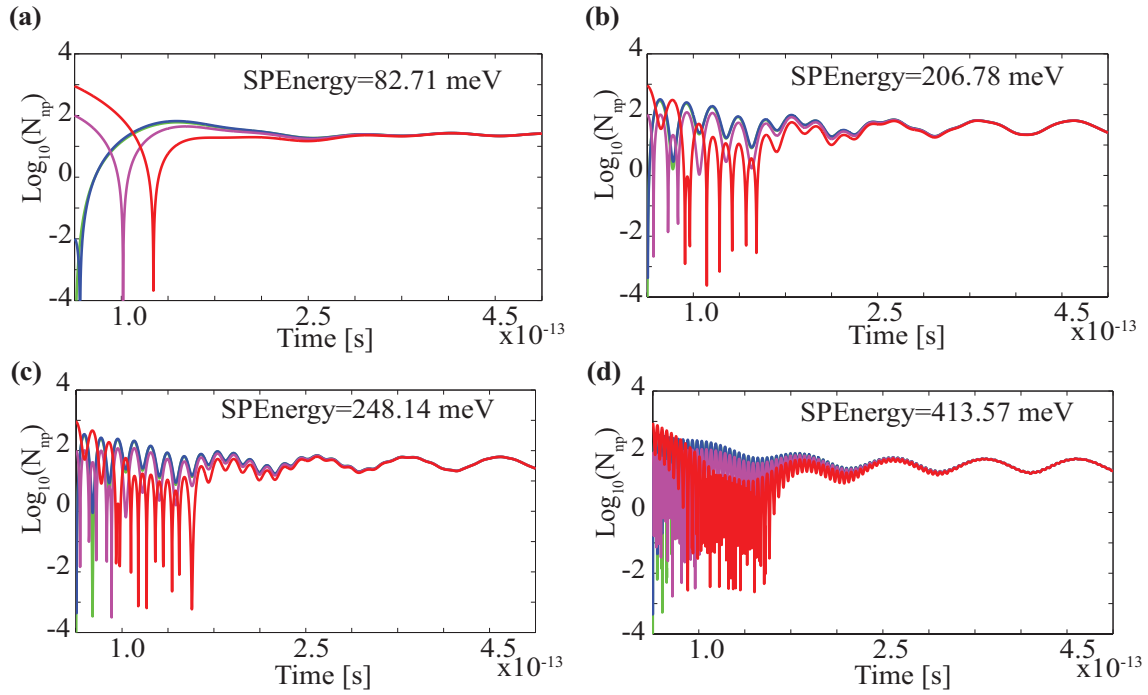


Figure 5.11: Variations in the number of SPs generated on log scale **(a)** When the SP mode energy is 20 THz **(b)** 50 THz **(c)** 60 THz and **(d)** 100 THz respectively.

## Conclusion

In this section, the continuous wave and dynamic operation of a spaser is analysed. Possibilities of a spaser operating as a coherent SP source, an amplifier, or a modulator are demonstrated. Due to the inherent feedback of the spaser, a conventional amplifier was not achieved from the spaser. However, it can be used as an amplifier before it reaches the steady state ( $<300$  fs). It also works as a pulse amplitude to time delay modulator for a very small initial population and as an SP amplitude modulator. Although several analyses have been conducted on the function of a spaser as an amplifier [18,21], previous designs used a spherical resonator made of silver or gold. Due to the spherical setup, pumping is not easy and the efficiency is much lower. Moreover, coupling such a system with plasmonic nano-circuitry is difficult. The proposed design consists of a two-dimensional resonator, Therefore, gain mediums can be placed over the flake and pumped easily and efficiently compared to existing designs, In addition to two-dimensional geometry, the circular shape provides enhanced coupling between the VCSEL and the system. In con-

trast to the conventional lasers, the VCSEL has smaller dimensions and the output beam of the VCSEL matches with two-dimensional circular configuration. Quantum theory based on optical Bloch equations is used to analyse the dynamics of the proposed design. Furthermore, the gain medium is treated quantum mechanically and the plasmonic system is considered quasi-classically. This same semi classical approach is also used in laser physics. Therefore, this approximation appears reasonable and reliable considering the output characteristics of the spaser [18].

First the CW operational regime of the spaser is considered. In the CW mode of operation, this spaser provides many SPs and makes the output electric field intensity higher than existing devices. Moreover, due to the plasmonic properties of graphene, the spaser poses higher mode energies, a higher quality factor, and a lower threshold gain [7]. The relationship between the gain and the number of plasmons is provided in addition to the dependency of the SP population on the radius of the flake. The design can be tuned according to number of SP outputs (intensity), considering the required gain, the SP mode energy, the electric field output, the threshold gain, and the plasmon quality factor. The device can easily be tuned and it has wide range of tuning values (*e.g.* plasmon resonance, mode energy, SP population, and electric field intensity) compared to the designs made of noble metals.

The main results of this analysis is associated with the ultra-fast behaviour of the spaser as shown in the Figure 5.9. Within the transient regime, the design works as an amplifier, considering the results from Figure 5.10, the system works as a pulse amplitude to time delay modulator. The system can also be used as a SP amplitude modulator as shown in the Figure 5.11. From the given information, optimum parameters for constructing a spaser can be selected considering the application. These design considerations are described in Chapter 7

In conclusion, given the geometrical aspects and design considerations, the device can be fabricated with the epitaxial growth method. The geometry provides optimal cou-

pling between the pump and active medium. Moreover, the two-dimensional geometry opens the applicability of this design to various nano-plasmonic applications without being restricted to ultra-fast optoelectronics in on-chip circuits, nano-lithography, and nano-scopy. This analysis provides a detailed framework for understanding the design procedures of a circular graphene spaser for different types of applications including a coherent SP source, an SP amplifier and an SP modulator.

### 5.3 Spaser made of un-doped graphene

One of the drawbacks of the previously described spaser designs is that the plasmonic nano-resonator must be doped to achieve plasmon resonance at IR - visible wavelengths. since the mono-layer intrinsic graphene does not provide plasmon resonance. In the MLG, layer separation is high and there is not tunnelling between electrons in layers. These layers act as two different atomic thick graphene layers. However, researchers have found that tightly bonded graphene layers can provided plasmon resonance in intrinsic graphene. This scenario is described in the Section 4.1.1.2. The design of the spaser is similar to the previous design considered in this chapter, except that the plasmonic nano-resonator is replaced by a circular bi-layer graphene flake. Therefore, the proposed spaser is an optically pumped, quantum dot powered circular graphene assembly.

#### 5.3.1 Results and discussion

The frameworks for analysing the steady state and dynamic responses of the circular spasers as described in the Chapter 3 and Chapter 4 were used to analyse the performance of the proposed design. Un-doped graphene was considered for the analysis, though bi-layer graphene can be doped and tuned over a wide range of wavelengths varying from IR to NIR. Similar to MLG, the conductivity of BLG also depends on the doping level and the operating wavelength. By considering the intraband and interband contributions of

graphene, the complex conductivity of the BLG can be derived as follows:

$$\sigma_{\text{BLG}}(\omega) = \frac{ie_0^2}{2\pi\hbar} \left\{ \frac{|E_F + \zeta| + |E_F - \zeta|}{\hbar(\omega - i\tau^{-1})} \right\} + \frac{ie_0^2}{8\pi\hbar} \left\{ \ln \left[ \frac{2|E_F + \zeta| - \hbar(\omega - i\tau^{-1})}{2|E_F + \zeta| + \hbar(\omega - i\tau^{-1})} \right] + \ln \left[ \frac{2|E_F - \zeta| - \hbar(\omega - i\tau^{-1})}{2|E_F - \zeta| + \hbar(\omega - i\tau^{-1})} \right] \right\}. \quad (5.12)$$

. where all the symbols the same meanings as described in the previous sections.

The steady state responses of the design, including, the electric field amplitude, the SP mode energy, the Q-factor, and the threshold gain are illustrated in the Figure 5.12. Figure 5.12 (a) shows the spaser mode energy variation with respect to the flake radius. Similar to the previous designs, a flake radius spanning from 30 nm to 100 nm is considered in this analysis. By varying the radius of the flake, spaser mode energy can be tuned of varying from 0.1 eV to 0.6 eV. According to Figure 5.12(a) when the radius of the nano-resonator becomes smaller, it supports higher spaser mode energies a larger radius. Figure 5.12 (b) shows the tunability of electric field amplitude of the resonator with respect to the flake radius. This resonator supports higher electric field amplitudes at  $11 \times 10^8$  V/m. Furthermore, Figure 5.12 (b) demonstrates that the electric field of the nano-resonator can be tailored by changing the radius. The electric field can also be tuned by varying the doping level of the flake as described in previous sections. Figures 5.12 (c) and (d) illustrate the threshold gain requirement of each mode and the Q-factor variation of the modes respectively. The proposed design requires less threshold gain than MLG, Gold and Silver. The minimum Q-factor is 10 when the flake radius is 100 nm and it can be increased by more than 50 by reducing the resonator radius to 30 nm. The resonator radius can not be reduced to a few nanometres due to the non-local effects of the quantum objects.

A study is was conducted to analyse dynamic responses of the propose spaser design in the time domain. Figure 5.13 shows the characteristics of the design in time domain under the continuous pumping condition with a gain of  $6 \times 10^{12} \text{ s}^{-1}$ . Lines in different colours represent different initial populations injected into the system at  $t = 0$ . Figures 5.13 (a), (b) and (c) Show the number of surface plasmons generated for the funda-

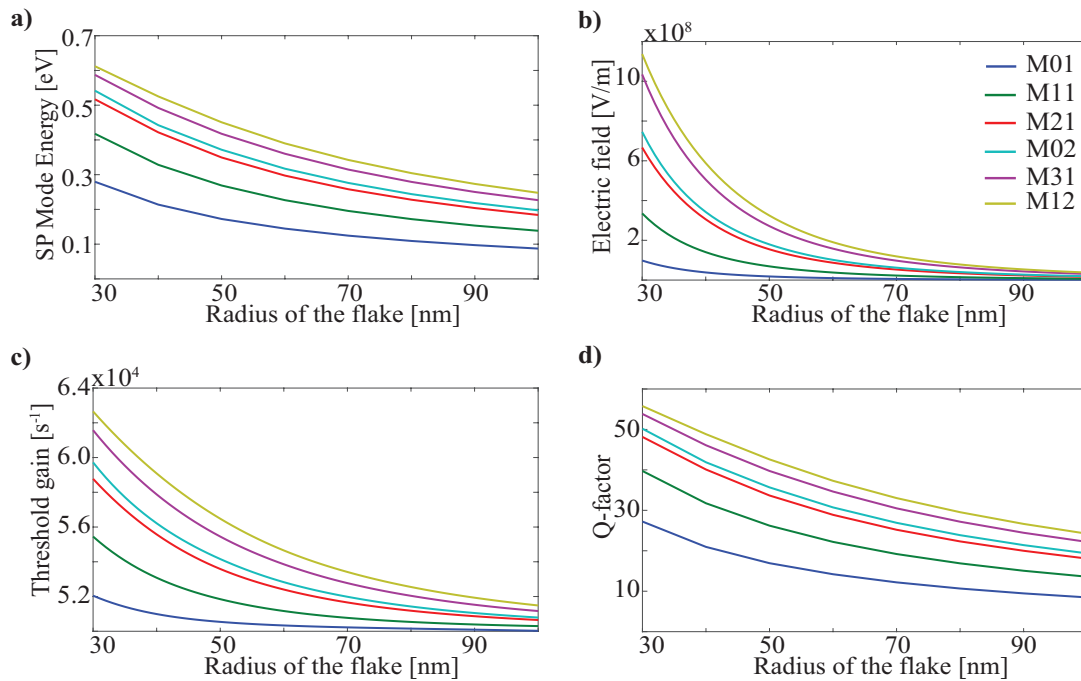


Figure 5.12: Steady state responses of first six lowest energy modes of the bi-layer graphene based spaser. **a)** Spaser mode energy variation with respect to the radius of the flake. **b)** Electric field amplitude versus the flake radius. **s)** Threshold gain requirement of each mode with respect to the flake radius. **c)** Q-factor variations of each mode for the varying flake radius.

mental mode when the spaser is operating with a mode energy of 0.09 eV, 0.17 eV and 0.28 eV respectively. As BLG supports lower mode energies compared to doped MLG, this proposed spaser provides  $\sim 900$  SPs per spasing mode regardless of the spaser mode energy which is considerably higher than highly doped MLG. Spaser mode energies supported by the BLG based spaser can be used effectively in biomedical applications. Due to the strong feedback of the spaser, this design is less applicable as an amplifier, but can be used as a coherent, intense, localised surface plasmon source since these are important characteristics that are required for biomedical applications.

The proposed design also can also be used as an SP modulator. Three different spaser configurations are considered with flake radius of 30 nm, 50 nm, and 100 nm. A pulse lasting in 100 fs and a sine wave of 10 THz are given to the systems and analysed the output characteristics of the designs. The results are illustrated in the Figure 5.14. Under

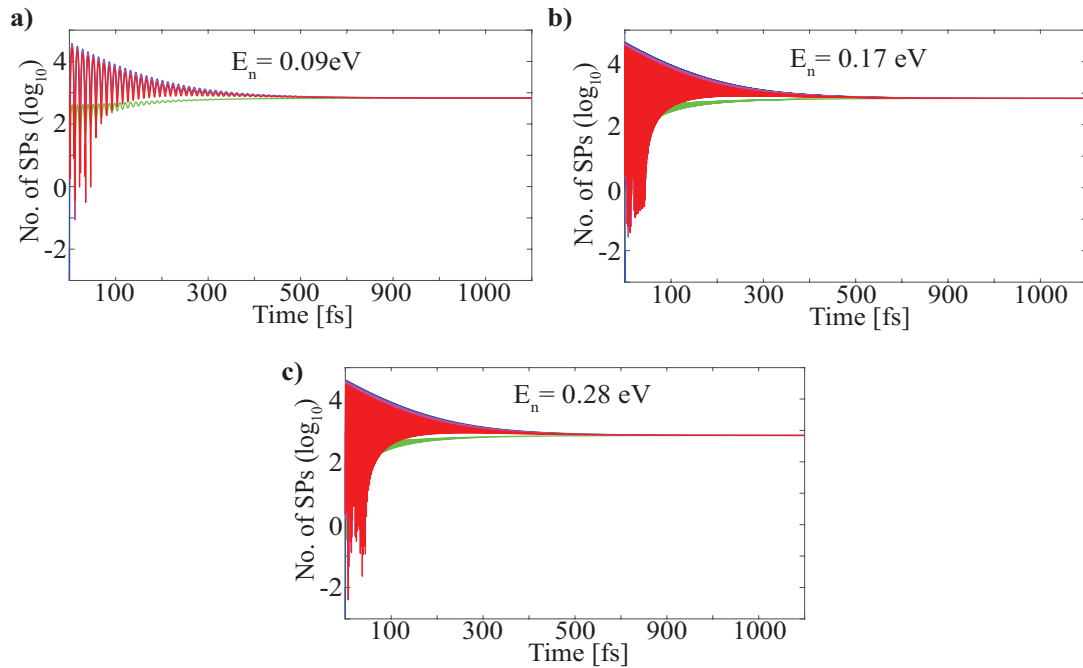


Figure 5.13: Variation the number of SPs generated on a log scale (a) When the SP mode energy is 20 THz (b) 50 THz (c) 60 THz and (d) 100 THz.

pulse pumping, at  $t = 0$ , the spaser is continuously pumped for 100 fs and the pumping stops the after 100 fs. Figure 5.14 (a) shows the output response of the spaser under pulse pumping condition when the spaser is operating at 0.09 eV. Figure 5.14 (b) and (c) also show the output response of the spaser under the pulse pumping condition when the spaser is operating at 0.17 eV and 0.28 eV respectively. When the spaser is operating at 0.09 eV (lower SP mode energy), the number of plasmons in the system increases to values in the order of  $\sim 10^6$ . However, when the spaser is working in higher spaser mode energies, such as 0.17 eV or 0.28 eV, the number of SPs generated approaches to  $\sim 1000$  (1047 exactly) for both cases and the rapidly declines to zero (requires more than 750 fs) immediately after removing the pump. Figures 5.14 (d), (e) and (f) show the output responses correspond to sine wave modulation. In all three spaser configurations, the systems oscillates around 700 surface plasmons per spasing mode. Moreover, for the initial populations ranging from 1 to 100, the SP population rapidly declines in the first 100 fs and then begins to increase after 120 fs.

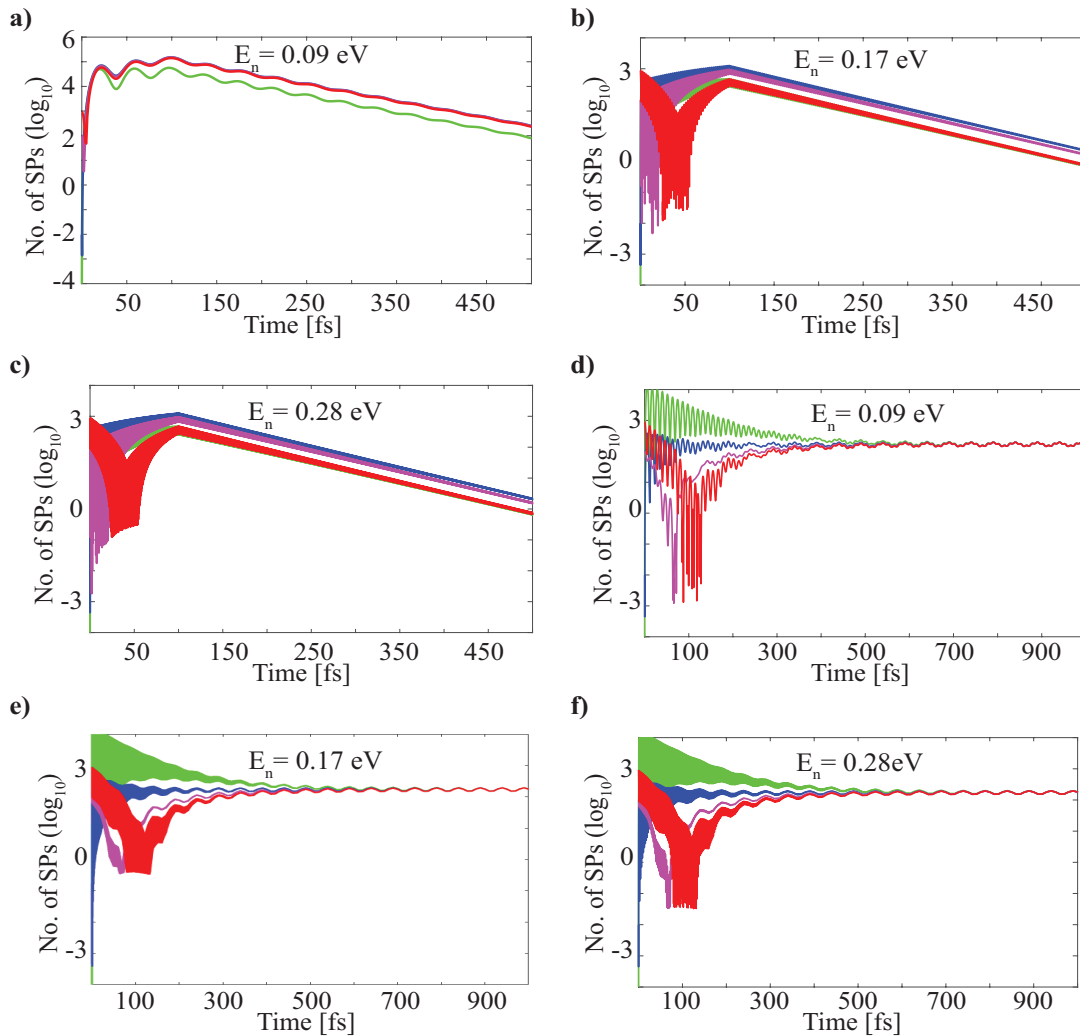


Figure 5.14: Variations of the number of SPs generated on a log scale (a) when the SP mode energy is 20 THz (b) 50 THz (c) 60 THz and (d) 100 THz.

### 5.3.2 Conclusion

This analysis provides the steady state and transient responses, such as SP mode energy, electric field amplitude, Q-factor, and number of SPs generated per spasing mode of a bi-layer graphene base spaser. The most unique finding is that the design provides plasmon resonance at zero doping. Therefore, the proposed device can be used effectively in biomedical applications. Spasers made of bi-layer, non-doped graphene can be used as an alternative to chemotherapy owing due to their surprising properties. such as the design made of un-doped graphene, higher output tightly confined and localised output.

Since the size of these spaser is a few hundred nanometres, a set of spasers can be used to cover a cancer cell. Moreover this device works in IR wavelengths and, the spasers can be powered externally from the outside of the body using a strong pump laser that matches the injected spasers. The proposed design is not only applicable in biomedicine, but also to opto-electronics circuits, nano-lithography, and nano-scopy.

## 5.4 Summary

This chapter describes three different spaser designs based on graphene. All the designs are based on a circular shaped nano-resonator and the first design is an electrically pumped spaser made of mono-layer graphene and powered by a quantum cascade well. Due to the surprising properties of graphene and the quantum cascade well, such as thermal and mechanical stability, higher outputs, ease of fabrication and ease of tuning, the device demonstrates higher and more efficient outputs compared to existing spaser designs based on graphene and noble metals. This section also presents the operational characteristics of the proposed spaser design. These details can be used to analyse a similar spaser setup or design a high power spaser since the framework provided is general and supports analysis of two-dimensional resonator based spasers.

The second configuration is an optically pumped spaser made of mono-layer graphene and quantum dots are powered by a VCSEL. This design is analysed and the operational characteristics are described using the framework developed and presented in Chapter 3. This study demonstrates the applicability of a graphene based spaser as a coherent SP source, an SP amplifier, and an SP modulator.

The third spaser configuration is also an optically pumped spaser, but the nano-resonator is replaced by a bi-layer graphene nano-resonator. The shape of the resonator is the same and this particular design provides spasing without doping the resonator. Therefore, this design has applications in opto-electronics and in biomedicine. A spaser

made of bi-layer graphene only supports SP mode energies varying from 0.09 eV to 0.28 eV (Far-IR to Mid-IR) and these values are slightly lower than MLG. However, spasers based on BLG provide higher electric field amplitude than designs made of MLG, which is an important characteristic to consider making when biomedical instruments. The major problems with using spasers in biomedicine are heavy metals such as gold and silver, which are not good for the human body and two-dimensional materials that must be doped to achieve plasmon resonance at commercially useful wavelengths. To address this problem, the proposed design is non-toxic and provides plasmon resonance at IR wavelengths with a higher electric field amplitude, which are optimal outputs that are necessary for biomedical applications.

# Chapter 6

## An MoS<sub>2</sub>-based spaser

**T**WO-dimensional (2D) materials have gained popularity regarding potential real-world applications, and molybdenum disulfide (MoS<sub>2</sub>) has emerged as a contender for graphene alternative with many unique optical and electrical properties [1–3]. These materials are well suited for ultra-thin nanodevices. Due to recent advances in nano-fabrication technology that has emerged during the last decade, it is possible to design ultra-fast and ultra-compact nanodevices that work in a quantum regime [1,2]. The critical dimensions of the devices are much smaller than the operating wavelength of the device and must overcome the limitations imposed by the diffraction limit [1]. A design which has critical dimensions in nanometre scale and can provide an electric field with the use of amplified surface plasmons is called as a spaser. This chapter, provides design details followed by a comprehensive analysis of an optically pumped, quantum dots powered, MoS<sub>2</sub> nano-resonator based spaser.

### 6.1 Introduction

Although much research has been done on spasers, the results depend on the model and most of the studies focus on spasers made of noble metals [6,27]. Although graphene is the most well frequently studied two-dimensional material, it is useful to model and analyse the characteristics of a device made of MoS<sub>2</sub> to enhance the efficiency. Furthermore, the optimal design parameters of an MoS<sub>2</sub> based spaser are essential to realising ultra-speed nano-optical devices. In this analysis, a circular spaser made of MoS<sub>2</sub> is con-

sidered for analytical tractability. A set of comprehensive design guidelines is provided to select the spaser's output mode energy with a particular mode and the output electric field intensity by varying the design parameters.

In this study, an MoS<sub>2</sub> spaser is analysed which is powered by quantum dots that operate in the range spanning the visible and infrared (IR) wavelengths (775 nm to 5  $\mu\text{m}$ ). A highly doped MoS<sub>2</sub> flake is used to obtain SPs at lower wavelengths [32]. Since the radius of the nanopatch is finite, localised surface plasmon modes are considered. Localised SP modes that are supported by the device are identified and the plasmon excitation rate and the electric field output of the device are analysed. In addition, the tunability of the electric field output, plasmon excitation rate, spaser mode energies and threshold gain requirements for continuous spasing are demonstrated.

This chapter is organized as follows: in Section 6.2.1, Section 6.2.2 and Section 6.2.3, design details of the spaser are provided regarding spaser modes and their degeneracy. Construction details and design considerations are also provided and can be used to fabricate the active medium and tune the proposed spaser design. Section 6.2.4 address the major results of the analysis with a detailed analytical model of the device and followed by a comprehensive analysis of the operating characteristics and tunability of the MoS<sub>2</sub> spaser.

## 6.2 Results and Discussion

### 6.2.1 Design of the spaser

The spaser proposed in this study consists of a circular, highly doped molybdenum disulfide resonator and a ring of quantum dots (QDs). The model described in this work is shown in Figure 6.1(a). To provide gain, gain chromophores (QDs) are placed on top of the two-dimensional MoS<sub>2</sub> resonator, maintaining a gap between the ring and the flake as illustrated in the Figure 6.1(a). Although any type of gain chromophores (described

in the Chapter 7) can be used to make this spaser. Here, semiconductor QDs are considered as the gain chromophores here. It is possible to replace the QDs with dye molecules which have a higher packing density than semiconductor QDs [18]. A spaser can be powered either optically or electrically. In this study, optical injection was used *via* a vertical cavity surface emitting laser (VCSEL) as shown in the schematic diagram. Due to the two-dimensional circular shape of the VCSEL and the higher power output, a VCSEL is used to excite the QDs of the proposed design [133].

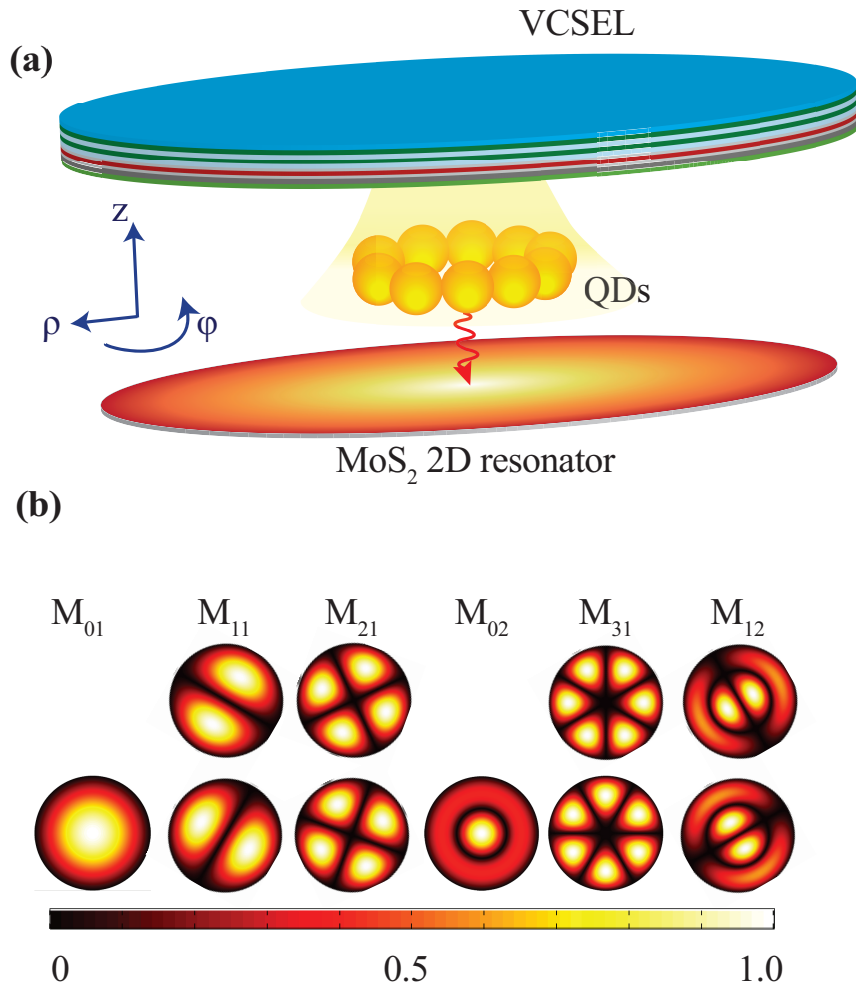


Figure 6.1: **(a)** Schematic diagram of proposed circular spaser made of highly doped  $\text{MoS}_2$  circular resonator with optically pumped a ring of quantum dots. **(b)** Normalized electric field distribution of first six lowest energy SP modes of the resonator.

Excited electrons in the QDs provide energy to generate coherent plasmons in the MoS<sub>2</sub> resonator. Furthermore, the MoS<sub>2</sub> circular resonator supports a set of modes similar to the graphene SP modes, as shown in Figure 6.1(b). These eigenmodes overlap with the emissions of the QD and produce spasing and doping of MoS<sub>2</sub> is required to obtain SPs at lower wavelengths. The large separation between the MoS<sub>2</sub> layers provides an ideal place to accommodate the guest species. Through a process known as intercalation, the guest species such as alkali metal ions (Li<sup>+</sup>, Na<sup>+</sup> and K<sup>+</sup>) can be accommodated within the separation and can be achieved *via* electrochemical doping [32, 141]. Intercalation causes changes in the host materials' electronic structure [141] and Li intercalation was used to obtain higher carrier density (changes plasma wavelength of the MoS<sub>2</sub> nanopatch). Lithium intercalated MoS<sub>2</sub> is denoted as Li<sub>x</sub>MoS<sub>2</sub> and recent researches have shown that, a charge carrier density of  $N_n = 16.84 \times 10^{27} \text{ m}^{-3}$  can be achieved via Lithium intercalation (Li<sub>1.000</sub>MoS<sub>2</sub>) [32, 141]. A charge carrier density  $N_n$  of  $8.85 \times 10^{27} \text{ m}^{-3}$  can be achieved with Li<sub>0.500</sub>MoS<sub>2</sub> intercalates and Li<sub>0.625</sub>MoS<sub>2</sub> intercalates can have a charge carrier density of  $12.94 \times 10^{27} \text{ m}^{-3}$  [32].

### 6.2.2 MoS<sub>2</sub> resonator and degeneracy modes

A circular MoS<sub>2</sub> nano-resonator is considered, with a radius spanning from 30 nm to 100 nm. The SP modes of the nanoresonator ( $\omega + i\gamma$ ) are obtained from  $\nabla \cdot [\Theta(r) - S_n] \nabla E_k(r) = 0$ , where  $\Theta(r)$  is equal to 1 inside the inclusions and to 0 outside referred to as the characteristics function [6]. Moreover, the eigenfrequency of the resonator  $\omega_{sp,n}$  satisfies  $S(\omega_{sp,n}) = S_n$  where  $S(\omega) = [1 - \epsilon_m(\omega)/\epsilon_d]^{-1}$  is Bergmans' spectral index. Here,  $\epsilon_m(\omega)$  is the permittivity of the plasmonic metal and  $\epsilon_d$  is the permittivity of the surrounding dielectric [6, 18, 21]. The SP modes of the resonator are found numerically using the commercial software COMSOL Multiphysics.

Recent work has shown that highly doped MoS<sub>2</sub> flakes support localised plasmon modes within the visible to IR wavelengths range (380 nm to 5000 nm) [32, 141]. Within this range, by considering the circular boundary conditions, the electric field distribution

of the flake is assumed to have the following form in a cylindrical coordinate system [7]:

$$\mathbf{E}_{\text{sp}} = \begin{pmatrix} E_{z^+} \\ E_{z^-} \end{pmatrix} = \begin{cases} E_{np} J_n(k_\rho \rho) \cos(n\phi) e^{-k_{z^+} z}, & z \geq 0 \\ E_{np} J_n(k_\rho \rho) \cos(n\phi) e^{k_{z^-} z}, & z < 0. \end{cases} \quad (6.1)$$

where each mode is characterized by two letters  $(n, p \in \mathbb{Z}^+)$ .  $E_{np}$  is the amplitude of electric field towards the  $z$ -direction,  $k_{z^+}$  is the wave vector towards the positive  $z$ -direction,  $k_{z^-}$  is the wave vector towards the negative  $z$ -direction and  $J_n$  is the  $n^{\text{th}}$  order Bessel function of the first kind.

The resonator supports a set of localised surface plasmon modes that can be excited externally as describe in the following sections. The obtained modes of the resonator and their normalized electric field distributions are shown in Figure 6.1(b). Due to the geometry of the resonator (*i.e.* sphere, disc, rectangle, etc.) the degenerated modes can be seen in the resonators. These degenerated modes resonate at the same frequency and carry same amount of spaser mode energy [24]. In Figure 6.1(b) shows that,  $M_{11}$ ,  $M_{21}$ ,  $M_{31}$  and  $M_{12}$  have degenerated twice as much due to the shape of the resonator.

The operating wavelength of these modes depend on the frequency dependent permittivity of the  $\text{MoS}_2$  flake. Recent researches has been done to obtain the characteristics of the dielectric properties of  $\text{MoS}_2$  to analyse the optical responses of  $\text{MoS}_2$  layers at IR and the visible wavelengths. These studies have shown that the complex permittivity of  $\text{MoS}_2$  can be modelled with a Lorentz-Drude model [32, 70, 71]. and the complex permittivity can be derived from equation 4.8

The spatial decay of the electromagnetic field away from the  $\text{MoS}_2$  layer is determined by the decay rates  $k_{z^+}$ ,  $k_{z^-}$  and follow the dispersion relation of:

$$k_{z^+} = \sqrt{k^2 - \epsilon_1 \left( \frac{\omega_{\text{sp}}}{c} \right)^2}, \quad (6.2)$$

$$k_{z^-} = \sqrt{k^2 - \epsilon_2 \left( \frac{\omega_{\text{sp}}}{c} \right)^2}, \quad (6.3)$$

where,  $k(\omega)$  is the plasmon wave vector which can be obtained using the following equation.

$$\mathbf{k}(\omega_{\text{sp}}) = \frac{\omega_{\text{sp}}}{c} \sqrt{\frac{\epsilon_r \epsilon_m(\omega)}{\epsilon_r + \epsilon_m(\omega)}}, \quad (6.4)$$

where,  $\epsilon_r$  and  $\epsilon_m(\omega)$  are permittivities of the surrounding material and meta material respectively. For realistic wavelengths considered in this work, the wavelength of the light in vacuum is much smaller than the plasmon wavelength ( $k \gg \omega^2/c^2$ ). Thus, the dispersion relation can be approximated as follows:

$$k_{z+} \approx k_{z-} \approx \mathbf{k}(\omega_{\text{sp}}) = \frac{\omega_{\text{sp}}}{c} \sqrt{\frac{\epsilon_r \epsilon_m(\omega)}{\epsilon_r + \epsilon_m(\omega)}}, \quad (6.5)$$

### 6.2.3 Active medium and the operation of the spaser

The characteristics of the active medium determine the strength of the interaction of electron-hole (e-h) recombination with the SP modes of the resonator. In addition, strength of the e-h recombination determines the amount of amplification that each SP mode receives. The quantum mechanical model of the proposed design considering the degenerated modes is shown in Figure 6.2. Here, A three level gain medium and plasmons with degenerated modes are considered here. The total system consists of  $n$ -states and the first three states are for denote states of the gain medium and the fourth to  $n^{\text{th}}$  states denote states of the plasmons and degenerated plasmons.  $|1_g\rangle$  and  $|2_g\rangle$  represent the

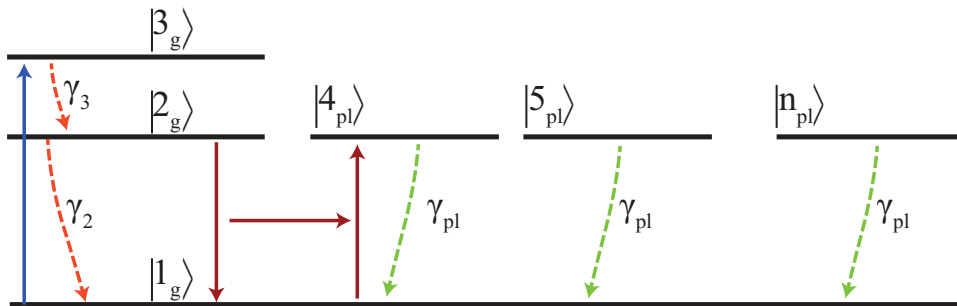


Figure 6.2: Quantum mechanical model of the spaser with  $n$ -states considering degeneracy modes of the resonator.

ground and excited states of the chromophore respectively. An assumption is made as SP eigenmodes resonate with the transition  $|2_g\rangle \rightleftharpoons |1_g\rangle$ . To achieve gain in this two-level system by population inversion, it is essential to introduce a third level  $|3_g\rangle$ . However this third level is pumped optically and population decays rapidly to the  $|2_g\rangle$ . The active medium receives energy *via* a VCSEL and electrons at ground state change to higher states receiving the energy. Then,  $|2_g\rangle \rightarrow |1_g\rangle$  the transition emits energy to the resonator non-radiatively [127] and generate SPs. The generated SPs stimulate the process and produce spasing. Due to the properties of the proposed spaser assembly, both the temporal and spatial coherence of the field can be maintained provided stimulated emission take place inside the cavity [93,94,142]. The process can be further analysed by considering the Hamiltonian of the spaser and the density matrix [143] elements for the interaction between plasmons and the gain medium as described in Chapter 3.

#### 6.2.4 Analysis of the performance

Only the six lowest energy modes of the spaser were analysed. Figure 6.3(a) and (b) show the SP mode energy for the varying radius ( $R$ ) of the resonator when  $N_n = 10.87 \times 10^{27} \text{ m}^{-3}$  and  $N_n = 12.94 \times 10^{27} \text{ m}^{-3}$  respectively. The device emits an output spaser mode energy variation from 0.10 eV to 1.60 eV displaying the ability to work from the Mid-IR to the visible range. The spaser mode is reduced when the radius of the resonator increases. The first mode ( $M_{01}$ ) can achieve a maximum spaser mode energy of 0.7 eV when the radius is 30 nm and  $N_n = 12.91 \times 10^{27} \text{ m}^{-3}$  and the 6<sup>th</sup> mode ( $M_{12}$ ) delivers a maximum SP mode energy of 1.60 eV which is in visible regime. It seems, that the system can be set to provide SP mode energy from 0.10 eV to 1.60 eV by changing the radius of the nano-resonator and doping level and setting the emission wavelengths of the QDs accordingly. The electric field intensity output of the proposed spaser was then analysed. According to equation (4.13), the output electric field intensity depends on the material parameters ( $\epsilon$ ), geometry of the spaser (radius) and SP mode wavelength ( $\omega_{sp}$ ). Figure 6.3(c) show the electric field output of the spaser when the charge carrier density of the resonator ( $N_n$ ) is  $8.85 \times 10^{27} \text{ m}^{-3}$ . Electric field intensity variations for charge car-

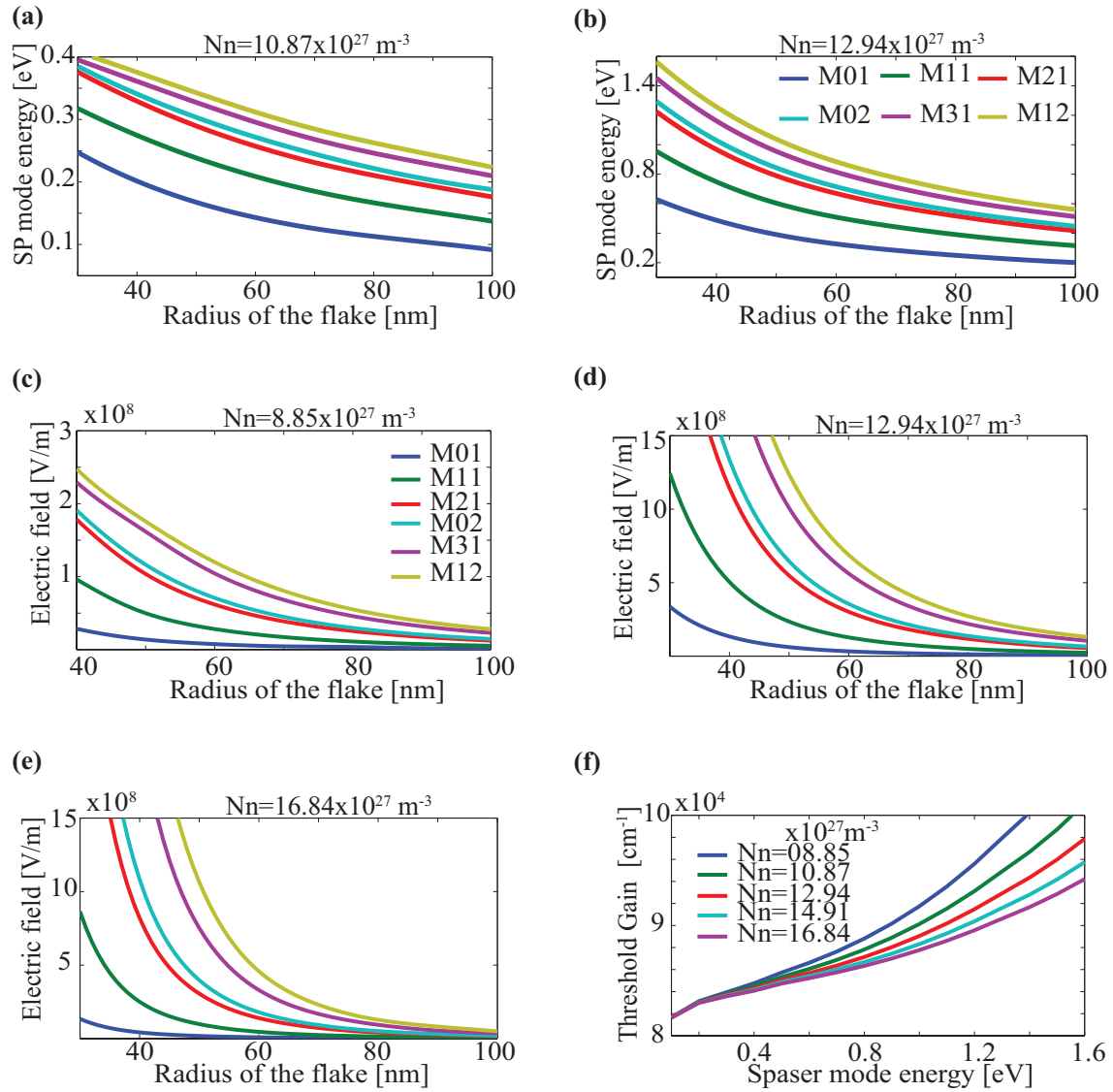


Figure 6.3: **(a)-(b)** SP mode energy output of the spaser with respect to the radius of the nano-resonator when  $N_n = 10.87 \times 10^{27} \text{ m}^{-3}$  and  $N_n = 12.94 \times 10^{27} \text{ m}^{-3}$  respectively. Electric field intensity of the spaser for varying resonator radius from 30 nm to 100 nm when **(c)** charge carrier density ( $N_n$ ) is  $8.85 \times 10^{27} \text{ m}^{-3}$ , **(d)**  $N_n = 12.94 \times 10^{27} \text{ m}^{-3}$ , and **(e)**  $N_n = 16.84 \times 10^{27} \text{ m}^{-3}$ . (the legend is common for the figures (a)-(e)). **(f)** Threshold gain requirement for continuous spasing for different charge carrier densities of the proposed spaser with spaser mode energy from 0.1 eV to 1.6 eV.

rier density from  $12.94 \times 10^{27} \text{ m}^{-3}$  to  $16.84 \times 10^{27} \text{ m}^{-3}$  are shown in Figure 6.3(d) and Figure 6.3(e) respectively. Figure 6.3(c)-(e) illustrate that the proposed design can achieve an electric field intensity higher than  $15 \times 10^8 \text{ Vm}^{-1}$  when the radius ( $R = 30 \text{ nm}$ ) and

at higher doping levels. The SP mode wavelength increases when the radius increases, Therefore, to obtain higher SP mode energy and electric field intensity, a smaller radius must be used by overcoming fabrication constraints. The proposed design made of MoS<sub>2</sub> delivers a higher electric field output and SP mode energy with fewer critical dimensions compared to the outputs of the currently proposed and designed spasers made of silver, gold and graphene [6,7,19,22].

It is essential to analyse amount of threshold gain ( $g_{th}$ ) required for continuous operation of the spaser. The threshold gain depends on spaser mode energy and MoS<sub>2</sub> nanopatch properties, which are functions of spaser geometry and material parameters. The amount of gain required for spasing is [21],

$$g_{th} = \frac{\omega}{c\sqrt{\epsilon_d}} \frac{\text{Re}[s(\omega)]}{1 - \text{Re}[s(\omega)]} \text{Im}[\epsilon(\omega)] \quad (6.6)$$

The threshold gain has a unit of "cm<sup>-1</sup>" and  $\epsilon_d$  is the permittivity of the surrounding dielectric. The threshold gain requirements for continuous spasing to obtain spaser mode energies from 0.10 eV to 1.6 eV for different charge carrier densities are shown in Figure 6.3(f). Higher charge carrier densities require lower threshold compared to lower carrier densities. The device requires minimum threshold gain of  $10.2 \times 10^4 \text{ cm}^{-1}$  to obtain spaser mode energy of 1.60 eV when  $Nn = 8.85 \times 10^{27} \text{ m}^{-3}$  and operate in the visible wavelengths (highest SP mode energy considered in this work) which can be achieved with semiconductor QDs [18,21]

The performances of a spaser is also depends on the number of SPs that can be generated in a unit of time which is called the plasmon excitation rate. The plasmon excitation rate of a spaser can be obtained from the following equation [22,24]:

$$\mathfrak{R}_{pl,k} = \alpha \omega_{sp}^2 \frac{\gamma_{2p}}{\gamma_{2p}^2 + (\omega_{12} - \omega_{sp})^2} |d_{13}^{(L)}|^2 \sum_{j=4}^n |d_{12}^{(K),j}|^2 . \quad (6.7)$$

The plasmon excitation rates of the proposed spaser design are shown in Figure 6.4(a) and (b). Figure 6.4(a) shows the normalized plasmon excitation rates of the six lowest en-

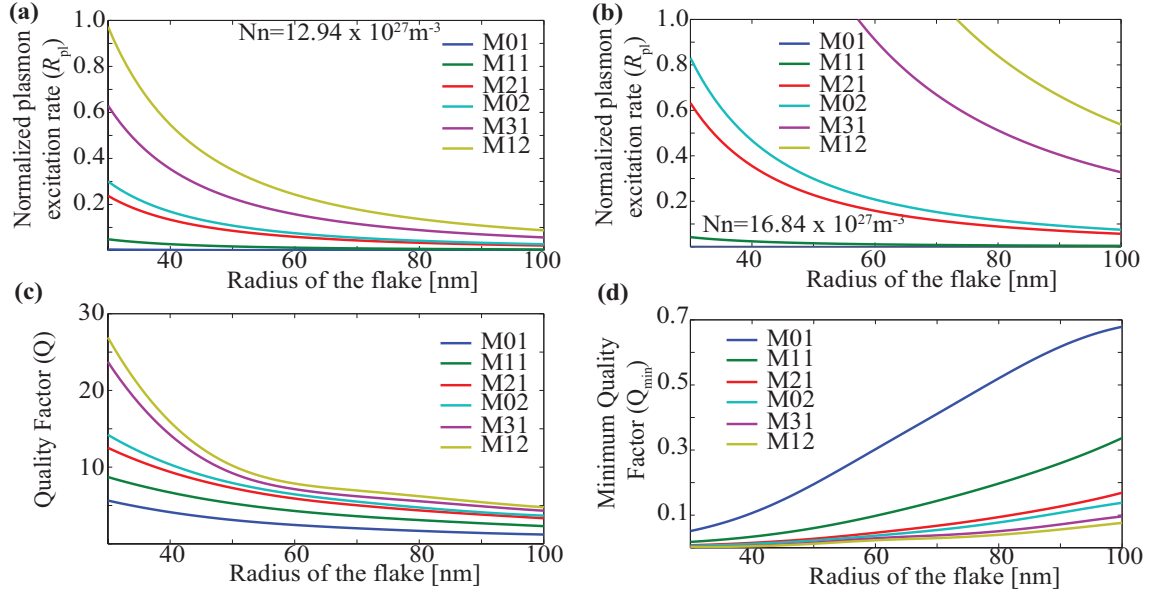


Figure 6.4: Normalized surface plasmon excitation rate for the six lowest energy modes supported by the device when the radius varies from 30 nm to 100 nm and **(a)** when the charge carrier density is  $N_n = 12.94 \times 10^{27} \text{ m}^{-3}$  and **(b)** when charge carrier density is  $N_n = 16.84 \times 10^{27} \text{ m}^{-3}$ . **(c)** Quality factor of the generated plasmons when  $N_n = 12.94 \times 10^{27} \text{ m}^{-3}$  Vs radius of the MoS<sub>2</sub> nanopatch. **(d)** Minimum quality factor requirement for continuous spasing for six lowest energy modes vs radius of the MoS<sub>2</sub> 2D resonator when  $N_n = 12.94 \times 10^{27} \text{ m}^{-3}$ .

ergy modes supported by the device, when the size of the resonator varies from 30 nm to 100 nm at a charge carrier density of  $12.94 \times 10^{27} \text{ m}^{-3}$ . Figure 6.4(b) illustrates the same for charge carrier density of  $16.84 \times 10^{27} \text{ m}^{-3}$ . These figures illustrate, at low radius values (which provide higher electric field intensities and mode energies), plasmon excitation is higher than at high radius values. In addition, high modes provide higher plasmon excitation rates compared to low modes. Considering the relationship in equation (6.7), a high electric field intensity and a high Q value are required to obtain a high plasmon excitation rate. Therefore, it seems that excitation rate can be increased by increasing the doping level and using a smaller resonator radius ( $R$ ).

#### 6.2.4.1 Condition for continuous spasing

The quality factor (Q) of the generated SPs is an important characteristic of the device since a spaser may not operate due to high loss associated with surface plasmons prop-

agation. Surface plasmons are collective oscillations of electrons and the half-life of the energy is stored as energy of the kinetic motions of electrons. Their magnetic component is negligible compared to a conventional, non-diffraction limited setup where optical resonances occur through periodic exchange of energy between electrical and magnetic fields [111, 112]. The remedy is to use kinetic energy in free electrons interacting with the field, restoring the energy balance for self-sustained oscillations. Furthermore spasers take advantage of this mechanism but this kinetic energy is lost from the system commensurate with the rate of scattering of electrons in metal [114–116]. The solution is to introduce gain using optical or electrical pumping to restore the energy loss from electron scattering [6, 117, 118]. Another approach is to design materials with less loss (*i.e.* low electron scattering rates) but higher free carrier densities [119]. Moreover the Q-factor measures the quality of the generated plasmons and higher Q yields low loss. The Q-factor depends on the material parameters and the operating wavelength. It is important to achieve a high Q value for efficient output. The Q value of the generated SPs can be obtained from [21],

$$Q = \frac{\omega}{2} \frac{\partial \text{Re}[\epsilon(\omega)] / \partial \omega}{\text{Im}[\epsilon(\omega)]}. \quad (6.8)$$

Figure 6.4(c) shows the quality factor of the produced plasmons when the radius varies from 30 nm to 100 nm at a charge carrier density  $N_n = 12.94 \times 10^{27} \text{ m}^{-3}$ . It seems the device can provide a Q-factor up to 27 which is a good value compared to the Q-factor of the noble metals such as gold and silver. However, the Q-factor of the MoS<sub>2</sub> resonator is slightly lower than that of graphene due to the higher imaginary component of the complex permittivity of the material. The design still provides a significant Q-factor, which can be used effectively in nano-optical applications. A condition for the existence of spasing is described below.

Considering the population inversion (since,  $n_{21} \leq 1$ ) of the spaser and the motion equations described by equations (3.6) and (3.8), a condition of continuous spasing can

obtained with, [18,21]:

$$\frac{(\gamma_n + \Gamma_{12})^2}{\gamma_n \Gamma_{12} [(\omega_{12} - \omega_{sp})^2 + (\gamma_n + \Gamma_{12})^2]} \sum_k |\Omega_{12}|^2 \geq 1, \quad (6.9)$$

At resonance  $\omega_{12} = \omega_{sp}$ , and, a necessary condition for the existence of spasing in a QD powered optically pumped circular MoS<sub>2</sub> spaser can be derived as follows,

$$\frac{4\hbar\omega_{sp}k_z |d_{12}|^2 e^{-2k_z\ell}}{\left(\epsilon_0\epsilon_b + \frac{\omega_p^2\epsilon_0(\omega_{sp}^2 - \gamma^2)}{(\omega_{sp}^2 + \gamma^2)^2}\right)} \geq \gamma_n\Gamma_{12}. \quad (6.10)$$

where  $\ell$  is the characteristic distance between the MoS<sub>2</sub> layer and the QD ring. Equation (6.10) introduces a condition of the plasmon polarization relaxation rate. Since,  $Q = \omega_{sp}/(2\gamma)$  a condition for plasmon quality factor (Q) for continuous spasing can be derived by:

$$Q \geq Q_{min} = \frac{\left[\epsilon_b(\omega_{sp}^2 + \gamma^2)^2 + \omega_p^2(\omega_{sp}^2 - \gamma^2)\right] \epsilon_0\Gamma_{12}}{8\hbar(\omega_{sp}^2 + \gamma^2)^2 k_z |d_{12}|^2} e^{2k_z\ell}. \quad (6.11)$$

The realistic parameters for the gain medium are  $d_{12} = 1.5 \times 10^{-17}$  esu,  $\ell = 6.0$  nm and  $\Gamma_{12} = 10$  meV [18] for the design that is considered in this study. Figure 6.4(d) shows the minimum Q required for existence of spasing. For all the modes considered, the  $Q_{min}$  value is always less than one and well below the Q values of generated SPs. Therefore, the device can work perfectly and effectively with a high quality factor, SP mode energy and electric field intensity and with fewer geometric dimensions than the presently proposed and designed spasers made of graphene and noble metals.

### 6.3 Comparison between MoS<sub>2</sub> and graphene resonators

A spaser is a promising device that is essential to creating ultra-fast and ultra-compact nano-devices [1,6]. Due to the properties of two dimensional materials such as graphene and molybdenum disulfide (MoS<sub>2</sub>), it is possible to design highly efficient spasers [19]. In contrast to graphene [33], the large tunability of surface plasmon (SP) resonance and

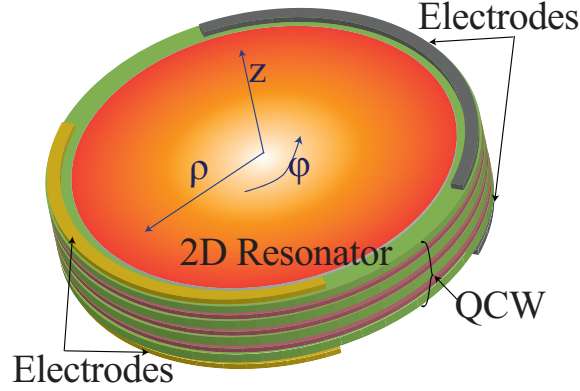


Figure 6.5: Schematic diagram of the spaser design used to compare spasers based on graphene and molybdenum disulfide.

the ability to control free carrier density using ultra-doping makes MoS<sub>2</sub> the material of choice for spaser designs [32]. To evaluate the effectiveness of MoS<sub>2</sub> compared to graphene, a model based on a circular two-dimensional resonator powered *by* a quantum cascade well (QCW) was used to derive performance characteristics.

To analyse the thresholds conditions of spasers based on graphene and MoS<sub>2</sub>, by considering the gain and the plasmon lifetime, necessary conditions for continuous spasing are derived as follows:

$$Q_{\min} = \begin{cases} \frac{e_0^2 E_F \Gamma_{12}}{4\pi\hbar^2 \omega_{\text{sp}} (\omega_{\text{sp}} + i\tau^{-1}) k_0^2 |d_{12}|^2} e^{2k_z \ell}, & \text{for graphene} \\ \frac{[\epsilon_b (\omega_{\text{sp}}^2 + \gamma^2)^2 + \omega_p^2 (\omega_{\text{sp}}^2 - \gamma^2)] \epsilon_0 \Gamma_{12}}{8\hbar (\omega_{\text{sp}}^2 + \gamma^2)^2 k_z k_0^2 |d_{12}|^2} e^{2k_z \ell}, & \text{for MoS}_2 \end{cases} \quad (6.12)$$

where,  $k_0$ ,  $E_F$ ,  $\tau$ ,  $\omega_p$ ,  $\gamma$ ,  $\omega_{\text{sp}}$ ,  $d_{12}$  and  $\ell$  are the effective Fermi vector of the active medium, Fermi energy of the graphene sheet, relaxation time of the carrier of graphene, plasma wavelength of MoS<sub>2</sub>, decay rate of MoS<sub>2</sub> carriers SP wavelength, dipole matrix element of transition from the first excited state to ground state of the gain medium and characteristics distance between the active medium and the two-dimensional resonator respectively.

The proposed design is compared to a similar spaser design made of a circular graphene resonator by means of the SP mode energy, the electric field intensity, the Q-factor and

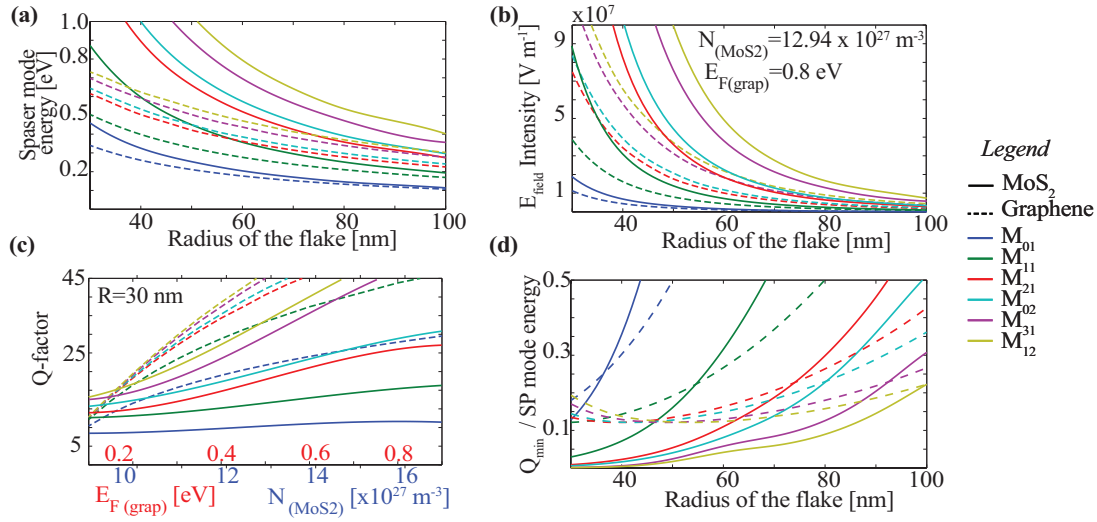


Figure 6.6: **(a)** Spaser mode energy comparison between MoS<sub>2</sub> (continuous lines) and graphene (dashed lines) resonators with respect to radius of the resonator. **(b)** Electric field output ratio ( $E_{np(\text{MoS}_2)} / E_{np(\text{graphene})}$ ) of the MoS<sub>2</sub> and graphene resonators. **(c)** Threshold Q-factors ( $Q_{\min}$ ) of both type of resonators (MoS<sub>2</sub> and graphene) normalized to spaser mode energy output versus radius of the resonators. **(d)** Minimum threshold Q ( $Q_{\min}$ ) of the MoS<sub>2</sub> and the graphene resonators normalized to their output spaser mode energy output versus radius of the resonators.

the operating thresholds. From Figure 6.6(a), demonstrates that the spaser mode energies of the first six modes of the MoS<sub>2</sub> based resonator (continuous lines) are always higher than those of the graphene resonator (dashed lines). The graphene resonator can work at Mid-IR to Near-IR wavelengths and the MoS<sub>2</sub> resonator can work in a wider and higher energy range than the graphene resonator, from Mid-IR to the visible wavelengths. In addition to the spaser mode energy, the Figure 6.6(b) illustrates the electric field outputs of the MoS<sub>2</sub> and graphene resonators ( $E_{np(\text{MoS}_2)}$  and  $E_{np(\text{graphene})}$ ). The proposed design made of MoS<sub>2</sub> provides electric field intensity output that is 12 times larger than that of the graphene resonator for the lowest energy mode. Higher energy mode provides an electric field output that is 100 times ( $\times 100$ ) large. The Q-factors of the two resonators are shown in Figure 6.6(c) and the graphene resonator provides slightly higher Q than MoS<sub>2</sub> resonator due to the massive electrons accommodated in MoS<sub>2</sub> and the lower carrier mobility [32, 144]. Finally, Figure 6.6(d) shows the minimum threshold Q ( $Q_{\min}$ ) of the MoS<sub>2</sub> and the graphene resonators normalized to their output spaser mode energy output. For smaller resonator radius, ranging from 30 nm to 40 nm, Figure 6.6(d) illustrates that the proposed design requires less threshold than graphene spaser. Higher modes require

lower threshold compared to graphene for a higher radius of up to 95 nm. Therefore, the proposed design provides efficient output compared to graphene due to the properties of the MoS<sub>2</sub> resonator.

## 6.4 Summary

A detailed comprehensive analysis of a spaser made of a circular molybdenum disulfide (MoS<sub>2</sub>) resonator powered by an optically pumped QD ring is described. Within the model, an  $n$ -level quantum system is considered, including plasmonic and gain systems. In addition, degeneracy modes of the design are considered. The Hamiltonian, density matrix and motion equations of the spaser, SP mode patterns, output spaser mode energy, electric field intensity, plasmon excitation rate, Q-factor and operating thresholds of the proposed design are comprehensively analysed and compared to similar existing designs. The proposed design has a higher Q-factor than current spaser designs. Furthermore, the device supports higher mode energies (up to 1.60 eV), and can achieve electric field intensities up to  $15 \times 10^8 \text{ Vm}^{-1}$  and higher plasmon excitation rates with fewer critical dimensions due to the properties of the MoS<sub>2</sub> resonator. Thermal and mechanical stability are additional advantages of the proposed model and the device can be fabricated with existing technologies. Using the analysis, the optimum parameters to consider when designing a spaser in a particular application to obtain an effective output can be determined. Since this device produces efficient outputs, the proposed device has numerous potential real world applications that are but not limited to nano-lithography, nano-scopy, nano-sensing, ultra-dense and ultra-fast information storage, nano-optoelectronics, and biomedicine.



# Chapter 7

## Design guidelines of spasers and applications

**D**ESIGN considerations of spasers are entirely based on their application. Depending on the application, a spaser can be tuned in terms of Surface Plasmon (SP) mode energy, electric field output, the Q-factor, the number of SPs generated and the SP generation rate. The design consideration of spaser components are described in this chapter. In addition, this chapter provides a set of comprehensive guidelines on how to tune spasers and describes their applications.

### 7.1 Spaser design guidelines

#### 7.1.1 Designing the components of a spaser

##### 7.1.1.1 Resonator

In contrast to the operation of a laser, a spaser, cavity is replaced by a nano-resonator. The resonator must support SPs and should satisfy conditions to generate SPs on it. Materials of interest are Gold, Silver, Graphene, Molybdenum Disulfide and Plasmene (Artificial graphene). Nano-resonators made of Gold and Silver are the most commonly used resonators for spaser applications. Due to the limitations of tunability, two-dimensional plasmonic materials such as graphene and MoS<sub>2</sub> have received increased attention in spaser designs. Their plasmonic properties has made them the top contenders for spaser applications. The two-dimensional nature and the ease of tunability of SP resonance of

those materials add significant value to these materials. As described in previous chapters, a resonator with finite dimensions supports a set of localized plasmon modes. The resonator size must vary in the range of tens of nanometres to hundreds of nanometres. This size must avoid the non-local effects of the resonator. Non-local effects typically occurs when the size of the resonator becomes smaller than a few nanometres ( $\leq 10$  nm). Therefore, it is safe to have a resonator size larger than 10 nm. A plasmonic resonator can be tuned to operate in different SP mode energies by carefully changing the geometrical parameters of the resonator. How to tune the resonator to achieve a particular electric field amplitude is described below [145–150].

Table 7.1: Table of tunability of spaser mode energy with respect to its resonator type.

Material	Shape	SP Mode Energy (eV)	Tuning Parameter
<b>MLG</b>	Circle	0.5 eV - 1.6 eV MIR-NIR	Flake radius (30 nm-100 nm) Doping Level
	Square	0.1 eV - 1.5 eV MIR-NIR	Length, Width (50 nm-200 nm) Doping Level
<b>BLG</b>	Circle	0.06 eV - 0.6 eV MIR-NIR	Flake radius (30 nm-100 nm) Doping Level
<b>MoS<sub>2</sub></b>	Circle	0.1 eV - 2.3 eV MIR-Visible	Flake radius (30 nm-100 nm) Doping Level
<b>Silver</b>	Sphere	1.4 eV - 3.0 eV NIR-Visible	Radius
	Cube	2.5 eV - 3.0 eV Visible	Length, Width, Height
	Rectangular Prism	1.38 eV - 3.1 eV NIR-Visible	Width, Length
	Shell	2.4 eV - 3.5 eV Visible	Radius, Shell Thickness
<b>Gold</b>	Sphere	1.4 eV - 2.5 eV NIR-Visible	Radius
	Cube	2.0 eV - 2.5 eV Visible	Length, Width, Height
	Gold	1.3 eV - 1.8 eV NIR	Radius, Length
	Shell	1.0 eV - 2.4 eV NIR-Visible	Radius, Shell Thickness

Doping can be introduced to graphene and MoS<sub>2</sub> electrically or electrochemically. A common method for doping MoS<sub>2</sub> is Li-intercalation which involves inserting Li ions in between MoS<sub>2</sub> layers to enhance the carrier concentration of the MoS<sub>2</sub> flake. However, more time is required to achieve a uniformly doped MoS<sub>2</sub> flake using Li-intercalation compared to the electrical gating method. According to the table 7.1, SP output mode energy can be varied by changing the radius of the flake. Thus, flake dimensions play a large role in plasmon resonance.

### 7.1.1.2 Active medium / gain system

Active medium provides energy non-radiatively to the plasmonic resonator for generating coherent SPs. Quantum dots, earth ions, dye molecules and quantum wells are of interest for use as the gain medium of spasers. Likewise, for the resonator, choice of active medium depends its application, SP mode energy, and type of material (threshold gain). Moreover, quantum well emissions are based on interband transitions and quantum cascade well emissions are based on intersubband transitions. Electron reusability is an advantage of using quantum cascade wells instead of typical quantum wells. Instead of varying the material similar to quantum wells, the emission wavelength of a quantum cascade well can be varied by changing the thickness of the layers. However, emission wavelengths of quantum cascade wells are limited in to IR wavelengths due to the limitations imposed on intersubband transitions. If someone requires emissions in the visible region, then a typical quantum well or other type of active mediums such as quantum dots can be used. The emission wavelength of quantum dots can be tailored by varying the size of the quantum dot. The details of the commonly used active mediums and their tuning parameters are provided in the Table 7.2 [151–159].

### 7.1.1.3 Pump

There are two pumping methods as described in previous chapters: electrical pumping and optical pumping. The most commonly used method is optical pumping. This thesis describes three optically pumped spaser designs and an electrically pumped spaser

and the pumping method depends on the active medium used. The quantum well and quantum cascade well can be pumped electrically via quantum nano-wires. In addition, quantum dots, earth-ions and dye molecules can be optically pumped using a laser that matches the absorption spectrum of the active medium. A VCSEL was introduced to provide pumping to the system due to its critical dimensions and output characteristics such as the shape of the beam and power output. It also provides accessibility to operate spaser as an SP modulator.

Table 7.2: Table of tunability of emission spectrum with respect to its active medium.

<b>Gain Medium</b>	<b>Absorption Spectrum</b>	<b>Emission Spectrum</b>	<b>Tuning Parameter</b>
<b>Quantum Well</b>	0.2 eV -3.3 eV IR-Visible	0.1 eV - 3.2 eV IR-Visible	Material
<b>Quantum Cascade Well</b>	0.1 eV -1.3 eV IR-Visible	0.05 eV - 1.2 eV IR-Visible	Layer Thickness Material
<b>Quantum Dots</b>			
InAs	1.1 eV -1.7 eV NIR	0.9 eV - 1.5 eV NIR	Size
CdSe	1.9 eV -3.0 eV Visible	1.7 eV - 2.7 eV Visible	Size
CdS	3.0 eV -4.5 eV Visible	2.5 eV - 4.2 eV Visible	Size
CdTe / CdSe	1.7 eV -2.3 eV Visible	1.4 eV - 1.9 eV NIR-Visible	Size Shell Thickness
<b>Earth-ions</b>	0.8 eV -4.5 eV NIR-Visible	0.9 eV - 3.0 eV NIR - Visible	Compound
<b>Dye-Molecules</b>	0.8 eV -4.5 eV NIR-Visible	0.6 eV - 4.0 eV NIR - Visible	Compound
<b>Carbon Nanotube</b>	1.0 eV -2.5 eV NIR-Visible	0.5 eV - 1.5 eV NIR	Chirality

## 7.1.2 Operational Characteristics

### 7.1.2.1 Q-Factor

The Q-factor of a resonator is an important characteristic of a spaser. Losses associated with the plasmonic resonator are inversely proportional to the Q-factor of the resonator. Therefore, a higher Q-factor indicates fewer losses which enables the device to work at

lower power levels, increasing its efficiency. Therefore, it is essential to achieve highest possible Q-factor to improve performance. The equation for the Q factor is defined as:

$$Q = \frac{\omega_{sp}}{2\gamma_{sp}} \quad (7.1)$$

where,  $\gamma_{sp}$  is the plasmon decay rate with the following form:

$$\gamma_{sp} = \frac{\text{Im}(\epsilon_m(\omega))}{\text{Re}\left(\frac{d\epsilon_m(\omega)}{d\omega}\right)} \quad (7.2)$$

Considering equations 7.1 and 7.2, to achieve a high Q-factor, a material with a low imaginary component for complex permittivity should be used as the plasmonic resonator. Due to the high mobility of graphene carriers, graphene resonators provide higher Q-factors and due to slower mobility of the massive electrons accommodated in MoS<sub>2</sub>, MoS<sub>2</sub> has a slightly lower Q-factor than graphene.

### 7.1.2.2 Threshold gain

Threshold gain is the minimum gain required for the existence of plasmons on the resonator surface. To minimize threshold gain, correct choice of material is essential. Due to the properties such as high electron mobility, graphene requires less threshold gain than other materials described in this thesis. The threshold gain of a resonator can be obtained from the following equation.

$$g_{th} = \frac{\omega}{c\sqrt{\epsilon_d}} \frac{\text{Re}[s(\omega)]}{1 - \text{Re}[s(\omega)]} \text{Im}[\epsilon(\omega)] \quad (7.3)$$

According to equation 7.3, the threshold gain depends entirely on the plasmonic material. The imaginary component of the materials' complex permittivity should be smaller than the real component to achieve a lower threshold gain.

### 7.1.2.3 Electric field amplitude

The electric field amplitude of the resonator is based on the size of the resonator and the doping level. Resonators that support higher mode energies provides higher electric fields and require a higher gain. Increasing the doping level can achieve higher electric field output. This can be managed according to the application as a high electric field output requires many SPs produced per mode, which requires a higher gain.

### 7.1.2.4 Rate of surface plasmon generation

The number of SPs generated per unit time depends on the interaction between the gain medium and the plasmonic nano-resonator. This relationship can be obtained from equation 7.4

$$\mathfrak{R}_{pl,k} = \alpha \omega_{sp}^2 \frac{\gamma_{2p}}{\gamma_{2p}^2 + (\omega_{12} - \omega_{sp})^2} |d_{13}^{(L)}|^2 \sum_{j=4}^n |d_{12}^{(K),j}|^2 . \quad (7.4)$$

According to this equation, the SP generation rate primarily depends on the coupling between the gain subsystem and the plasmonic subsystems.  $d_{12}^{(K),j}$  is the dipole matrix element that corresponds to the transition from the first excited state to the ground state. A careful design should be considered to make the  $d_{12}^{(K),j}$  a real quantity.  $d_{13}^{(L)}$  corresponds to the energy transition from the pumping source to the gain element. The SP generation rate can be increased by improving the coupling between the pumping source and the gain element, which can be achieved through careful selection of pumping sources and gain elements. The details to select materials to make spasers are provided in the previous section of this chapter.

## 7.2 Applications of spasers

As described in previous chapters, a spaser is a non-diffraction limited setup with critical dimensions that are smaller than one micron, and the output is intense, coherent, and tightly localized. Therefore, a spaser is a promising device that can be used in numerous real world applications [160–165]. A spaser can be operated in two regimes: CW and

dynamic. The mode of selection depends on the application as described in following sections.

### **7.2.1 Continuous wave operation (CW mode)**

When a spaser operates in CW mode, it provides coherent and intense output. Therefore, it can be used for applications in nano-lithography and nano-scopy as well as in on-chip circuits such as an SP source (*i.e.* quantum computing, lab-on-a-chip concept).

#### **7.2.1.1 Nano-lithography**

Nano-lithography [166–169] is a major branch in nano-scale fabrication process, meaning the structures with at least one critical dimension are between 1 nm - 100 nm. However, due to the bulky nature of lasers, spasers have become the top contender for lasers and a better alternative to bulky designs made of lasers. The characteristics of two-dimensional resonator based spasers match the requirements. The proposed spaser described in this thesis provides higher outputs in terms of the electric field, SP mode energy, Q-Factor, and number of SPs compared to existing models. Therefore, these designs are ideal for nano-lithography.

#### **7.2.1.2 Nano-Scopy**

Nano-scopy [170–175] is fast growing technique for imaging ultra-small structures of a nanometre scale [176]. The necessity of a highly localized device was the initial problem that can be overcome with the application of spasers.

#### **7.2.1.3 Lab-on-a-chip**

Lab-on-a-chip is a concept that has received increasing attention over the past ten years due to the technological development of nano-scale fabrication and non-diffraction limited assemblies [177–182]. This concept has primarily been considered for biomedical applications. In most of the cases, for imaging purposes, a nano-scale coherent light or

SP source is required, which can be achieved using a spaser. Due to their high tuning capabilities, two-dimensional resonator based spasers have a large impact on the performance of the device and its applicability in these applications. The output characteristics and the circular shape of the design improve the applicability of the proposed spasers due to the ease of coupling them with other nano-circuitries.

#### **7.2.1.4 Quantum computing**

The field of quantum computing [183–189] has emerged quickly over the past two decades. This process requires nano-optical sources, amplifiers, modulators and switches since optical devices work faster than the electronic designs. Laser is the optical counterpart to the transistor operation in electronics. However, the laser has critical dimensions that are larger than a few microns ( $> 5 \mu\text{m}$ ) and the system becomes bulky. A possible alternative is the use of spasers instead of lasers. Although, the packing density of square resonators is high, circular resonators provide higher and more efficient output than the square shape. Therefore, circular two-dimensional spasers would have a large impact on the creation of quantum computers.

#### **7.2.2 Spaser as an amplifier**

Chapter 5 shows that the spaser work as an SP amplifier and is a loss compensator. Due to the Joule losses associated with the propagation of SP fields are being disturbed. Therefore, to achieve continuous operation, gain must be introduced in to the system with a spaser. Thus, spasers can be used in association with SP waveguides to overcome losses. Although, this process is energy consuming, the ultra-fast behaviour and small critical dimensions compensate for that drawback. Optically or electrically pumped spasers can be placed over the SP waveguide to achieve seamless operation.

Since the spaser is the nano-plasmonic counterpart of the laser, the operation of transistors can be replaced by spasers which require smaller critical dimensions than lasers.

Therefore, the application of spasers as amplifiers is essential to creating ultra-fast, ultra-thin nano-optical circuits.

### 7.2.3 Spaser as a modulator

Recent research have shown that two-dimensional materials such as graphene and MoS<sub>2</sub> are ideal for designing SP waveguides [190–195]. However, to transmit data over waveguides, electronic waves must be transformed to an SP form. This study demonstrates the ultra-fast dynamics of the spaser and the applicability of two-dimensional spasers as modulators (Pulsed / Sine wave). In addition to the modulation response, the two-dimensional nature and shape of the designs make them easy to incorporate with other plasmonic nano devices.

### 7.2.4 Applications in bio-medicine

Common methods of destroying cancer cells are radiotherapy and chemotherapy [196–199]. However, due to localisation problems, it is difficult to target cancer cells, while avoiding healthy cells. Thus, in addition the cancer cells, healthy and important cells in the vicinity are destroyed during this process (highly critical in brain tumors). Therefore, the method is inefficient. Not having a proper alternative is the main reason to continue this method to destroy cancer cells. The development of an effective technique to treat cancers is one of the major challenges that medical researchers have faced.

A spaser is a device that can provide a tightly concentrated electric field in the form of localised surface plasmons. Spasers provide coherent oscillations of free surface electrons and the use of plasmonic photothermal cancer therapy is described in the references [200,201]. The proposed designs in this research are small (30 nm to 100 nm) and are ideal energy sources. Since body cell sizes range from 1 micron to 100 microns. 10 - 100 spasers can be used to cover a single cell. Moreover, due to the highly localised nature of the spasers, the precise cancer cell can be targeted. Due to recent advances in biomedical engineering, it is also possible to target cancer cells (using a drug delivery

method). The largest problem has been designing a non-toxic, organic spaser assembly. The use of heavy plasmonic metals can have strong effects on the body and all existing two-dimensional designs require doped resonators to achieve SPs on the resonator. Therefore, the proposed un-doped graphene based spaser (described in the Section 5.3) can be used as an optimal alternative to cancer therapies, such as chemotherapy and radiotherapy.

The proposed spaser designs based on un-doped graphene can generate surface plasmons in the infra-red wavelengths and provide higher electric fields, making the setup more compatible than existing spaser designs. Un-doped graphene based spaser supports electric field amplitudes higher than  $11 \times 10^8$  V/m and can be tuned over a wide range, varying from 0.1 eV to 0.62 eV. In the proposed method of treatment, a cluster of un-doped graphene based spasers must be placed around the cancer cells and then the cancer cells can be damaged by providing energy to the spasers. For continuous operation of these spasers, they must be pumped externally via a pumping source. Since, the design operates in infra-red wavelengths, these spasers can be pumped externally via pump lasers which can be penetrated through the body, making the process harmless to the human body. The photons provided by the laser pump will then be absorbed by the active medium of the spaser and the active medium will provide energy continuously to the plasmonic nano-resonator to generate surface plasmons. In contrast to existing spaser designs, the proposed spaser design provides tightly localised and coherent surface plasmons due to the inherent properties of graphene. The tight localisation of the design and optimum external energy pumping, which is much smaller than current illumination powers used in existing photothermal therapies, make it possible to generate coherent, high, and tightly concentrated electric fields on spasers, causing selective destruction of the cancer cells [201–205].

## Chapter 8

# Conclusions and future work

**D**UE to recent advances in the area of nano-electronics and studies on configurations which are not limited by the diffraction limit, such as spasers, it is possible to design ultra-thin, ultra-fast and efficient nanocircuits.

This chapter concludes this thesis by providing a summary of major findings and the contributions made to the area of spasers throughout the author's PhD. This chapter also provides suggestions for future research as extensions of the current study.

### 8.1 Summary of contributions

With recent advances in the study of nano-scale optoelectronic circuits in the field of plasmonics and numerous applications, the development of new design paths, theoretical models, and guidelines for optimising and engineering the designs are of interest in various research disciplines. This could stimulate the practical realisation of new plasmonic nano-circuits, making them easily customisable and tunable for delivering optimal performances in diverse applications. This thesis presents a comprehensive study on the design, modelling, and characterisation of active nanoplasmonic sources, particularly spasers made of two dimensional materials, such as graphene and molybdenum disulfide. In addition, innovative design considerations for increasing the output and tunability are provided and discussed.

The findings of this research contribute to the existing knowledge on spasers in three significant ways: deriving a quantum mechanical framework for analysing two-dimensional resonator based spaser configurations, conducting a detailed analysis of different spaser configurations made of two-dimensional plasmonic materials to achieve higher and more efficient outputs. (including the work of pioneering a spaser based on molybdenum disulfide, and providing a comprehensive set of guidelines to design and optimise spasers.

Pioneering a spaser design based on  $\text{MoS}_2$  is one of the significant achievements of this research because there are many spaser designs based on graphene, but, the work explained in the Chapter 6 is the first spaser design made with a  $\text{MoS}_2$  resonator. This work also extends the applicability of  $\text{MoS}_2$  to active plasmonic devices. Moreover, the proposed design has paved the way towards many potential real-world applications based on  $\text{MoS}_2$  with improved output characteristics compared to existing spaser designs based on noble metals and graphene.

A summary of the contributions and findings to fulfill the research aims and objectives of this thesis is presented below:

**Implementing a quantum mechanical framework to analyse a two dimensional, nano-resonator based spaser design.**

Chapter 3 and Chapter 4 provide a framework by combining a quantum mechanical model and a semi-classical model. The quantum mechanical model is used to analyse the gain subsystem and the interaction between the gain system and the plasmonic subsystems of a spaser and the plasmonic subsystem is analysed using a semi-classical approach. This model can be used to analyse two dimensional resonator based spasers in different operating modes, such as continuous wave operation and dynamic operation. The spaser's mode energy, electric field amplitude, Q-factor, threshold gain, and surface plasmon generation rate can be analysed under the steady state operation of the spaser. This framework can also be used to analyse variations of the number of surface plasmons

generated per spasing mode, population inversion of the gain system, amplifier response and modulated responses of a spaser.

**Developing and analysing the continuous wave operation of an electrically pumped, quantum cascade well powered, mono-layer graphene based spaser.**

First section of Chapter 5 provides a detailed analysis of a circular, shaped mono-layer graphene (MLG) based spaser. The proposed design is an electrically pumped quantum cascade well powered, circular MLG nano-resonator-based spaser. Due to the properties of MLG and the quantum cascade well, the proposed design has higher mechanical and thermal stability which are the most important characteristics of nanoscale designs. This circular nano-resonator-based spaser supports tightly localised plasmon modes due to its geometry and the materials used. It also provides intense and coherent SP output since stimulated emission occurs in the system. The design supports a set of localised SP modes with higher energies and a higher electric field, and Q-factor; it requires less threshold gain compared to existing spasers based on noble metals. The spaser can be tuned over a wide range of wavelengths, varying from Mid-IR to Near-IR. The proposed spaser can be used to generate electric field amplitudes as high as  $35 \times 10^7$  V/m. In addition, the resonator of the spaser can generate plasmons with higher quality factors (e.g. 80). Due to these efficient and effective outputs, the proposed spaser design can be integrated into many plasmonic nano-circuits. This work is reported in the "Journal of Applied Physics" (2015)

**Modelling and studying a quantum dots powered, optically pumped, circular, mono-layer graphene spaser.**

A spaser can be used as a coherent plasmonic source, as well as an SP amplifier and an SP modulator. To determine the applicability of graphene based spasers as an amplifier or modulator, an analysis was conducted as described in the second section of Chapter 5. The system is analysed to determine the number of surface plasmons generated per spasing mode and the population inversion of the gain system under several conditions. Under the steady state condition, this system generates many SPs, ( $\sim 900$ ) when

the system is pumped by a laser with  $8 \times 10^{12} \text{ s}^{-1}$ . This value is large compared to the small mode volume of the design. This design can only be used as an amplifier for a short time ( $< 250 \text{ fs}$ ) due to the inherent strong feedback of the spaser as described in this chapter. The proposed design also can be applied as pulse amplitude to the time delay modulator. Thus, this spaser can be used to develop ultra-fast, ultra-thin optical devices.

### **Realising a VCSEL pumped spaser based on un-doped bi-layer graphene (BLG).**

The applicability of MLG based spasers in biomedical applications is declining due to the requirement of doping to achieve plasmon resonance at IR wavelengths. Therefore, existing MLG based spasers have less compatibility within biomedical applications, such as cancer treatments. It is possible to achieve plasmon resonance at IR- wavelengths using un-doped graphene, which is highly useful in biomedicine, due to the ability of generating plasmons in un-doped condition of bi-layer graphene. The proposed spaser geometry consists of quantum dots that can be pumped optically and the design was analysed using the frameworks described in Chapter 4. This device was also analysed in both of the operational regimes (continuous wave and dynamic) and the results are described. According to the results, this device provides higher electric fields and SPs than MLG, but BLG supports lower mode energies than MLG. These spasers can be used to damage cancer cells as an alternative to chemotherapy. Chemotherapy may damage nearby healthy cells that are in the close proximity to the cancer cells. A group of spasers can be used to damage the cancer cells selectively; they can be pumped externally from a pump laser, such that only the malignant cells are destroyed. Therefore, BLG-based spasers have many potential real-world applications in the area of biomedicine

**Designing and analysing the characteristics of a molybdenum disulfide nano-resonator-based, two-dimensional spaser.**

A spaser made with an MoS<sub>2</sub> nano-resonator is analysed and described in Chapter 6. This study is the first analysis of a spaser based on MoS<sub>2</sub> to date. The proposed design supports higher spaser mode energies varying from Mid-IR to the visible wavelengths and provides higher electric field amplitudes than graphene-based devices. The layer separation in MoS<sub>2</sub> accommodates more carriers and can achieve higher carrier densities. Therefore, the system supports higher outputs. In addition, MoS<sub>2</sub> accommodate massive electrons unlike graphene, thus its electron mobility is lower than that of graphene. Therefore, spasers made of MoS<sub>2</sub> nano-resonators consume more power and provide plasmons with a slightly lower Q-factor than graphene nano-resonators. This work is reported in the “Journal of Applied Physics”.

**Providing comprehensive guidelines to design and optimise spasers.**

Chapter 7 provides a comprehensive set of guidelines for designing and optimising spasers. It is a collection of the data from the results obtained in this research and the details provided in the related literature. The discussion provides details for selecting appropriate resonators considering the material, shape, tune relevant parameters, and input / output characteristics. It also explains how to form active mediums depending on design considerations. The methods for obtaining efficient outputs and how to tune these parameters are also discussed. A designer can find most of the necessary design parameters to create a spaser for a particular application.

The findings of this research have expanded the applications of spasers in many ways. For example, the proposed designs can be easily integrated into on-chip circuits and can interconnect with most of the existing optical devices due to their shape. Bi-layer graphene-based un-doped spasers can be used as an alternative to chemotherapy, for many other biomedical applications. Moreover, the derived framework and guidelines can be used to analyse the performance and develop many spaser designs based on two-dimensional plasmonic nano-resonators, making the outcomes of this research more use-

ful.

## 8.2 Suggestions for future research

This work can be extended through many pathways, some of which are described below;

### **a) Extending the study to analyse the effect of multiple active elements of a spaser configuration.**

All the analyses were conducted considering the interaction of a single active element of the gain medium with the plasmonic nano-resonators. The total interaction was found by taking the superposition of individual interactions which is a safe assumption in laser physics. However, an analysis can be done to analyse the interaction among the resonator and the gain element, in addition to the interactions with the gain elements in the active medium. Then, the effects of multiple active mediums can be analysed, in order to improve the accuracy of the current physical model.

### **b) A comprehensive analysis of the performance of a group of two-dimensional resonator based spasers.**

In this analysis, all the designs are analysed individually. Yet an analysis of the collective operation of a group of spasers is essential when applying spasers to biomedical applications (as an alternative to the chemotherapy) and to nanoplasmonic circuits. Then the gain medium - gain medium, nano-resonator - nano-resonator and nano-resonator - gain medium interactions must be considered. Researchers have shown that the collective operation of spasers provides " $\times N^2$ " output and not " $\times N$ " output. These designs can also be used to achieve super-radiance.

### **c) Realising single plasmon generation**

This study analyses the number of surface plasmons generated per spasing mode. These designs can be carefully tailored to achieve more SPs or fewer SPs. In such case can be used to develop a system which can generate a single plasmon which can be used in applications, such as quantum counting systems and tomography [206–208]

**d) Analysing the performance of spasers generates propagating surface plasmons.**

Localised plasmon modes of the resonators are considered in this analysis. However, an analysis can be done to analyse the performance of a spaser based on surface plasmon polaritons (SPP). A shape such as a nano-ribbon could provide better output characteristics in contrast to the existing two-dimensional spaser designs. It could also create more potential applications for the spasers, such as compensating for losses associated with plasmonic waveguides.

**e) Designing and analysing spasers made of other two-dimensional plasmonic materials.**

Other than  $\text{MoS}_2$ , black phosphorus is one of the top contenders for replacing graphene. Therefore, this analysis can be extended to study the performance of new plasmonic nano-resonators made of different two-dimensional plasmonic materials, such as black phosphorus, plasmene (an artificial graphene made of gold nano particles).

# Abbreviations

BLG	Bi-Layer Graphene
CNT	Carbon Nanotube
CW	Continuous Wave
DOS	Density of States
e-h pair	electron-hole pair
GNF	Graphene Nanoflake
IR	Infrared
Laser	Light Amplification by Stimulated Emission of Radiation
LSP	Localized Surface Plasmons
LOQC	Linear Optics Quantum Computing
LSP	Localized Surface Plasmon Resonance
MIR	Mid Infrared
MLG	Mono-Layer Graphene
NIR	Near Infrared
NP	Nanoparticle
QD	Quantum Dot
QED	Quantum Electrodynamics
QW	Quantum Well
SP	Surface Plasmon
Spaser	Surface Plasmon Amplification by Stimulated Emission of Radiation
SPP	Surface Plasmon Polaritons
SPR	Surface Plasmon Resonance
TLS	Two Level System
VCSEL	Vertical Cavity Surface Emitting Laser

# Appendix A

## Resonator wavelengths

### A.1 Resonance wavelengths of circular graphene resonators

Table A.1: Table of resonance wavelengths of circular shaped monolayer graphene with respect to its radius when the doping level is 0.8 eV.

Resonator Radius (nm)	Mode wavelengths (nm)					
	M01	M11	M21	M02 667	M31	M12
10	1683	1229	784	667	453	337
15	2111	1624	1353	1269	1071	923
20	2592	1887	1616	1555	1422	1321
25	3109	2165	1812	1745	1619	1539
30	3645	2466	2013	1926	1778	1692
35	4192	2783	2227	2120	1936	1834
40	4745	3111	2452	2324	2103	1980
45	5303	3445	2687	2538	2278	2134
50	5863	3785	2928	2759	2462	2295
55	6426	4129	3175	2985	2650	2461
60	6991	4475	3425	3215	2843	2633
65	7557	4823	3678	3448	3040	2808
70	8124	5173	3933	3684	3240	2986
75	8691	5524	4190	3921	3441	3167
80	9260	5876	4449	4160	3645	3350
85	9829	6230	4708	4400	3850	3534
90	10398	6583	4969	4641	4056	3720
95	10968	6938	5230	4884	4264	3906
100	11538	7293	5492	5126	4472	4094

Table A.2: Table of resonance wavelengths of circular shaped monolayer graphene with respect to its Fermi level when the radius is 30 nm.

Fermi level (eV)	Mode wavelengths (nm)					
	M01	M11	M21	M02	M31	M12
0.10	11389	9796	9464	9416	9334	9284
0.15	8653	6980	6570	6509	6412	6356
0.20	7252	5598	5143	5074	4963	4902
0.25	6382	4778	4298	4222	4101	4035
0.30	5781	4232	3741	3660	3531	3460
0.35	5335	3840	3345	3262	3127	3053
0.40	4990	3545	3050	2965	2825	2748
0.45	4712	3313	2821	2735	2592	2513
0.50	4484	3125	2638	2551	2405	2325
0.55	4291	2969	2488	2401	2253	2171
0.60	4126	2838	2362	2275	2127	2044
0.65	3983	2726	2255	2168	2020	1936
0.70	3857	2628	2164	2077	1928	1843
0.75	3745	2542	2083	1997	1848	1763
0.80	3645	2466	2013	1927	1778	1692
0.85	3555	2398	1950	1865	1716	1630
0.90	3474	2337	1894	1809	1660	1574

## A.2 Resonance wavelengths of circular shaped bi-layer graphene (BLG) resonators

Table A.3: Table of resonance wavelengths of circular shaped bi-layer graphene with respect to its radius when the Fermi level  $E_f = 0.0$  eV.

Flake Radius (nm)	Mode wavelengths (nm)					
	M01	M11	M21	M02	M31	M12
30	4440	2968	2398	2293	2117	2026
40	5806	3777	2952	2791	2512	2359
50	7190	4618	3551	3338	2964	2754
60	8583	5474	4171	3910	3445	3180
70	9981	6339	4804	4494	3941	3624
80	11382	7209	5444	5086	4446	4078
90	12786	8083	6088	5683	4957	4539
100	14191	8959	6736	6284	5473	5005

Table A.4: Table of resonance wavelengths of circular shaped bi-layer graphene with respect to its radius when the Fermi level  $E_f = 0.2$  eV.

Flake Radius (nm)	Mode wavelengths (nm)					
	M01	M11	M21	M02	M31	M12
30	4325	2883	2323	2218	2044	1953
40	5659	3676	2868	2710	2435	2284
50	7010	4498	3455	3247	2880	2674
60	8369	5335	4062	3806	3351	3092
70	9734	6180	4680	4377	3836	3526
80	11101	7029	5305	4955	4330	3971
90	12471	7882	5934	5539	4830	4421
100	13842	8737	6567	6125	5334	4876

Table A.5: Table of resonance wavelengths of circular shaped bi-layer graphene with respect to its radius when the Fermi level  $E_f = 0.4$  eV.

Flake Radius (nm)	Mode wavelengths (nm)					
	M01	M11	M21	M02	M31	M12
30	4003	2652	2119	2019	1849	1759
40	5247	3396	2637	2487	2227	2082
50	6506	4165	3189	2994	2648	2453
60	7772	4946	3757	3518	3091	2848
70	9041	5733	4335	4052	3546	3256
80	10313	6524	4918	4592	4008	3672
90	11587	7318	5504	5136	4475	4093
100	12861	8113	6094	5682	4945	4518

### A.3 Resonance wavelengths of circular MoS<sub>2</sub> resonators

Table A.6: Table of resonance wavelengths of circular shaped monolayer graphene with respect to its radius when the carrier concentration is  $8.84 \times 10^{27} \text{ m}^{-3}$ .

Resonator Radius (nm)	Mode wavelengths (nm)					
	M01	M11	M21	M02	M31	M12
40	5089	3463	2897	2817	2760	2671
50	6227	4119	3293	3141	2903	2802
60	7380	4811	3763	3560	3215	3034
70	8541	5518	4265	4017	3583	3344
80	8834	6235	4782	4491	3978	3689
90	10876	6958	5309	4977	4387	4051
100	12047	7684	5841	5469	4804	4424

Table A.7: Table of resonance wavelengths of circular shaped monolayer graphene with respect to its radius when the carrier concentration is  $16.85 \times 10^{27} \text{ m}^{-3}$ .

Resonator Radius (nm)	Mode wavelengths (nm)					
	M01	M11	M21	M02	M31	M12
30	2701	1422	921	838	654	556
40	3819	2078	1387	1241	1004	868
50	4898	2759	1879	1691	1383	1202
60	6074	3478	2388	2161	1785	1563
70	7258	4200	2917	2652	2198	1933
80	8507	4941	3468	3176	2630	2318
90	9580	5654	3929	3662	3114	2642
100	10902	6413	4530	4190	3484	3087

# Appendix B

## Numerical Methods

### Resonant Structures

Three plasmonic structures are considered in this research, namely, Mono-layer graphene (MLG), Bi-layer graphene (BLG) and Molybdenum Disulfide (MoS<sub>2</sub>). In particular, circular shape is considered. All the structures are modelled as disks (three-dimensional (3D) structures). Rather than transmitting energy, those structures are designed to store electromagnetic energy of a particular frequency within a small space. A commercial software, COMSOL Multiphysics is used to analyse these structures explained above. Quantities of interest included the resonant wavelength and the Q-factor. One of the structures considered in this study is shown in Figure B.1

### Adding Physics to the system - COMSOL

Electromagnetic waves - frequency domain analyser is used to analyse the resonant structures described in the previous section. For the time-harmonics and eigenfrequency related problems, the governing equation can be given in the form,

$$\nabla \times (\mu_r^{-1} \nabla \times \mathbf{E}) - k_0^2 \epsilon_{rc} \mathbf{E} = 0 \quad (\text{B.1})$$

Where,  $k_0$  is the wave number of free space and defined as,

$$k_0 = \omega \sqrt{\epsilon_0 \mu_0} = \frac{\omega}{c_0} \quad (\text{B.2})$$

where,  $c_0$  is the speed of light in vacuum.

Considering out-of-plane wave number as  $k_z$ , electric field can be modelled as,

$$\mathbf{E}(x, y, z) = \tilde{\mathbf{E}}(x, y)e^{-ik_z z} \quad (\text{B.3})$$

Thereby, the wave equation can be simplified as,

$$(\nabla - ik_z \mathbf{z}) \times [\mu_r^{-1}(\nabla - ik_z \mathbf{z}) \times \tilde{\mathbf{E}}] - k_0^2 \epsilon_{rc} \tilde{\mathbf{E}} = 0, \quad (\text{B.4})$$

where,  $\mathbf{z}$  is the unit vector towards the z-direction of the coordinate system considered as shown in the figure.

Similarly, due to the 2D symmetry, electric field varies with the azimuthal mode number  $m$  and the equation B.3 can be represented in a form as,

$$\mathbf{E}(r, \phi, z) = \tilde{\mathbf{E}}(r, z)e^{-im\phi}. \quad (\text{B.5})$$

For this case, the wave equation can be simplified as,

$$(\nabla - i\frac{m}{r}\Phi) \times [\mu_r^{-1}(\nabla - i\frac{m}{r}\Phi) \times \tilde{\mathbf{E}}] - k_0^2 \epsilon_{rc} \tilde{\mathbf{E}} = 0, \quad (\text{B.6})$$

where,  $\Phi$  is the unit vector towards  $i\frac{m}{r}\Phi$ -direction of the coordinate system considered.

Then, the system can be solved as an eigenfrequency problem and it provides the complex eigenfrequencies in the form of,

$$\lambda = -i\omega + \delta, \quad (\text{B.7})$$

where,  $\delta$  is the damping of the eigenfrequency. Then the Q-factor can be obtained from the following equation,

$$Q = \frac{\omega}{2|\delta|}. \quad (\text{B.8})$$

### Conductivity models

All the resonator types considered in this study (Mono-layer graphene (MLG), Bi-layer Graphene and Molybdenum disulfide) are modelled by using their conductivity formulas explained in Chapter 4.

**Meshing**

Automatic and semi-automatic meshing tools are available in COMSOL Multiphysics, including free tetrahedral meshing and swept meshing. The default algorithm is automatic tetrahedral meshing for physics defined in solids, and a combination of tetrahedral and boundary-layer meshing for fluids. Here, automatic tetrahedral meshing is used in all the analysis.

**Parametric sweep**

Parametric sweep is used to obtain the values of varying parameters, such as flake radius and its doping level (Fermi level)

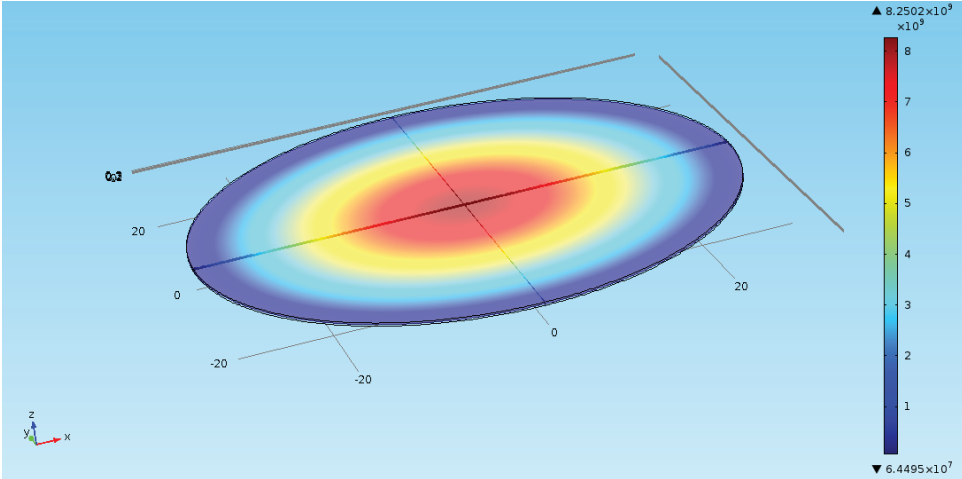


Figure B.1: 2D resonant structure considered in COMSOL Multiphysics.

# Bibliography

- [1] M. Premaratne and G. P. Agrawal, *Light propagation in gain media*. Cambridge University Press, 2011.
- [2] S. A. Maier, *Plasmonics: Fundamentals and Applications: Fundamentals and Applications*. Springer, 2007.
- [3] S. Lal, S. Link, and N. J. Halas, "Nano-optics from sensing to waveguiding," *Nat. Photonics*, vol. 1, no. 11, pp. 641–648, 2007.
- [4] M. R. Feldman, S. C. Esener, C. C. Guest, and S. H. Lee, "Comparison between optical and electrical interconnects based on power and speed considerations," *Appl. Opt.*, vol. 27, no. 9, pp. 1742–1751, May 1988.
- [5] A. Majumdar, J. Kim, J. Vuckovic, and F. Wang, "Graphene for tunable nanophotonic resonators," *Selected Topics in Quantum Electronics, IEEE Journal of*, vol. 20, no. 1, pp. 68–71, Jan 2014.
- [6] D. J. Bergman and M. I. Stockman, "Surface plasmon amplification by stimulated emission of radiation: Quantum generation of coherent surface plasmons in nanosystems," *Phys. Rev. Lett.*, vol. 90, p. 027402, Jan 2003.
- [7] C. Jayasekara, M. Premaratne, M. I. Stockman, and S. D. Gunapala, "Multimode analysis of highly tunable, quantum cascade powered, circular graphene spaser," *J. Appl. Phys.*, vol. 118, no. 17, p. 173101, 2015.
- [8] D. Chang, A. S. Sørensen, P. Hemmer, and M. Lukin, "Quantum optics with surface plasmons," *Physical review letters*, vol. 97, no. 5, p. 053002, 2006.

- [9] A. V. Zayats and I. I. Smolyaninov, "Near-field photonics: surface plasmon polaritons and localized surface plasmons," *Journal of Optics A: Pure and Applied Optics*, vol. 5, no. 4, p. S16, 2003.
- [10] P. Zijlstra, J. W. Chon, and M. Gu, "Five-dimensional optical recording mediated by surface plasmons in gold nanorods," *Nature*, vol. 459, no. 7245, p. 410, 2009.
- [11] G. Nenninger, P. Tobiška, J. Homola, and S. Yee, "Long-range surface plasmons for high-resolution surface plasmon resonance sensors," *Sensors and Actuators B: Chemical*, vol. 74, no. 1, pp. 145–151, 2001.
- [12] B. Liedberg, C. Nylander, and I. Lunström, "Surface plasmon resonance for gas detection and biosensing," *Sensors and actuators*, vol. 4, pp. 299–304, 1983.
- [13] J. Homola, S. S. Yee, and G. Gauglitz, "Surface plasmon resonance sensors: review," *Sensors and Actuators B: Chemical*, vol. 54, no. 1, pp. 3–15, 1999.
- [14] I. H. El-Sayed, X. Huang, and M. A. El-Sayed, "Surface plasmon resonance scattering and absorption of anti-egfr antibody conjugated gold nanoparticles in cancer diagnostics: applications in oral cancer," *Nano letters*, vol. 5, no. 5, pp. 829–834, 2005.
- [15] H. Raether, *Surface plasmons on smooth and rough surfaces and on gratings*. Springer, 2006, vol. 111.
- [16] S. K. Ghosh and T. Pal, "Interparticle coupling effect on the surface plasmon resonance of gold nanoparticles: from theory to applications," *Chemical reviews*, vol. 107, no. 11, pp. 4797–4862, 2007.
- [17] D. Li and M. I. Stockman, "Electric spaser in the extreme quantum limit," *Phys. Rev. Lett.*, vol. 110, p. 106803, Mar 2013.
- [18] M. I. Stockman, "The spaser as a nanoscale quantum generator and ultrafast amplifier," *J. Opt.*, vol. 12, no. 2, p. 024004, 2010.
- [19] V. Apalkov and M. I. Stockman, "Proposed graphene nanospaser," *Light Sci. Appl.*, vol. 3, Jul. 2014.

- [20] M. I. Stockman, "Spasers explained," *Nat. Photonics*, vol. 2, no. 6, pp. 327–329, 2008.
- [21] —, "Nanoplasmonics: past, present, and glimpse into future," *Opt. Express*, vol. 19, no. 22, pp. 22 029–22 106, Oct 2011.
- [22] C. Rupasinghe, I. D. Rukhlenko, and M. Premaratne, "Spaser made of graphene and carbon nanotubes," *ACS Nano*, vol. 8, no. 3, pp. 2431–2438, 2014.
- [23] N. I. Zheludev, S. Prosvirnin, N. Papasimakis, and V. Fedotov, "Lasing spaser," *Nat. Photonics*, vol. 2, no. 6, pp. 351–354, 2008.
- [24] C. Rupasinghe, I. D. Rukhlenko, and M. Premaratne, "Design optimization of spasers considering the degeneracy of excited plasmon modes," *Opt. Express*, vol. 21, no. 13, pp. 15 335–15 349, 2013.
- [25] S.-W. Chang, C.-Y. A. Ni, and S.-L. Chuang, "Theory for bowtie plasmonic nanolasers," *Opt. Express*, vol. 16, no. 14, pp. 10 580–10 595, 2008.
- [26] D. G. Baranov, E. Andrianov, A. P. Vinogradov, and A. A. Lisyansky, "Exactly solvable toy model for surface plasmon amplification by stimulated emission of radiation," *Opt. Express*, vol. 21, no. 9, pp. 10 779–10 791, May 2013.
- [27] M. A. Noginov, G. Zhu, A. M. Belgrave, R. Bakker, V. M. Shalaev, E. E. Narimanov, S. Stout, E. Herz, T. Suteewong, and U. Wiesner, "Demonstration of a spaser-based nanolaser." *Nature*, vol. 460, no. 7259, pp. 1110–1112, Aug 2009.
- [28] M. T. Hill, M. Marell, E. S. P. Leong, B. Smalbrugge, Y. Zhu, M. Sun, P. J. van Veldhoven, E. J. Geluk, F. Karouta, Y.-S. Oei, R. Nötzel, C.-Z. Ning, and M. K. Smit, "Lasing in metal-insulator-metal sub-wavelength plasmonic waveguides," *Opt. Express*, vol. 17, no. 13, pp. 11 107–11 112, Jun 2009.
- [29] R. F. Oulton, V. J. Sorger, T. Zentgraf, R.-M. Ma, C. Gladden, L. Dai, G. Bartal, and X. Zhang, "Plasmon lasers at deep subwavelength scale," *Nature*, vol. 461, no. 7264, pp. 629–632, 2009.

- [30] R.-M. Ma, R. F. Oulton, V. J. Sorger, G. Bartal, and X. Zhang, "Room-temperature sub-diffraction-limited plasmon laser by total internal reflection," *Nat. Mater.*, vol. 10, no. 2, pp. 110–113, 2011.
- [31] H. Ramakrishna Matte, A. Gomathi, A. K. Manna, D. J. Late, R. Datta, S. K. Pati, and C. Rao, "MoS<sub>2</sub> and WS<sub>2</sub> analogues of graphene," *Angewandte Chemie*, vol. 122, no. 24, pp. 4153–4156, 2010.
- [32] Y. Wang, J. Z. Ou, A. F. Chrimes, B. J. Carey, T. Daeneke, M. M. Alsaif, M. Mortazavi, S. Zhuiykov, N. Medhekar, M. Bhaskaran *et al.*, "Plasmon resonances of highly doped two-dimensional MoS<sub>2</sub>," *Nano Lett.*, vol. 15, no. 2, pp. 883–890, 2015.
- [33] A. Grigorenko, M. Polini, and K. Novoselov, "Graphene plasmonics," *Nat. Photonics*, vol. 6, no. 11, pp. 749–758, 2012.
- [34] T. Low and P. Avouris, "Graphene plasmonics for terahertz to mid-infrared applications," *ACS Nano*, vol. 8, no. 2, pp. 1086–1101, 2014.
- [35] S. Thongrattanasiri, I. Silveiro, and F. Javier García de Abajo, "Plasmons in electrostatically doped graphene," *Applied Physics Letters*, vol. 100, no. 20, p. 201105, 2012.
- [36] M. Gullans, D. Chang, F. Koppens, F. G. de Abajo, and M. D. Lukin, "Single-photon nonlinear optics with graphene plasmons," *Physical Review Letters*, vol. 111, no. 24, p. 247401, 2013.
- [37] S. Thongrattanasiri, A. Manjavacas, and F. J. Garcia de Abajo, "Quantum finite-size effects in graphene plasmons," *Acs Nano*, vol. 6, no. 2, pp. 1766–1775, 2012.
- [38] E. Hwang and S. D. Sarma, "Dielectric function, screening, and plasmons in two-dimensional graphene," *Physical Review B*, vol. 75, no. 20, p. 205418, 2007.
- [39] M. R. Das, R. K. Sarma, R. Saikia, V. S. Kale, M. V. Shelke, and P. Sengupta, "Synthesis of silver nanoparticles in an aqueous suspension of graphene oxide sheets and its antimicrobial activity," *Colloids and Surfaces B: Biointerfaces*, vol. 83, no. 1, pp. 16–22, 2011.

- [40] C. Jang, S. Adam, J.-H. Chen, E. Williams, S. D. Sarma, and M. Fuhrer, "Tuning the effective fine structure constant in graphene: Opposing effects of dielectric screening on short-and long-range potential scattering," *Physical review letters*, vol. 101, no. 14, p. 146805, 2008.
- [41] Y.-W. Tan, Y. Zhang, K. Bolotin, Y. Zhao, S. Adam, E. Hwang, S. D. Sarma, H. Stormer, and P. Kim, "Measurement of scattering rate and minimum conductivity in graphene," *Physical review letters*, vol. 99, no. 24, p. 246803, 2007.
- [42] E. Hwang, S. Adam, and S. D. Sarma, "Carrier transport in two-dimensional graphene layers," *Physical review letters*, vol. 98, no. 18, p. 186806, 2007.
- [43] S. D. Sarma, S. Adam, E. Hwang, and E. Rossi, "Electronic transport in two-dimensional graphene," *Reviews of Modern Physics*, vol. 83, no. 2, p. 407, 2011.
- [44] S. Kim, I. Jo, D. C. Dillen, D. A. Ferrer, B. Fallahazad, Z. Yao, S. K. Banerjee, and E. Tutuc, "Direct measurement of the fermi energy in graphene using a double-layer heterostructure," *Phys. Rev. Lett.*, vol. 108, p. 116404, Mar 2012.
- [45] Z. Fei, A. Rodin, G. Andreev, W. Bao, A. McLeod, M. Wagner, L. Zhang, Z. Zhao, M. Thiemens, G. Dominguez, M. Fogler, A. C. Neto, C. Lau, F. Keilmann, and D. Bascov, "Gate-tuning of graphene plasmons revealed by infrared nano-imaging," *Nature*, 2012.
- [46] W. Zhu, F. Xiao, M. Kang, D. Sikdar, and M. Premaratne, "Tunable terahertz left-handed metamaterial based on multi-layer graphene-dielectric composite," *Appl. Phys. Lett.*, vol. 104, no. 5, p. 051902, 2014.
- [47] R. Frindt and A. Yoffe, "Physical properties of layer structures: optical properties and photoconductivity of thin crystals of molybdenum disulphide," in *Proceedings of the Royal Society of London A: Mathematical, Physical and Engineering Sciences*, vol. 273, no. 1352. The Royal Society, 1963, pp. 69–83.
- [48] J. Du, Q. Wang, G. Jiang, C. Xu, C. Zhao, Y. Xiang, Y. Chen, S. Wen, and H. Zhang, "Ytterbium-doped fiber laser passively mode locked by few-layer molybdenum

- disulfide (mos<sub>2</sub>) saturable absorber functioned with evanescent field interaction," *Scientific reports*, vol. 4, p. 6346, 2014.
- [49] W. Zhou, X. Zou, S. Najmaei, Z. Liu, Y. Shi, J. Kong, J. Lou, P. M. Ajayan, B. I. Yakobson, and J.-C. Idrobo, "Intrinsic structural defects in monolayer molybdenum disulfide," *Nano letters*, vol. 13, no. 6, pp. 2615–2622, 2013.
- [50] R. Wang, B. A. Ruzicka, N. Kumar, M. Z. Bellus, H.-Y. Chiu, and H. Zhao, "Ultrafast and spatially resolved studies of charge carriers in atomically thin molybdenum disulfide," *Physical Review B*, vol. 86, no. 4, p. 045406, 2012.
- [51] A. P. Nayak, T. Pandey, D. Voiry, J. Liu, S. T. Moran, A. Sharma, C. Tan, C.-H. Chen, L.-J. Li, M. Chhowalla *et al.*, "Pressure-dependent optical and vibrational properties of monolayer molybdenum disulfide," *Nano letters*, vol. 15, no. 1, pp. 346–353, 2014.
- [52] J. Lin, H. Li, H. Zhang, and W. Chen, "Plasmonic enhancement of photocurrent in mos<sub>2</sub> field-effect-transistor," *Applied Physics Letters*, vol. 102, no. 20, p. 203109, 2013.
- [53] K. J. Klabunde and R. Richards, *Nanoscale materials in chemistry*. Wiley Online Library, 2001, vol. 1035.
- [54] A. Scholz, T. Stauber, and J. Schliemann, "Plasmons and screening in a monolayer of mos<sub>2</sub>," *Physical Review B*, vol. 88, no. 3, p. 035135, 2013.
- [55] A. N. Enyashin, S. Gemming, M. Bar-Sadan, R. Popovitz-Biro, S. Y. Hong, Y. Prior, R. Tenne, and G. Seifert, "Structure and stability of molybdenum sulfide fullerenes," *Angewandte Chemie International Edition*, vol. 46, no. 4, pp. 623–627, 2007.
- [56] K. J. Si, D. Sikdar, Y. Chen, F. Eftekhari, Z. Xu, Y. Tang, W. Xiong, P. Guo, S. Zhang, Y. Lu *et al.*, "Giant plasmene nanosheets, nanoribbons, and origami," *ACS Nano*, vol. 8, no. 11, pp. 11 086–11 093, 2014.
- [57] T. Low, R. Roldán, H. Wang, F. Xia, P. Avouris, L. M. Moreno, and F. Guinea, "Plasmons and screening in monolayer and multilayer black phosphorus," *Physical review letters*, vol. 113, no. 10, p. 106802, 2014.

- [58] K.-T. Lam and J. Guo, "Plasmonics in strained monolayer black phosphorus," *Journal of Applied Physics*, vol. 117, no. 11, p. 113105, 2015.
- [59] Z. Li, Y. Xiao, Y. Gong, Z. Wang, Y. Kang, S. Zu, P. M. Ajayan, P. Nordlander, and Z. Fang, "Active light control of the mos2 monolayer exciton binding energy," *ACS Nano*, 2015.
- [60] A. Newaz, D. Prasai, J. Ziegler, D. Caudel, S. Robinson, R. Haglund Jr, and K. Bolotin, "Electrical control of optical properties of monolayer mos 2," *Solid State Communications*, vol. 155, pp. 49–52, 2013.
- [61] J. B. Khurgin and G. Sun, "Comparative analysis of spasers, vertical-cavity surface-emitting lasers and surface-plasmon-emitting diodes," *Nat. Photonics*, vol. 8, no. 6, pp. 468–473, 2014.
- [62] K. E. Dorfman, P. K. Jha, D. V. Voronine, P. Genevet, F. Capasso, and M. O. Scully, "Quantum-coherence-enhanced surface plasmon amplification by stimulated emission of radiation," *Phys. Rev. Lett.*, vol. 111, p. 043601, Jul 2013.
- [63] X. Zhong, M. Hong, and Z. Li, "Spaser in plasmonic nano-antenna evaluated by an analytical theory," *Appl. Phys. A*, vol. 115, no. 1, pp. 5–11, 2014.
- [64] R. Flynn, C. Kim, I. Vurgaftman, M. Kim, J. Meyer, A. Mäkinen, K. Bussmann, L. Cheng, F.-S. Choa, and J. Long, "A room-temperature semiconductor spaser operating near 1.5  $\mu\text{m}$ ," *Opt. Express*, vol. 19, no. 9, pp. 8954–8961, 2011.
- [65] O. L. Berman, R. Y. Kezerashvili, and Y. E. Lozovik, "Graphene nanoribbon based spaser," *Phys. Rev. B*, vol. 88, p. 235424, Dec 2013.
- [66] Q. Bao, H. Zhang, B. Wang, Z. Ni, C. H. Y. X. Lim, Y. Wang, D. Y. Tang, and K. P. Loh, "Broadband graphene polarizer," *Nat. Photonics*, vol. 5, no. 7, pp. 411–415, 2011.
- [67] J. Wang, W. B. Lu, X. B. Li, Z. H. Ni, and T. Qiu, "Graphene plasmon guided along a nanoribbon coupled with a nanoring," *J. Phys. D: Appl. Phys.*, vol. 47, no. 13, p. 135106, 2014.

- [68] D. Sikdar and M. Premaratne, "Electrically tunable directional spp propagation in gold-nanoparticle-assisted graphene nanoribbons," in *Photonics Conference (IPC), 2014 IEEE*. IEEE, 2014, pp. 330–331.
- [69] W. Wang, S. Xiao, and N. A. Mortensen, "Localized plasmons in bilayer graphene nanodisks," *Physical Review B*, vol. 93, no. 16, p. 165407, 2016.
- [70] X. Yan, L. Zhu, Y. Zhou, E. Yiwen, L. Wang, and X. Xu, "Dielectric property of mos 2 crystal in terahertz and visible regions," *Applied optics*, vol. 54, no. 22, pp. 6732–6736, 2015.
- [71] B. Mukherjee, F. Tseng, D. Gunlycke, K. K. Amara, G. Eda, and E. Simsek, "Complex electrical permittivity of the monolayer molybdenum disulfide (mos 2) in near uv and visible," *Optical Materials Express*, vol. 5, no. 2, pp. 447–455, 2015.
- [72] A. Castellanos-Gomez, "Black phosphorus: narrow gap, wide applications," *J. Phys. Chem. Lett*, vol. 6, no. 21, pp. 4280–4291, 2015.
- [73] Z. Liu and K. Aydin, "Localized surface plasmons in nanostructured monolayer black phosphorus," *Nano letters*, vol. 16, no. 6, pp. 3457–3462, 2016.
- [74] A. Nemilentsau, T. Low, and G. Hanson, "Anisotropic 2d materials for tunable hyperbolic plasmonics," *Physical review letters*, vol. 116, no. 6, p. 066804, 2016.
- [75] X. Ling, H. Wang, S. Huang, F. Xia, and M. S. Dresselhaus, "The renaissance of black phosphorus," *Proceedings of the National Academy of Sciences*, vol. 112, no. 15, pp. 4523–4530, 2015.
- [76] W. Zhu, M. Premaratne, S. D. Gunapala, G. P. Agrawal, and M. I. Stockman, "Quasi-static analysis of controllable optical cross-sections of a layered nanoparticle with a sandwiched gain layer," *J. Opt.*, vol. 16, no. 7, p. 075003, 2014.
- [77] J. Chen, M. Badioli, P. Alonso-González, S. Thongrattanasiri, F. Huth, J. Osmond, M. Spasenović, A. Centeno, A. Pesquera, P. Godignon *et al.*, "Optical nano-imaging of gate-tunable graphene plasmons," *Nature*, vol. 487, no. 7405, pp. 77–81, 2012.

- [78] A. Y. Nikitin, F. Guinea, F. García-Vidal, and L. Martín-Moreno, "Edge and waveguide terahertz surface plasmon modes in graphene microribbons," *Phys. Rev. B*, vol. 84, no. 16, p. 161407, 2011.
- [79] K. J. Ooi, H. S. Chu, L. K. Ang, and P. Bai, "Mid-infrared active graphene nanoribbon plasmonic waveguide devices," *JOSA B*, vol. 30, no. 12, pp. 3111–3116, 2013.
- [80] L. W. Casperson, "Cylindrical laser resonators," *J. Opt. Soc. Am.*, vol. 63, no. 1, pp. 25–29, 1973.
- [81] T. Chakraborty and V. M. Apalkov, "Quantum cascade transitions in nanostructures," *Adv. Phys.*, vol. 52, no. 5, pp. 455–521, 2003.
- [82] D. Sikdar, I. D. Rukhlenko, W. Cheng, and M. Premaratne, "Unveiling ultrasharp scattering-switching signatures of layered gold-dielectric-gold nanospheres," *J. Opt. Soc. Am. B*, vol. 30, no. 8, pp. 2066–2074, 2013.
- [83] K. S. Novoselov, A. K. Geim, S. V. Morozov, D. Jiang, Y. Zhang, S. V. Dubonos, I. V. Grigorieva, and A. A. Firsov, "Electric field effect in atomically thin carbon films," *science*, vol. 306, no. 5696, pp. 666–669, 2004.
- [84] A. K. Geim and K. S. Novoselov, "The rise of graphene," *Nature materials*, vol. 6, no. 3, pp. 183–191, 2007.
- [85] A. C. Neto, F. Guinea, N. M. Peres, K. S. Novoselov, and A. K. Geim, "The electronic properties of graphene," *Reviews of modern physics*, vol. 81, no. 1, p. 109, 2009.
- [86] P. Blake, E. Hill, A. Castro Neto, K. Novoselov, D. Jiang, R. Yang, T. Booth, and A. Geim, "Making graphene visible," *Applied Physics Letters*, vol. 91, no. 6, p. 063124, 2007.
- [87] A. C. Ferrari, J. Meyer, V. Scardaci, C. Casiraghi, M. Lazzeri, F. Mauri, S. Piscanec, D. Jiang, K. Novoselov, S. Roth *et al.*, "Raman spectrum of graphene and graphene layers," *Physical review letters*, vol. 97, no. 18, p. 187401, 2006.
- [88] R. Q. Yang, "Infrared laser based on intersubband transitions in quantum wells," *Superlatt. Microstruct.*, vol. 17, no. 1, pp. 77 –, 1995.

- [89] J. Faist, F. Capasso, D. L. Sivco, C. Sirtori, A. L. Hutchinson, and A. Y. Cho, "Quantum cascade laser," *Science*, vol. 264, no. 5158, pp. 553–556, 1994.
- [90] J. Faist, F. Capasso, C. Sirtori, D. L. Sivco, A. L. Hutchinson, and A. Y. Cho, "Vertical transition quantum cascade laser with bragg confined excited state," *Appl. Phys. Lett.*, vol. 66, no. 5, pp. 538–540, 1995.
- [91] Z. Fang, S. Thongrattanasiri, A. Schlather, Z. Liu, L. Ma, Y. Wang, P. M. Ajayan, P. Nordlander, N. J. Halas, and F. J. García de Abajo, "Gated tunability and hybridization of localized plasmons in nanostructured graphene," *ACS Nano*, vol. 7, no. 3, pp. 2388–2395, 2013.
- [92] E. Andrianov, N. Chtchelkatchev, and A. Pukhov, "Noisy metamolecule: strong narrowing of fluorescence line," *Opt. Lett.*, vol. 40, no. 15, pp. 3536–3539, 2015.
- [93] M. L. Marasinghe, M. Premaratne, and D. M. Paganin, "Coherence vortices in mie scattering of statistically stationary partially coherent fields," *Opt. Express*, vol. 18, no. 7, pp. 6628–6641, 2010.
- [94] M. L. Marasinghe, D. M. Paganin, and M. Premaratne, "Coherence-vortex lattice formed via mie scattering of partially coherent light by several dielectric nanospheres," *Opt. Lett.*, vol. 36, no. 6, pp. 936–938, 2011.
- [95] S. Liu, C. Zhang, M. Hu, X. Chen, P. Zhang, S. Gong, T. Zhao, and R. Zhong, "Coherent and tunable terahertz radiation from graphene surface plasmon polaritons excited by an electron beam," *Appl. Phys. Lett.*, vol. 104, no. 20, p. 201104, 2014.
- [96] M. Kuttge, F. J. Garcia de Abajo, and A. Polman, "Ultrasmall mode volume plasmonic nanodisk resonators," *Nano Lett.*, vol. 10, no. 5, pp. 1537–1541, 2009.
- [97] J. Faist, F. Capasso, C. Sirtori, D. L. Sivco, A. L. Hutchinson, and A. Y. Cho, "Vertical transition quantum cascade laser with bragg confined excited state," *Appl. Phys. Lett.*, vol. 66, no. 5, pp. 538–540, 1995.
- [98] J. Faist, F. Capasso, D. L. Sivco, C. Sirtori, A. L. Hutchinson, A. Y. Cho *et al.*, "Quantum cascade laser," *Science*, vol. 264, no. 5158, pp. 553–556, 1994.

- [99] B. Williams, "Terahertz quantum cascade lasers," in *Asia Optical Fiber Communication and Optoelectronic Exposition and Conference*. Optical Society of America, 2008, p. SuG3.
- [100] C. Gmachl, F. Capasso, D. L. Sivco, and A. Y. Cho, "Recent progress in quantum cascade lasers and applications," *Reports on progress in physics*, vol. 64, no. 11, p. 1533, 2001.
- [101] G. Dehlinger, L. Diehl, U. Gennser, H. Sigg, J. Faist, K. Ensslin, D. Grützmacher, and E. Müller, "Intersubband electroluminescence from silicon-based quantum cascade structures," *Science*, vol. 290, no. 5500, pp. 2277–2280, 2000.
- [102] H. Luo, S. Laframboise, Z. Wasilewski, G. Aers, H. Liu, and J. Cao, "Terahertz quantum-cascade lasers based on a three-well active module," *Applied physics letters*, vol. 90, no. 4, p. 041112, 2007.
- [103] J. Faist, F. Capasso, C. Sirtori, D. L. Sivco, J. N. Baillargeon, A. L. Hutchinson, S.-N. G. Chu, and A. Y. Cho, "High power mid-infrared ( $\lambda = 5 \mu\text{m}$ ) quantum cascade lasers operating above room temperature," *Applied Physics Letters*, vol. 68, no. 26, pp. 3680–3682, 1996.
- [104] F. Capasso, "Band-gap engineering: from physics and materials to new semiconductor devices," *Science*, vol. 235, pp. 172–177, 1987.
- [105] O. Painter, R. Lee, A. Scherer, A. Yariv, J. O'Brien, P. Dapkus, and I. Kim, "Two-dimensional photonic band-gap defect mode laser," *Science*, vol. 284, no. 5421, pp. 1819–1821, 1999.
- [106] A. Mews, A. Kadavanich, U. Banin, and A. Alivisatos, "Structural and spectroscopic investigations of cds/hgs/cds quantum-dot quantum wells," *Physical Review B*, vol. 53, no. 20, p. R13242, 1996.
- [107] P. Bose, N. Paitya, S. Bhattacharya, D. De, S. Saha, K. Chatterjee, S. Pahari, and K. Ghatak, "Influence of light waves on the effective electron mass in quantum

- wells, wires, inversion layers and superlattices," *Quantum Matter*, vol. 1, no. 2, pp. 89–126, 2012.
- [108] D. C. Bertolet, J.-K. Hsu, and K. M. Lau, "Tailoring of hole eigenenergies in strained GaAs/AlGaAs single quantum wells grown by atmospheric pressure organometallic chemical vapor deposition," *Applied physics letters*, vol. 53, no. 25, pp. 2501–2503, 1988.
- [109] R. Q. Yang, "Infrared laser based on intersubband transitions in quantum wells," *Superlatt. Microstruct.*, vol. 17, no. 1, p. 77, 1995.
- [110] R. Nicholas, J. Portal, C. Houlbert, P. Perrier, and T. Pearsall, "An experimental determination of the effective masses for Ga<sub>x</sub>In<sub>1-x</sub>As<sub>y</sub>P<sub>1-y</sub> alloys grown on InP," *Appl. Phys. Lett.*, vol. 34, no. 8, pp. 492–494, 1979.
- [111] I. B. Udagedara, I. D. Rukhlenko, and M. Premaratne, "Surface plasmon-polariton propagation in piecewise linear chains of composite nanospheres: the role of optical gain and chain layout," *Opt. Express*, vol. 19, no. 21, pp. 19973–19986, 2011.
- [112] —, "Complex- $\omega$  approach versus complex- $k$  approach in description of gain-assisted surface plasmon-polariton propagation along linear chains of metallic nanospheres," *Phys. Rev. B*, vol. 83, no. 11, p. 115451, 2011.
- [113] J. B. Khurgin, "How to deal with the loss in plasmonics and metamaterials," *Nat. Nanotech.*, vol. 10, no. 1, pp. 2–6, 2015.
- [114] —, "Ultimate limit of field confinement by surface plasmon polaritons," *Faraday Discuss.*, vol. 178, pp. 109–122, 2015.
- [115] J. B. Khurgin and G. Sun, "Scaling of losses with size and wavelength in nanoplasmonics and metamaterials," *Appl. Phys. Lett.*, vol. 99, no. 21, p. 211106, 2011.
- [116] —, "How small can nano be in a nanolaser?" *Nanophotonics*, vol. 1, no. 1, pp. 3–8, 2012.
- [117] —, "Practicality of compensating the loss in the plasmonic waveguides using semiconductor gain medium," *Appl. Phys. Lett.*, vol. 100, no. 1, p. 011105, 2012.

- [118] A. P. Vinogradov, E. S. Andrianov, A. A. Pukhov, A. V. Dorofeenko, and A. Lisiansky, "Quantum plasmonics of metamaterials: loss compensation using spasers," *Phys. Uspekhi*, vol. 55, no. 10, pp. 1046–1053, 2012.
- [119] J. B. Khurgin and G. Sun, "In search of the elusive lossless metal," *Appl. Phys. Lett.*, vol. 96, no. 18, p. 181102, 2010.
- [120] X. Meng, K. Fujita, S. Murai, T. Matoba, and K. Tanaka, "Plasmonically controlled lasing resonance with metallic-dielectric core-shell nanoparticles," *Nano Lett.*, vol. 11, no. 3, pp. 1374–1378, 2011.
- [121] A. K. Verma and Z. Rostamy, "Resonant frequencies of shielded rectangular and circular microstrip resonators," *International Journal of Microwave and Millimeter-Wave Computer-Aided Engineering*, vol. 5, no. 1, pp. 13–19, 1995.
- [122] Y. E. Lozovik, I. A. Nechepurenko, A. V. Dorofeenko, E. S. Andrianov, and A. A. Pukhov, "Spaser spectroscopy with subwavelength spatial resolution," *Phys. Lett. A*, vol. 378, no. 9, pp. 723–727, 2014.
- [123] Y. E. Lozovik, I. Nechepurenko, A. Dorofeenko, E. Andrianov, and A. Pukhov, "Highly sensitive spectroscopy based on a surface plasmon polariton quantum generator," *Laser Phys. Lett.*, vol. 11, no. 12, p. 125701, 2014.
- [124] H. T. Hattori, I. McKerracher, H. H. Tan, C. Jagadish, D. La Rue, and R. Michael, "In-plane coupling of light from in-plane-based photonic crystal band-edge lasers into single-mode waveguides," *IEEE Journal of Quantum Electronics*, vol. 43, no. 4, pp. 279–286, 2007.
- [125] R. M. Cazo, O. Lisbôa, H. T. Hattori, V. M. Schneider, C. L. Barbosa, R. C. Rabelo, and J. L. Ferreira, "Experimental analysis of reflected modes in a multimode strained grating," *Microwave and Opt. Tech. Lett.*, vol. 28, no. 1, pp. 4–8, 2001.
- [126] C. Jayasekara, M. Premaratne, S. D. Gunapala, and M. I. Stockman, "MoS<sub>2</sub> spaser," *Journal of Applied Physics*, vol. 119, no. 13, p. 133101, 2016.

- [127] D. Weeraddana, M. Premaratne, and D. L. Andrews, "Direct and third-body mediated resonance energy transfer in dimensionally constrained nanostructures," *Phys. Rev. B*, vol. 92, no. 3, p. 035128, 2015.
- [128] —, "Quantum electrodynamics of resonance energy transfer in nanowire systems," *Physical Review B*, vol. 93, no. 7, p. 075151, 2016.
- [129] D. Weeraddana, M. Premaratne, S. D. Gunapala, and D. L. Andrews, "Quantum electrodynamical theory of high-efficiency excitation energy transfer in laser-driven nanostructure systems," *Physical Review B*, vol. 94, no. 8, p. 085133, 2016.
- [130] C. Jayasekara, M. Premaratne, S. D. Gunapala, and M. I. Stockman, "Is  $\text{mos}_2$  better for spasers than graphene?" in *Lasers and Electro-Optics (CLEO), 2016 Conference on*. Optical Society of America, 2016, pp. 1–2.
- [131] E. H Sargent, "Infrared quantum dots," *Advanced Materials*, vol. 17, no. 5, pp. 515–522, 2005.
- [132] I. Moreels, K. Lambert, D. Smeets, D. De Muynck, T. Nollet, J. C. Martins, F. Vanhaecke, A. Vantomme, C. Delerue, G. Allan *et al.*, "Size-dependent optical properties of colloidal pbs quantum dots," *ACS nano*, vol. 3, no. 10, pp. 3023–3030, 2009.
- [133] T. E. Sale, *Vertical cavity surface emitting lasers*. Research Studies Press Taunton, 1995.
- [134] C. W. Wilmsen, H. Temkin, and L. A. Coldren, "Vertical-cavity surface-emitting lasers," *Vertical-Cavity Surface-Emitting Lasers, Edited by Carl W. Wilmsen and Henryk Temkin and Larry A. Coldren*, pp. 474. ISBN 0521590221. Cambridge, UK: Cambridge University Press, July 1999., vol. 1, 1999.
- [135] K. Lear, K. Choquette, R. Schneider, S. Kilcoyne, and K. Geib, "Selectively oxidised vertical cavity surface emitting lasers with 50% power conversion efficiency," *Electronics Letters*, vol. 31, no. 3, pp. 208–209, 1995.

- [136] F. Koyama, S. Kinoshita, and K. Iga, "Room-temperature continuous wave lasing characteristics of a gas vertical cavity surface-emitting laser," *Applied physics letters*, vol. 55, no. 3, pp. 221–222, 1989.
- [137] Z. G. Pan, S. Jiang, M. Dagenais, R. A. Morgan, K. Kojima, M. T. Asom, R. E. Leibenguth, G. D. Guth, and M. W. Focht, "Optical injection induced polarization bistability in vertical-cavity surface-emitting lasers," *Applied physics letters*, vol. 63, no. 22, pp. 2999–3001, 1993.
- [138] C. J. Chang-Hasnain, J. Harbison, G. Hasnain, A. C. Von Lehmen, L. Florez, and N. Stoffel, "Dynamic, polarization, and transverse mode characteristics of vertical cavity surface emitting lasers," *IEEE Journal of Quantum Electronics*, vol. 27, no. 6, pp. 1402–1409, 1991.
- [139] J. L. Jewell, J. Harbison, A. Scherer, Y. Lee, and L. Florez, "Vertical-cavity surface-emitting lasers: design, growth, fabrication, characterization," *IEEE Journal of Quantum Electronics*, vol. 27, no. 6, pp. 1332–1346, 1991.
- [140] B. Lee, S. Kim, H. Kim, and Y. Lim, "The use of plasmonics in light beaming and focusing," *Progress in Quantum Electronics*, vol. 34, no. 2, pp. 47–87, 2010.
- [141] F. Xiong, H. Wang, X. Liu, J. Sun, M. Brongersma, E. Pop, and Y. Cui, "Li intercalation in  $\text{mos}_2$ : In situ observation of its dynamics and tuning optical and electrical properties," *Nano lett.*, vol. 15, no. 10, pp. 6777–6784, 2015.
- [142] Y. Zhang, S. Wang, H. Yu, H. Zhang, Y. Chen, L. Mei, A. Di Lieto, M. Tonelli, and J. Wang, "Atomic-layer molybdenum sulfide optical modulator for visible coherent light," *Scientific reports*, vol. 5, 2015.
- [143] K. Blum, *Density matrix theory and applications*. Springer Science & Business Media, 2012, vol. 64.
- [144] C. Yim, M. O'Brien, N. McEvoy, S. Winters, I. Mirza, J. G. Lunney, and G. S. Duesberg, "Investigation of the optical properties of  $\text{mos}_2$  thin films using spectroscopic ellipsometry," *Applied Physics Letters*, vol. 104, no. 10, p. 103114, 2014.

- [145] M. J. Bloemer, M. Buncick, R. Warmack, and T. Ferrell, "Surface electromagnetic modes in prolate spheroids of gold, aluminum, and copper," *JOSA B*, vol. 5, no. 12, pp. 2552–2559, 1988.
- [146] M. Rycenga, C. M. Cobley, J. Zeng, W. Li, C. H. Moran, Q. Zhang, D. Qin, and Y. Xia, "Controlling the synthesis and assembly of silver nanostructures for plasmonic applications," *Chemical reviews*, vol. 111, no. 6, pp. 3669–3712, 2011.
- [147] P. K. Jain, K. S. Lee, I. H. El-Sayed, and M. A. El-Sayed, "Calculated absorption and scattering properties of gold nanoparticles of different size, shape, and composition: applications in biological imaging and biomedicine," *J. Phys. Chem. B*, vol. 110, no. 14, pp. 7238–7248, 2006.
- [148] B. J. Wiley, S. H. Im, Z.-Y. Li, J. McLellan, A. Siekkinen, and Y. Xia, "Maneuvering the surface plasmon resonance of silver nanostructures through shape-controlled synthesis," *J. Phys. Chem. B*, vol. 110, no. 32, 2006.
- [149] X. Huang, I. H. El-Sayed, W. Qian, and M. A. El-Sayed, "Cancer cell imaging and photothermal therapy in the near-infrared region by using gold nanorods," *Journal of the American Chemical Society*, vol. 128, no. 6, pp. 2115–2120, 2006.
- [150] E. Ringe, J. M. McMahon, K. Sohn, C. Cobley, Y. Xia, J. Huang, G. C. Schatz, L. D. Marks, and R. P. Van Duyne, "Unraveling the effects of size, composition, and substrate on the localized surface plasmon resonance frequencies of gold and silver nanocubes: a systematic single-particle approach," *The Journal of Physical Chemistry C*, vol. 114, no. 29, pp. 12 511–12 516, 2010.
- [151] J. Fabian, H. Nakazumi, and M. Matsuoka, "Near-infrared absorbing dyes," *Chemical Reviews*, vol. 92, no. 6, pp. 1197–1226, 1992.
- [152] V. Klimov, A. Mikhailovsky, S. Xu, A. Malko, J. Hollingsworth, C. Leatherdale, H.-J. Eisler, and M. Bawendi, "Optical gain and stimulated emission in nanocrystal quantum dots," *Science*, vol. 290, no. 5490, pp. 314–317, 2000.

- [153] D. Norris, A. Sacra, C. Murray, and M. Bawendi, "Measurement of the size dependent hole spectrum in cdse quantum dots," *Physical review letters*, vol. 72, no. 16, p. 2612, 1994.
- [154] X. Michalet, F. Pinaud, L. Bentolila, J. Tsay, S. Doose, J. Li, G. Sundaresan, A. Wu, S. Gambhir, and S. Weiss, "Quantum dots for live cells, in vivo imaging, and diagnostics," *science*, vol. 307, no. 5709, pp. 538–544, 2005.
- [155] A. Guzelian, U. Banin, A. Kadavanich, X. Peng, and A. Alivisatos, "Colloidal chemical synthesis and characterization of inas nanocrystal quantum dots," *Applied physics letters*, vol. 69, no. 10, pp. 1432–1434, 1996.
- [156] W. Zhang, G. Chen, J. Wang, B.-C. Ye, and X. Zhong, "Design and synthesis of highly luminescent near-infrared-emitting water-soluble cdte/cdse/zns core/shell/shell quantum dots," *Inorganic chemistry*, vol. 48, no. 20, pp. 9723–9731, 2009.
- [157] H. Zollinger, *Color chemistry: syntheses, properties, and applications of organic dyes and pigments*. John Wiley & Sons, 2003.
- [158] W. F. Krupke, "Optical absorption and fluorescence intensities in several rare-earth-doped  $\text{Y}_2\text{O}_3$  and  $\text{LaF}_3$  single crystals," *Physical Review*, vol. 145, no. 1, p. 325, 1966.
- [159] Y.-C. Li, Y.-H. Chang, Y.-F. Lin, Y.-S. Chang, and Y.-J. Lin, "Synthesis and luminescent properties of  $\text{In}^{3+}$ ( $\text{Eu}^{3+}$ ,  $\text{Sm}^{3+}$ ,  $\text{Dy}^{3+}$ )-doped lanthanum aluminum germanate  $\text{LaAlGe}_2\text{O}_7$  phosphors," *Journal of alloys and compounds*, vol. 439, no. 1, pp. 367–375, 2007.
- [160] S.-H. Kwon, J.-H. Kang, C. Seassal, S.-K. Kim, P. Regreny, Y.-H. Lee, C. M. Lieber, and H.-G. Park, "Subwavelength plasmonic lasing from a semiconductor nanodisk with silver nanopan cavity," *Nano letters*, vol. 10, no. 9, pp. 3679–3683, 2010.
- [161] M. Richter, M. Gegg, T. S. Theuerholz, and A. Knorr, "Numerically exact solution of the many emitter–cavity laser problem: Application to the fully quantized spaser emission," *Physical Review B*, vol. 91, no. 3, p. 035306, 2015.

- [162] M. I. Stockman, "Nanoplasmonics: The physics behind the applications," *Physics Today*, vol. 64, no. 2, pp. 39–44, 2011.
- [163] K. Li, X. Li, M. I. Stockman, and D. J. Bergman, "Surface plasmon amplification by stimulated emission in nanolenses," *Physical review B*, vol. 71, no. 11, p. 115409, 2005.
- [164] T. V. Shahbazyan and M. I. Stockman, *Plasmonics: theory and applications*. Springer, 2013.
- [165] M. Rycenga, C. M. Cobley, J. Zeng, W. Li, C. H. Moran, Q. Zhang, D. Qin, and Y. Xia, "Controlling the synthesis and assembly of silver nanostructures for plasmonic applications," *Chemical reviews*, vol. 111, no. 6, pp. 3669–3712, 2011.
- [166] S. L. Brandow, M.-S. Chen, T. Wang, C. S. Dulcey, J. M. Calvert, J. F. Bohland, G. S. Calabrese, and W. J. Dressick, "Size-controlled colloidal pd (ii) catalysts for electroless ni deposition in nanolithography applications," *Journal of The Electrochemical Society*, vol. 144, no. 10, pp. 3425–3434, 1997.
- [167] W. Zhou and Z. L. Wang, *Scanning microscopy for nanotechnology: techniques and applications*. Springer science & business media, 2007.
- [168] A. Camposeo, F. Cervelli, A. Piombini, F. Tantussi, F. Fuso, M. Allegrini, and E. Arimondo, "A laser-cooled atom beam for nanolithography applications," *Materials Science and Engineering: C*, vol. 23, no. 1, pp. 217–220, 2003.
- [169] K. Salaita, Y. Wang, and C. A. Mirkin, "Applications of dip-pen nanolithography," *Nature nanotechnology*, vol. 2, no. 3, pp. 145–155, 2007.
- [170] M. Aeschlimann, T. Brixner, A. Fischer, C. Kramer, P. Melchior, W. Pfeiffer, C. Schneider, C. Strüber, P. Tuchscherer, and D. V. Voronine, "Coherent two-dimensional nanoscopy," *Science*, vol. 333, no. 6050, pp. 1723–1726, 2011.
- [171] J. Fölling, M. Bossi, H. Bock, R. Medda, C. A. Wurm, B. Hein, S. Jakobs, C. Eggeling, and S. W. Hell, "Fluorescence nanoscopy by ground-state depletion and single-molecule return," *Nature methods*, vol. 5, no. 11, pp. 943–945, 2008.

- [172] S. W. Hell, "Far-field optical nanoscopy," *science*, vol. 316, no. 5828, pp. 1153–1158, 2007.
- [173] D. Ronnlund, L. Xu, A. Perols, A. K. Gad, A. Eriksson Karlstrom, G. Auer, and J. Widengren, "Multicolor fluorescence nanoscopy by photobleaching: Concept, verification, and its application to resolve selective storage of proteins in platelets," *ACS nano*, vol. 8, no. 5, pp. 4358–4365, 2014.
- [174] C. Brune, A. Sawatzky, and M. Burger, "Primal and dual bregman methods with application to optical nanoscopy," *International Journal of Computer Vision*, vol. 92, no. 2, pp. 211–229, 2011.
- [175] —, "Bregman-em-tv methods with application to optical nanoscopy," *Scale Space and Variational Methods in Computer Vision*, pp. 235–246, 2009.
- [176] H. Blom and M. Bates, "Nanoscopyimaging life at the nanoscale: a nobel prize achievement with a bright future," *Physica Scripta*, vol. 90, no. 10, p. 108010, 2015.
- [177] L. Novak, P. Neuzil, J. Pipper, Y. Zhang, and S. Lee, "An integrated fluorescence detection system for lab-on-a-chip applications," *Lab on a Chip*, vol. 7, no. 1, pp. 27–29, 2007.
- [178] S. Balslev, A. Jorgensen, B. Bilenberg, K. B. Mogensen, D. Snakenborg, O. Geschke, J. P. Kutter, and A. Kristensen, "Lab-on-a-chip with integrated optical transducers," *Lab on a Chip*, vol. 6, no. 2, pp. 213–217, 2006.
- [179] A. Pais, A. Banerjee, D. Klotzkin, and I. Papautsky, "High-sensitivity, disposable lab-on-a-chip with thin-film organic electronics for fluorescence detection," *Lab on a Chip*, vol. 8, no. 5, pp. 794–800, 2008.
- [180] S. Haeberle and R. Zengerle, "Microfluidic platforms for lab-on-a-chip applications," *Lab on a Chip*, vol. 7, no. 9, pp. 1094–1110, 2007.
- [181] C. D. Chin, V. Linder, and S. K. Sia, "Lab-on-a-chip devices for global health: Past studies and future opportunities," *Lab on a Chip*, vol. 7, no. 1, pp. 41–57, 2007.

- [182] V. Srinivasan, V. K. Pamula, and R. B. Fair, "An integrated digital microfluidic lab-on-a-chip for clinical diagnostics on human physiological fluids," *Lab on a Chip*, vol. 4, no. 4, pp. 310–315, 2004.
- [183] A. Steane, "Quantum computing," *Reports on Progress in Physics*, vol. 61, no. 2, p. 117, 1998.
- [184] M. Shahriar, P. Hemmer, S. Lloyd, P. Bhatia, and A. Craig, "Solid-state quantum computing using spectral holes," *Physical Review A*, vol. 66, no. 3, p. 032301, 2002.
- [185] T. Hey, "Quantum computing: an introduction," *Computing & Control Engineering Journal*, vol. 10, no. 3, pp. 105–112, 1999.
- [186] H. Häffner, C. F. Roos, and R. Blatt, "Quantum computing with trapped ions," *Physics reports*, vol. 469, no. 4, pp. 155–203, 2008.
- [187] T. D. Ladd, F. Jelezko, R. Laflamme, Y. Nakamura, C. Monroe, and J. L. O'Brien, "Quantum computers," *Nature*, vol. 464, no. 7285, pp. 45–53, 2010.
- [188] J. J. García-Ripoll, P. Zoller, and J. I. Cirac, "Speed optimized two-qubit gates with laser coherent control techniques for ion trap quantum computing," *Physical Review Letters*, vol. 91, no. 15, p. 157901, 2003.
- [189] T. Pellizzari, S. A. Gardiner, J. I. Cirac, and P. Zoller, "Decoherence, continuous observation, and quantum computing: A cavity qed model," *Physical Review Letters*, vol. 75, no. 21, p. 3788, 1995.
- [190] W. L. Barnes, A. Dereux, and T. W. Ebbesen, "Surface plasmon subwavelength optics," *Nature*, vol. 424, no. 6950, pp. 824–830, 2003.
- [191] K. Tanaka and M. Tanaka, "Simulations of nanometric optical circuits based on surface plasmon polariton gap waveguide," *Applied Physics Letters*, vol. 82, no. 8, pp. 1158–1160, 2003.
- [192] M. P. Nezhad, K. Tetz, and Y. Fainman, "Gain assisted propagation of surface plasmon polaritons on planar metallic waveguides," *Optics Express*, vol. 12, no. 17, pp. 4072–4079, 2004.

- [193] M. L. Brongersma and P. G. Kik, *Surface plasmon nanophotonics*. Springer, 2007.
- [194] A. Akbari, R. N. Tait, and P. Berini, "Surface plasmon waveguide schottky detector," *Optics express*, vol. 18, no. 8, pp. 8505–8514, 2010.
- [195] L. Liu, Z. Han, and S. He, "Novel surface plasmon waveguide for high integration," *Optics Express*, vol. 13, no. 17, pp. 6645–6650, 2005.
- [196] N. C. for Locally Advanced Cervical Cancer Meta-analysis Collaboration *et al.*, "Neoadjuvant chemotherapy for locally advanced cervical cancer: a systematic review and meta-analysis of individual patient data from 21 randomised trials." *European journal of cancer (Oxford, England: 1990)*, vol. 39, no. 17, p. 2470, 2003.
- [197] M.-C. Mathieu, R. Rouzier, A. Llombart-Cussac, L. Sideris, S. Koscielny, J. Travagli, G. Contesso, S. Delaloge, and M. Spielmann, "The poor responsiveness of infiltrating lobular breast carcinomas to neoadjuvant chemotherapy can be explained by their biological profile," *European Journal of Cancer*, vol. 40, no. 3, pp. 342–351, 2004.
- [198] P. J. Carey, M. T. Oberst, M. A. McCubbin, and S. H. Hughes, "Appraisal and caregiving burden in family members caring for patients receiving chemotherapy." in *Oncology nursing forum*, vol. 18, no. 8, 1990, pp. 1341–1348.
- [199] R. Rouzier, C. M. Perou, W. F. Symmans, N. Ibrahim, M. Cristofanilli, K. Anderson, K. R. Hess, J. Stec, M. Ayers, P. Wagner *et al.*, "Breast cancer molecular subtypes respond differently to preoperative chemotherapy," *Clinical Cancer Research*, vol. 11, no. 16, pp. 5678–5685, 2005.
- [200] X. Zhang, Y. L. Chen, R.-S. Liu, and D. P. Tsai, "Plasmonic photocatalysis," *Reports on Progress in Physics*, vol. 76, no. 4, p. 046401, 2013.
- [201] C. Rupasinghe, W. Zhu, and M. Premaratne, "Spaser powered photothermal cancer therapy using graphene and carbon nanotubes," in *Photonics Conference (IPC), 2014 IEEE*. IEEE, 2014, pp. 16–17.

- [202] Y. Fang, Z. Li, Y. Huang, S. Zhang, P. Nordlander, N. J. Halas, and H. Xu, "Branched silver nanowires as controllable plasmon routers," *Nano letters*, vol. 10, no. 5, pp. 1950–1954, 2010.
- [203] A. Boardman, M. Brongersma, M. Stockman, and M. Wegener, "Plasmonics and metamaterials: introduction," *JOSA B*, vol. 26, no. 12, pp. PM1–PM1, 2009.
- [204] P. Ginzburg, N. Berkovitch, A. Nevet, I. Shor, and M. Orenstein, "Resonances on-demand for plasmonic nano-particles," *Nano letters*, vol. 11, no. 6, pp. 2329–2333, 2011.
- [205] Y. B. Zheng, B. Kiraly, P. S. Weiss, and T. J. Huang, "Molecular plasmonics for biology and nanomedicine," *Nanomedicine*, vol. 7, no. 5, pp. 751–770, 2012.
- [206] S. Takeuchi, J. Kim, Y. Yamamoto, and H. H. Hogue, "Development of a high-quantum-efficiency single-photon counting system," *Applied Physics Letters*, vol. 74, no. 8, pp. 1063–1065, 1999.
- [207] S. Ganan and D. McClure, "Bayesian image analysis: An application to single photon emission tomography," *Amer. Statist. Assoc.*, pp. 12–18, 1985.
- [208] Z. Yuan, B. E. Kardynal, R. M. Stevenson, A. J. Shields, C. J. Lobo, K. Cooper, N. S. Beattie, D. A. Ritchie, and M. Pepper, "Electrically driven single-photon source," *Science*, vol. 295, no. 5552, pp. 102–105, 2002.
- [209] M. Andresen, A. C. Stiel, J. Fölling, D. Wenzel, A. Schönle, A. Egner, C. Eggeling, S. W. Hell, and S. Jakobs, "Photoswitchable fluorescent proteins enable monochromatic multilabel imaging and dual color fluorescence nanoscopy," *Nature biotechnology*, vol. 26, no. 9, pp. 1035–1040, 2008.
- [210] M. Premaratne and M. I. Stockman, "Theory and technology of spasers," *Advances in Optics and Photonics*, vol. 9, no. 1, pp. 79–128, 2017.
- [211] G. H. B. Thompson, "Physics of semiconductor laser devices," *Chichester, Sussex, England and New York, Wiley-Interscience*, 1980. 572 p., vol. 1, 1980.

- [212] D. Weeraddana, M. Premaratne, and D. L. Andrews, "Optical control of resonance energy transfer in quantum dot systems," in *Nanotechnology Materials and Devices Conference (NMDC), 2016 IEEE*. IEEE, 2016, pp. 1–2.
- [213] F. Stern, "Polarizability of a two-dimensional electron gas," *Phys. Rev. Lett.*, vol. 18, no. 14, p. 546, 1967.
- [214] A. J. Figueredo and P. S. A. Wolf, "Assortative pairing and life history strategy - a cross-cultural study." *Human Nat.*, vol. 20, pp. 317–330, 2009.
- [215] A. Fedorov, A. Baranov, and Y. Masumoto, "Coherent control of optical-phonon-assisted resonance secondary emission in semiconductor quantum dots," *Opt. and Spect.*, vol. 93, no. 1, pp. 52–60, 2002.
- [216] K. Y. Yeung, J. Chee, H. Yoon, Y. Song, J. Kong, and D. Ham, "Far-infrared graphene plasmonic crystals for plasmonic band engineering," *Nano Lett.*, vol. 14, no. 5, pp. 2479–2484, 2014.
- [217] R. Taubert, M. Hentschel, J. Kastel, and H. Giessen, "Classical analog of electromagnetically induced absorption in plasmonics," *Nano Lett.*, vol. 12, no. 3, pp. 1367–1371, 2012.
- [218] D. Y. Fedyanin, "Toward an electrically pumped spaser," *Opt. Lett.*, vol. 37, no. 3, pp. 404–406, Feb 2012.
- [219] M. Jablan, H. Buljan, and M. Soljačić, "Plasmonics in graphene at infrared frequencies," *Phys. Rev. B*, vol. 80, p. 245435, Dec 2009.
- [220] A. V. Dorofeenko, A. A. Zyablovsky, A. P. Vinogradov, E. S. Andrianov, A. A. Pukhov, and A. A. Lisyansky, "Steady state superradiance of a 2d-spaser array," *Optics express*, vol. 21, no. 12, pp. 14 539–14 547, 2013.
- [221] K. E. Dorfman, P. K. Jha, D. V. Voronine, P. Genevet, F. Capasso, and M. O. Scully, "Quantum-coherence-enhanced surface plasmon amplification by stimulated emission of radiation," *Physical review letters*, vol. 111, no. 4, p. 043601, 2013.

- [222] E. S. Andrianov, A. A. Pukhov, A. V. Dorofeenko, A. P. Vinogradov, and A. A. Lisiansky, "Spaser operation below threshold: autonomous vs. driven spasers," *Opt. Express*, vol. 23, no. 17, pp. 21 983–21 993, Aug 2015.
- [223] J. B. Khurgin and G. Sun, "Injection pumped single mode surface plasmon generators: threshold, linewidth, and coherence," *Opt. Express*, vol. 20, no. 14, pp. 15 309–15 325, 2012.
- [224] J. M. Pitarke, V. M. Silkin, C. E. V., and P. M. Echenique, "Theory of surface plasmons and surface-plasmon polaritons," *Rep. Prog. Phys.*, vol. 70, no. 1, 2007.
- [225] P. Lalanne, J. P. Hugonin, and J. C. Rodier, "Theory of Surface Plasmon Generation at Nanoslit Apertures," *Phys. Rev. Lett.*, vol. 94, no. 263902, 2005.
- [226] W. L. Barnes, A. Dereux, and T. W. Ebbesen, "Surface plasmon subwavelength optics," *Nat. Photonics*, vol. 424, pp. 824–830, 2003.
- [227] P. Lalanne, J. P. Hugonin, and J. C. Rodier, "Light in tiny holes," *Nat. Photonics.*, vol. 445, pp. 39–46, 2007.
- [228] C. Genet and T. W. Ebbesen, "Approximate model for surface-plasmon generation at slit apertures," *J. Opt. Soc. Am.*, vol. A 23, pp. 1608–1615, 2006.
- [229] H. Raether, *Surface Plasmons on Smooth and Rough Surfaces and on Gratings*. Springer-Verlag, 1988.
- [230] W. L. Barnes, "Surface plasmon-polariton length scales: A route to sub-wavelength optics," *J. Opt. A: Pure Appl. Opt.*, vol. 8, pp. S87–S93, 2006.
- [231] L. Cohen, *Time-frequency analysis*. Prentice-Hall P'IR, 1995.
- [232] E. Ozbay, "Plasmonics: Merging Photonics and Electronics at Nanoscale Dimensions," *Science*, vol. 311, no. 5758, pp. 189–193, 2006.
- [233] S. A. Maier, M. L. Brongersma, P. G. Kik, S. Meltzer, A. A. G. Requicha, and H. A. Atwater, "Plasmonics - A route to nanoscale optical devices," *Adv. Mater.*, vol. 13, pp. 1501–1505, 2001.

- [234] N.J.Halas, "Connecting the dots: Reinventing optics for nanoscale dimensions," *Proc. Nat. Acad. Sci.*, vol. 106, no. 10, pp. 3643–3644, 2009.
- [235] C. P. Huang and Y. Y. Zhu, "Plasmonics: Manipulating light at the subwavelength scale," *Active and Passive Electronic Components*, vol. 2007, p. 30946, 2007.
- [236] E. K. Stelzer, "Light microscopy: Beyond the diffraction limit?" *Nature*, vol. 417, pp. 806–807, 2002.
- [237] D. K. Gramotnev and S. I. Bozhevolnyi, "Plasmonics beyond the diffraction limit," *Nat. Photonics*, vol. 4, pp. 83–91, 2010.
- [238] S. Astilean, P. Lalanne, and M. Palamaru, "Light transmission through metallic channels much smaller than the wavelength," *Optics Communications*, vol. 175, pp. 265–273, 2000.
- [239] J. N. Anker, W. Paige Hall, O. Lyandres, N. C. Shah, J. Zhao, and R. P. V. Duyne, "Biosensing with plasmonic nanosensors," *Nature Materials*, vol. 7, pp. 442–453, 2008.
- [240] J. Li and M. Gu, "Gold-nanoparticle-enhanced cancer photothermal therapy," *IEEE Journal of Selected Topics in Quantum Electronics*, vol. PP, no. 99, pp. 1–8, 2009.
- [241] M. Born and E. Wolf, *Principles of optics : electromagnetic theory of propagation, interference and diffraction of light*. Pergamon Press New York, 1959.
- [242] D. Sarid and W. Challener, *Modern introduction to surface plasmons: theory, mathematical modeling, and applications*. Cambridge University Press, 2010.
- [243] S. H. Chang, S. Gray, and G. Schatz, "Surface plasmon generation and light transmission by isolated nanoholes and arrays of nanoholes in thin metal films," *Opt. Express*, vol. 13, no. 8, pp. 3150–3165, 2005.
- [244] R. wannemacher, "Plasmon supported transmission of light through nanometric holes in metallic thin films," *Optics communications*, vol. 195, pp. 107–118, 2001.

- [245] H. J. Lezec, A. Degiron, and E. Devaux, "Beaming light from a subwavelength aperture," *Science*, vol. 297, no. 5582, pp. 820–822, 2002.
- [246] Y. Xie, R. Armis, J. V. Moloney, and M. Mansuripur, "Transmission of light through slit apertures in metallic films," *Optics Express*, vol. 12, pp. 6106–6121, 2004.
- [247] M. J. Bastiaans, "The wigner distribution function applied to optical signals and systems," *Optics Communications*, vol. 25, no. 1, 1978.
- [248] E. Wigner, "The quantum correction for thermodynamic equilibrium," *Physical review*, vol. 40.
- [249] A. Walther, "Radiometry and coherence," *J. Opt.Sc. A*, vol. 58, no. 9, 1968.
- [250] A. Torre, *Linear Ray and Wave Optics in Phase Space*. Elsevier B.V., 2005.
- [251] M. E. Testorf, M. J. Hennelly, and B. Ojeda-castaneda, *Phase space optics:fundamentals and applications*. Mcgraw-hil, 2009.
- [252] C. J. Moreno and R. O. Martinez, "The Wigner function in paraxial optics II. Optical diffraction pattern representation," *Revista Mexicana De Fisica*, vol. 49, no. 3, pp. 290–295, 2003.
- [253] S. Cho, J. C. Petruccelli, and M. A. Alonso, "Wigner functions for paraxial and nonparaxial fields," *Journal of Modern Optics*, vol. 56, no. 17, pp. 1842–1852, 2009.
- [254] P. Lalanne, M. Besbes, and J. P. Hugonin, "Numerical analysis of a slit-groove diffraction problem," *J. Europ. Opt. Soc. Rap. Public.*, vol. 2, no. 07022, 2007.
- [255] P. Loughlin and L. Cohen, "A Wigner approximation method for wave propagation," *J. Acoust. Soc. Am.*, vol. 118, no. 3, pp. 1268–1271, 2005.
- [256] M. A. Alonso, "Diffraction of paraxial partially coherent fields by planar obstacles in the Wigner representation," *J. Opt. Soc. Am. A.*, vol. 26, no. 7, pp. 1588–1597, 2009.
- [257] M. J. Bastiaans, "Wigner distribution function and its application to first-order optics," *J. Opt. Soc. Am.*, vol. 69, no. 7, pp. 1710–1716, 1979.

- [258] M. A. Alonso, L. Edgar, and b. Vicenta, "Generalized radiometry as a tool for the propagation of partially coherent fields," *Optics Communications*, vol. 207, pp. 101–112, 2002.
- [259] M. A. Alonso, "Exact description of free electromagnetic wave fields in terms of rays," *Optics Express*, vol. 11, no. 23, pp. 3128–3135, 2003.
- [260] —, "Wigner functions for nonparaxial, arbitrarily polarized electromagnetic wave fields in free space," *J. Opt. Soc. Am. A.*, vol. 21, no. 11, pp. 2233–2243, 2004.
- [261] J. C. Petrucci and M. A. Alonso, "Phase space distributions tailored for dispersive media," *J. Opt. Soc. Am. A.*, vol. 27, no. 5, pp. 1194–1201, 2010.
- [262] M. W. Kowarz, "Homogeneous and evanescent contributions in scalar near-field diffraction," *Applied Optics*, vol. 34, no. 17, pp. 3055–3063, 1995.
- [263] J. W. Goodman, *Introduction to fourier optics*. Roberts and Company USA, 2005.
- [264] E. Wolf, *Introduction to the theory of coherence and polarization of light*. Cambridge University Press, 2007.
- [265] M. J. Bastiaans, "Application of the Wigner distribution function to partially coherent light," *J. Opt. Soc. Am. A.*, vol. 3, no. 8, pp. 1227–1238, 1986.
- [266] P. Lalanne, J. P. Hugonin, and J. C. Rodier, "Approximate model for surface-plasmon generation at slit apertures," *J. Opt. Soc. Am. A.*, vol. 23, no. 7, pp. 1608–1615, 2006.
- [267] T. D. Visser, "Plasmonics: Surface plasmons at work?" *Nat. Phys.*, vol. 2, pp. 509–510, 2006.
- [268] K. Leosson, T. Nikolajsen, A. Boltasseva, and S. I. Bozhevolnyi, "Long-range surface plasmon polariton nanowire waveguides for device applications," *Opt. Express*, vol. 14, no. 1, pp. 314–319, 2006.
- [269] M. S. A. and H. A. Atwater, "Plasmonics: Localization and guiding of electromagnetic energy in metal/dielectric structures," *J. Appl. Phys.*, vol. 98, p. 011101, 2005.

- [270] J. A. Dionne, L. A. Sweatlock, H. A. Atwater, and A. Polman, "Plasmon slot waveguides: Towards chip-scale propagation with subwavelength-scale localization," *Phys. Rev. B*, vol. 73, p. 035407, 2006.
- [271] E. D. Palik, *Handbook of Optical Constants of Solids*. Academic, 1985.
- [272] J. Y. Laluet, A. Drezet, C. Genet, and T. W. Ebbesen, "Generation of surface plasmons at single subwavelength slits: from slit to ridge plasmon," *New J. Phys.*, vol. 10, p. 105014, 2008.
- [273] H. A. Atwater, "The promise of plasmonics," *Sci. Am.*, vol. 62, no. 7, pp. 56–63, 2007.
- [274] X. Luo and T. Ishihara, "Subwavelength photolithography based on surface-plasmon polariton resonance," *Opt. Express*, vol. 12, no. 14, pp. 3055–3065, 2004.
- [275] M. G. Somekh, G. Stabler, S. Liu, J. Zhang, and C. W. See, "Wide-field high-resolution surface-plasmon interference microscopy," *Opt. Lett.*, vol. 34, no. 20, pp. 3110–3112, 2009.
- [276] R. Zia, J. A. Schuller, A. Chandran, and M. L. Brongersma, "Plasmonics: the next chip-scale technology," *Mater. Today*, vol. 9, pp. 20–27, 2006.